2010

Dual Phase Steel Characterization for Tube Bending and Hydroforming Applications

Chad Oliver
University of Windsor

Dual Phase Steel Characterization for Tube Bending and Hydroforming Applications

by

Chad Oliver

A Thesis

Submitted to the Faculty of Graduate Studies

through Materials Engineering

in Partial Fulfillment of the Requirements for

the Degree of Master of Applied Science at the

University of Windsor

Windsor, Ontario, Canada

2010

Dual Phase Steel Characterization for Tube Bending and Hydroforming Applications

by

Chad Oliver

APPROVED BY:

_____

Dr. S. Das, Outside Program Reader
Civil & Environmental Engineering

_____

Dr. D.O. Northwood, Program Reader
Mechanical, Automotive, & Materials Engineering

_____

Dr. D. Green, Co-Advisor
Mechanical, Automotive, & Materials Engineering

_____

Dr. R. Bowers, Co-Advisor
Mechanical, Automotive, & Materials Engineering

_____

Mr. B. Longhouse, Industrial Advisor
VARI-FORM

_____

Dr. H. Hu, Chair
Mechanical, Automotive, & Materials Engineering

September 7, 2010

Author's Declaration of Originality

I hereby certify that I am the sole author of this thesis and that no part of this thesis has been published or submitted for publication.

I certify that, to the best of my knowledge, my thesis does not infringe upon anyone's copyright nor violate any proprietary rights and that any ideas, techniques, quotations, or any other material from the work of other people included in my thesis, published or otherwise, are fully acknowledged in accordance with the standard referencing practices. Furthermore, to the extent that I have included copyrighted material that surpasses the bounds of fair dealing within the meaning of the Canada Copyright Act, I certify that I have obtained a written permission from the copyright owner(s) to include such material(s) in my thesis and have included copies of such copyright clearances to my appendix.

I declare that this is a true copy of my thesis, including any final revisions, as approved by my thesis committee and the Graduate Studies office, and that this thesis has not been submitted for a higher degree to any other University or Institution.

Abstract

This study examined the behaviour of dual phase steel tubes from three different strength grades undergoing rotary draw bending and pressure sequence hydroforming. It was found that the level of strain experienced by the tubes was independent of the steel grade. It was also shown that the same microstructural features that affect strength and elongation in uniaxial tensile testing affected dual phase steel tubes undergoing tube bending.

Seven commercial dual phase steels from three different suppliers were compared. It was found that the strength of the steels was mainly dependent on martensite volume fraction, while elongation was influenced by the level of martensite banding.

Nano indentation techniques were developed to facilitate the measurement of hardness of individual phases within dual phase steel. Three steels from different strength grades were tested. It was found that the hardness of the martensite phase followed the trend predicted by the calculated martensite carbon content.

Acknowledgements

First, I would like to thank my advisors Dr. Daniel Green and Dr. Randy Bowers for giving me the opportunity to work on this project. Their support and guidance has been much appreciated. I would also like to thank my committee members, Dr. Derek Northwood and Dr. Sreekanta Das for their insight and advice on my work.

A special thank you to Vari-Form and engineering manager Blair Longhouse for providing all of the necessary material, equipment and expertise that made this project possible.

I would like to extend thanks to John Robinson and Andy Jenner for their assistance with the preparation of all sample materials, Dr. Xueyuan Nie and Jun Feng Su for their generosity in allowing the use of their nano indentation equipment, and finally Abel Chang for his shared knowledge and support on all aspects of this project.

Table of Contents

List of Figures

List of Tables

Chapter 1:

Introduction

Dual phase steels were first investigated in 1963 by Williams and Davies [1], however they gained little attention until the oil crisis of the 1970's. It was during this time that automotive manufacturers focused their efforts on developing lighter vehicles in a bid to increase fuel economy. This interest faded in the following decades; however, more recently the trend towards light weight vehicles has re-emerged. In order to achieve weight savings, it is essential to reduce the overall mass of individual components within a vehicle. A large percentage of this weight is attributable to the body and structural components [2]. These components are typically constructed from flat sheet material; therefore by utilizing materials that possess higher strength, the thickness of these components can be reduced while still retaining their overall strength and integrity.

Dual phase steels have unique properties which make them ideally suited for use in automotive applications. Their excellent combination of strength and elongation, as seen in Figure 1.1, means that for a given strength level, they are able to be formed into more complex shapes than mild steel or high strength low alloy alternatives [3]. Dual phase steels exhibit low yield/tensile strength ratios combined with high rates of work hardening [4,5]. This allows them to be more easily formed while still providing final as-formed parts with significant strength. They also display continuous yielding behaviour, i.e. no indication of yield point elongation, giving them better forming characteristics [5,6].

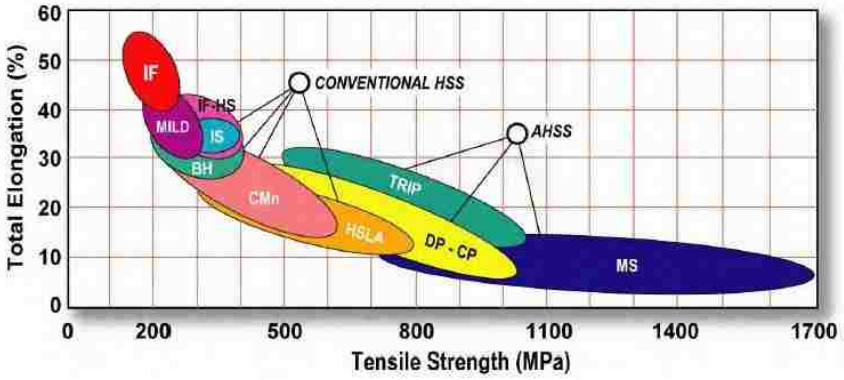

Figure 1.1: Comparison of total elongation and tensile strength for several types of steel [3]

Compared to other alternative non-ferrous materials such as aluminum and magnesium, dual phase steels offer several cost benefits for manufacturers. Their production is very similar to conventional steel, meaning that they require relatively low amounts of energy to produce [7]. They are also able to be recycled alongside other ferrous materials, giving them the ability to be handled by existing recycling facilities using standard sorting techniques. With regards to use on the production line, dual phase steels are able to be formed and joined using traditional methods [8]. This provides manufacturers significant cost savings as the costs of retooling factories are kept to a minimum. Due to these factors, it is expected that the use of dual phase steels in the automotive industry will continue to rise. It is therefore important that research and investigation of these steels continues, with efforts focusing on both improving the steels and refining the methods used to form them.

1.1 Objectives of Research

Vari-Form, a Tier 1 supplier of automotive structural components, currently utilizes several grades of dual phase steel in their production components. This steel is supplied by the producer to a tubing mill which roll forms, welds, and cuts it into straight tube lengths for utilization by Vari-Form's production line. Upon receipt of the tubing, it is subjected to a series of bending and hydroforming operations to produce completed components which are shipped to the automaker. As components become more complex in design, the demands placed on the strength and formability of dual phase steels is pushed to the limit. Previously, Vari-Form's

metallurgical knowledge of the steels they utilized was limited to what was provided to them by the steel maker. While they performed some mechanical testing of their own, their knowledge of what was happening to the material on a microstructural level during forming operations was lacking. Through partnership with the University of Windsor, their desire was to develop a greater understanding of material behaviour during their specific forming operations.

Vari-Form sources steel for their production from a number of suppliers. Traditionally, dual phase steel sourced from a steel producer is shipped with specifications of the material's minimum strength and elongation. There is no single standard to which all dual phase steels conform, and therefore each producer has their own specific "recipe" to produce a steel of a given strength grade. Steel of the same grade from different suppliers may vary in composition, microstructure, and behaviour at a microstructural level during forming. These differences can lead to variations in forming performance, and also cause certain steels to be less forgiving during the forming process. These differences become particularly important in a production scale environment, where an increase in scrap can cause time and financial losses. It is therefore desirable to take a detailed look at dual phase steels from several suppliers and compare them to determine whether differences exist, and how those differences might affect the steel performance based on what is known from literature.

The objectives of this research can be summarized as follows:

1. Observe and characterize both macro and microstructural performance of dual phase steel tubes undergoing Vari-Form's rotary draw mandrel bending and pressure sequence hydroforming processes.

2. Identify material differences that may affect deformation behaviour during tube bending, and make recommendations on what Vari-Form should look for when selecting a dual phase steel.

3. Characterize and compare several commercially available dual phase steels of similar grades from different suppliers with the intention of making recommendations as to which supplier's steel would be best for Vari-Form.

Chapter 2:

Literature Review

The following literature review is separated into three main sections. The first section addresses the important microstructural, physical and mechanical aspects of dual phase steels. A detailed overview of their production is provided, along with information related to their forming behaviour. The second section describes several manufacturing processes commonly used to fabricate tubular dual phase steel components. Finally, a brief summary of nano indentation hardness testing is presented.

2.1 Dual Phase Steels

Dual phase steels are low carbon steels that posses a microstructure consisting of a combination of ferrite and martensite. These phases are arranged such that the hard martensite is present in islands located at the grain boundaries within a soft ferrite matrix [1]. The islands can be separated, such as those seen in Figure 2.1, or connected to form a continuous martensite network.

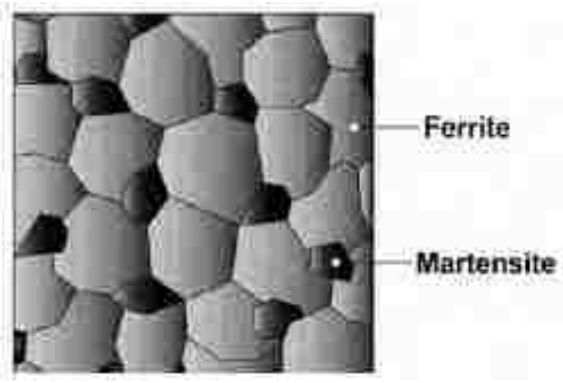

Figure 2.1: Diagram of dual phase steel microstructure [3]

The result of this composite microstructure is steel which possesses both high strength and good elongation. A comparison of tensile curves for three low carbon steels can be seen in

Figure 2.2. It is readily apparent that the dual phase steel possesses significantly higher strength than the conventional ferrite/pearlite low carbon steel, while still retaining good elongation. When compared to the high strength low alloy steel, the dual phase steel possesses better elongations at the same tensile strength, with continuous yielding behaviour.

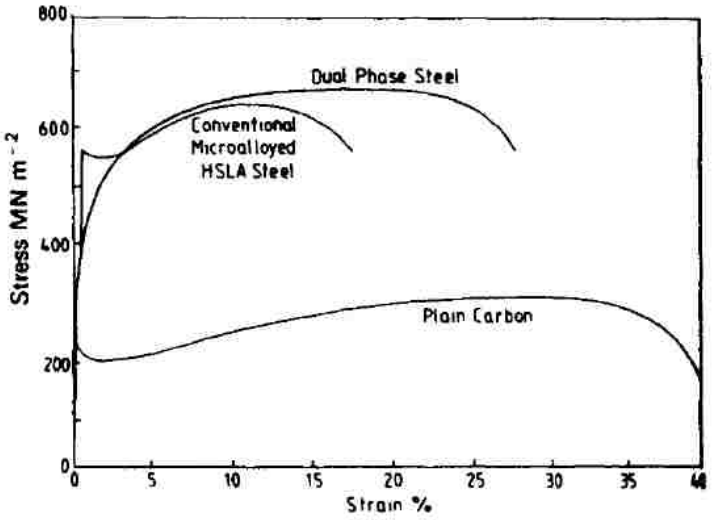

Figure 2.2: Comparison of tensile curves for different low carbon steels [9]

2.1.1 Production

Typical dual phase steels have carbon contents in the range of 0.05 to 0.2 weight percent. The region of the iron-carbon phase diagram which is of primary interest to dual phase steel production can be seen in Figure 2.3. The dual phase microstructure can be obtained from steel consisting of solely iron and carbon; however, it is more common for steels to contain additional alloying elements to assist in their production and improve their mechanical properties [10]. Such elements include manganese and silicon.

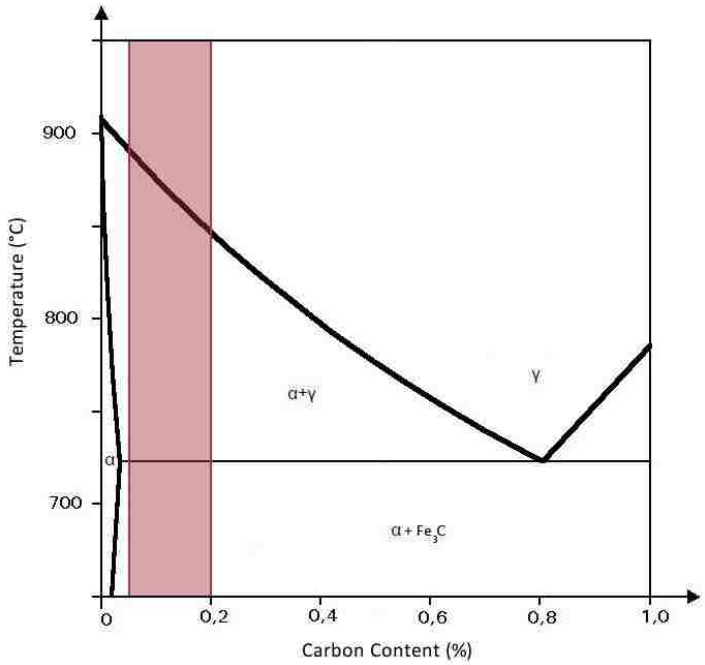

Figure 2.3: Iron-carbon phase diagram showing area of interest for typical dual phase steels

The dual phase steel microstructure can be created using two methods, namely sequential quenching and intercritical annealing [11]. The distinction between the two lies in the direction by which the α+γ phase field is reached. In sequential quenching, the α+γ field is reached by cooling the sample, while in intercritical annealing the α+γ field is reached by heating the sample. Graphical representations of the heat treatment paths for sequential quenching and intercritical annealing can be found in Figures 2.4 and 2.6, respectively.

In sequential quenching, the steel is first heated into the γ region to obtain a completely austenitic structure. This austenizing is often accompanied by hot rolling to reduce the thickness of the steel. After sufficient thickness reduction has been achieved, the steel is cooled to a temperature below the A_{r3}, but above the A_{r1} placing it in the α+γ region. It is then held for a period of time. Ferrite grains begin to nucleate at the prior austenite grain boundaries and start to grow into the austenite grains. It is important that the temperature of the steel at this stage be uniform across its width. It is possible for the centre of the strip to remain fully austenitic, while the edges enter the α+γ region [12]. This can produce a heterogeneous microstructure

that varies across the width of the steel sheet. After sufficient holding time the steel can be quenched to transform the austenite into martensite. The final dual phase microstructure produced from sequential quenching typically consists of large blocky shaped martensite islands surrounded by a coarse ferrite matrix [11]. This distinct martensite morphology can be observed in Figure 2.5. The substructure of the martensite can vary from lath to plate structures. It is dictated by the carbon content of the austenite present in the intercritical region; however, the percentage of carbon at which the transformation from lath to plate occurs can be influenced by the presence of other alloying elements [13].

Due to the limitations of the hot rolling process and the difficulty in obtaining consistent sheet thickness in the sub-millimetre range, hot rolled dual phase steels are typically used in applications requiring thicker material such as wheels, bumpers and suspension components.

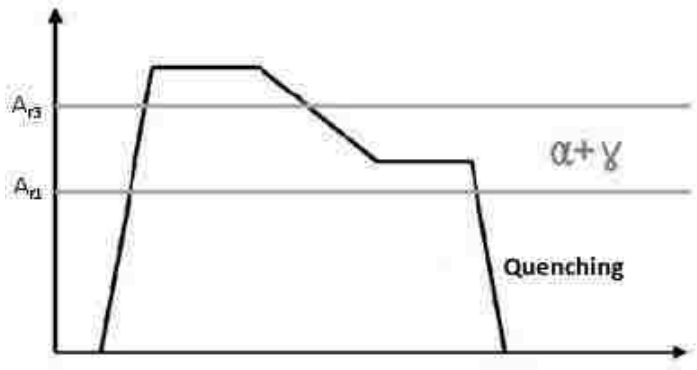

Figure 2.4: Heat treatment path for sequential quenching

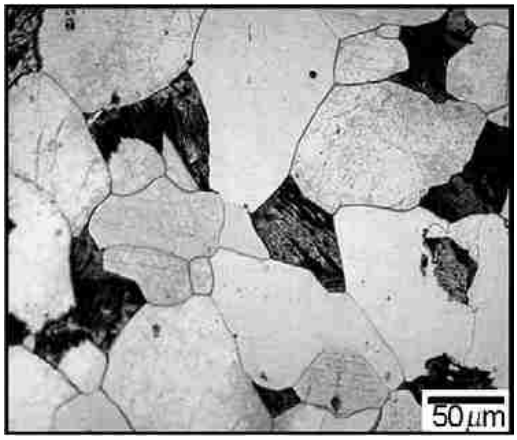

Figure 2.5: Microstructure of a sequentially quenched dual phase steel [11]

In order to obtain thin sheet commonly used in auto body components, dual phase steel is cold rolled followed by intercritical annealing heat treatment. In this method, the steel is supplied by the mill in the form of ferrite/pearlite sheet which can easily be cold rolled [14]. After rolling to the desired thickness, the steel is heated above the A_{c1} temperature, but below the A_{c3} temperature placing it in the α+γ phase region. Three main stages occur during intercritical annealing [15,16]. In the first stage, the dissolution of pearlite begins to occur at ferrite/carbide interfaces [11], forming austenite with eutectoid composition. This process is controlled primarily by carbon diffusion in austenite and occurs nearly instantaneously given that the diffusion distance is on the order of the pearlite interlamellar spacing. In the second stage, austenite begins to grow along grain boundaries and into the ferrite to achieve final equilibrium at the annealing temperature. This stage is controlled by both carbon and substitutional alloying element diffusion. In the last stage, there is final equilibration within the austenite. The concentration gradients of the substitutional elements are eliminated by their diffusion through the austenite grains. However, this is an extremely slow process given the slow diffusion rates of alloying elements in austenite, and does not fully progress during conventional intercritical annealing time scales [17].

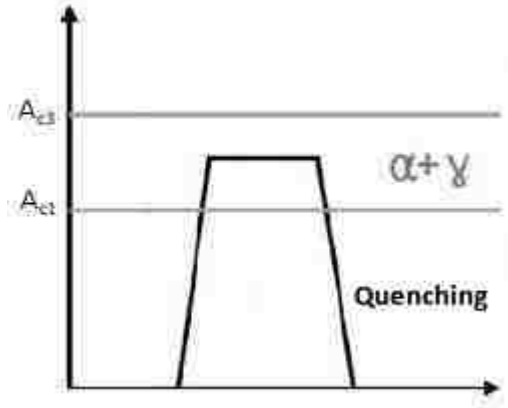

Figure 2.6: Heat treatment path for intercritical annealing

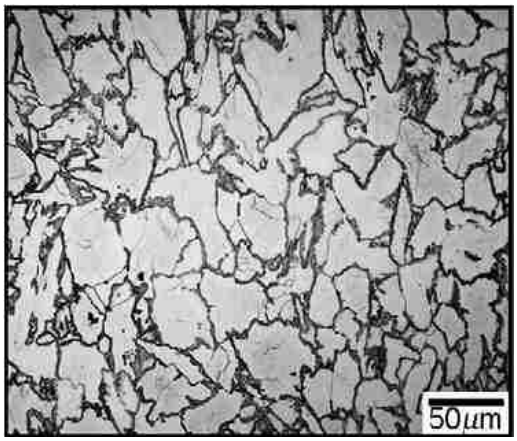

Figure 2.7: Microstructure of an intercritically annealed dual phase steel [11]

Austenite transformation following intercritical annealing is different from that after austenization in sequential quenching in two ways [17]. First, a nucleation step is not required to form new ferrite during cooling since the old ferrite present during annealing can grow epitaxially into the austenite. Secondly, under short intercritical annealing times, carbon but not substitutional alloying elements segregate and determine phase proportions and compositions.

In the intercritical annealing process, parameters such as temperature, holding time, and cooling rate control the volume fraction and composition of the constituents in the final microstructure. An example of a dual phase microstructure produced by intercritical annealing can be observed in Figure 2.7. Annealing temperature and soaking time in the intercritical region

controls the volume fraction of austenite, which is transformed to martensite upon quenching [18]. A higher intercritical annealing temperature will result in the formation of more austenite, while the carbon content of the austenite will be reduced. The fraction of austenite that transforms to martensite is a function of cooling rate and is affected by the carbon and alloying element content of the austenite and by the fineness of the dispersion of austenite particles [19]. A fine dual phase structure produces more martensite than a coarse microstructure after annealing at low temperatures and cooling at slow rates. This increased martensite fraction is a result of higher carbon enrichment in fine structures as compared to coarse ones [11]. The amount of interstitial carbon in ferrite of a dual phase steel depends on the intercritical annealing temperature and cooling rate. The solubility of carbon decreases with increasing intercritical annealing temperature [20]. At fast cooling rates, high levels of interstitial carbon may be trapped within the ferrite, reducing its ductility at room temperature [20].

2.1.2 Effects of Common Alloying Elements

The addition of alloying elements is very common in dual phase steels and is generally done to facilitate their production. The most common of these elements are manganese and silicon, due to their abundance and low cost.

When added to steel, manganese acts as an austenite stabilizer and can reduce the activity of carbon within the austenite phase [21]. These aspects retard the transformation kinetics allowing martensite to be formed at slower cooling rates. The diffusivity of manganese is substantially slower in austenite than in ferrite. With short holding times during intercritical annealing, the outer edges of austenite particles can become enriched in manganese. This increases local hardenability which, depending on cooling rate, may lead to the edges of the austenite particles transforming to martensite while the interior transforms to a ferrite/carbide aggregate [15]. The manganese enriched zone can be seen around the edges of the martensite particle in Figure 2.8.

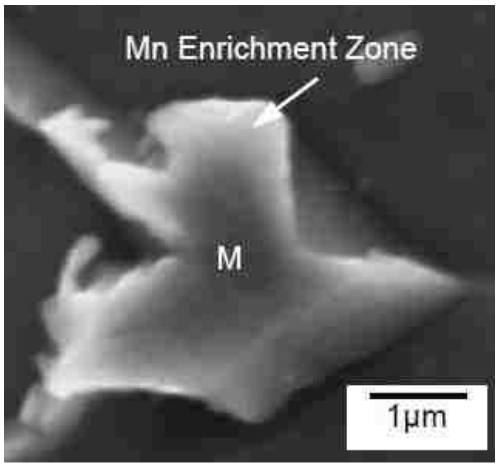

Figure 2.8: Manganese enriched zone within a martensite particle [15]

The composition of the austenite during intercritical annealing is also affected by the silicon content of the steel. The presence of silicon promotes carbon migration from the ferrite into the austenite, adding to the carbon content of the austenite [22]. Silicon also retards cementite formation during cooling which can suppress the formation of pearlite.

To allow for slower cooling rates after annealing while still giving the ability to form martensite, alloying elements such as molybdenum and chromium can be added to the steel [9]. While these elements reduce the critical cooling rate required to form martensite, they also increase the stability of the iron carbide in the initial sheet, requiring longer hold times in the intercritical region to dissolve it [18].

Dual phase steels can also benefit from precipitation hardening within the ferrite phase. Elements such as vanadium and titanium can be added to form fine dispersions of carbonitride precipitates. These precipitates provide a strengthening component within the ferrite and contribute to the hardenability of the steel. At typical intercritical annealing temperatures, the precipitates do not dissolve. As the steel is cooled, they inhibit the movement of the ferrite/austenite interfaces which results in a greater likelihood of martensite formation [9].

2.1.3 Banding

Microstructural banding in low alloy steel is caused by the segregation of substitutional alloying elements during dendritic solidification upon casting [23]. The addition of elements such as manganese, chromium, and molybdenum causes solidification to occur over a range of temperatures and compositions. This results in the dendrite cores solidifying as relatively pure metal, while alloying elements are rejected into the interdendritic spaces which become enriched in solute. These high and low solute regions are then elongated into parallel bands during rolling operations [24]. Differences in austenite transformation behaviours between the bands can lead to the formation of laminated microstructures upon subsequent heat treatment. This can be observed graphically from the CCT diagrams seen in Figure 2.9. Bands can transform into discrete layers of martensite, bainite, ferrite, and pearlite in the final cooled microstructure [25].

Manganese is the alloying element most responsible for the development of microstructural banding in low alloy steels [26]. During cooling, carbon migrates from low to high manganese regions. This redistribution of carbon is due to the effect of substitutional alloying elements on the temperature at which austenite begins to transform to ferrite (the A_{r1} temperature). During cooling, ferrite forms in bands with a high A_{r3} temperature and rejects carbon into the austenite of adjacent low A_{r3} temperature bands. This results in the formation of carbon rich and carbon depleted layers which directly impact the resulting microstructure during cooling.

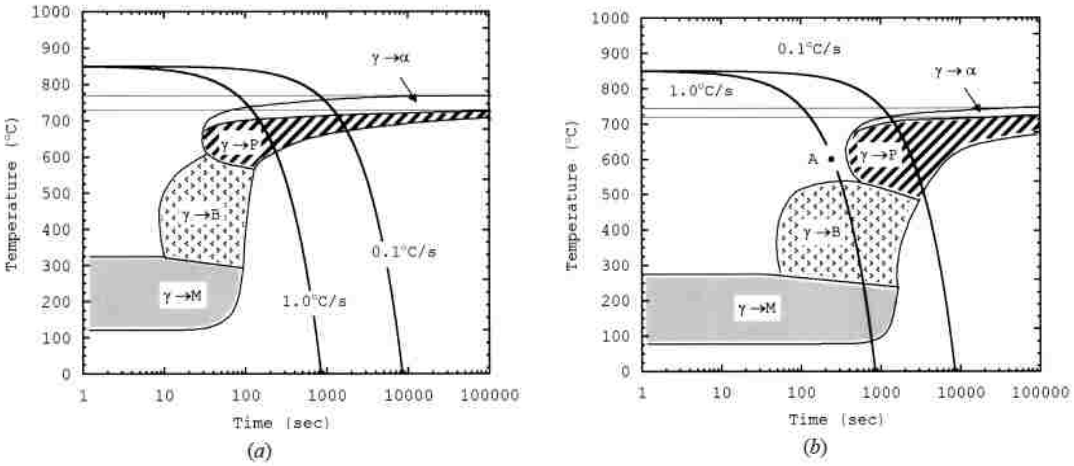

Figure 2.9: CCT diagrams for 5140 steel with (a) 0.82 wt% Mn and (b) 1.83 wt% Mn [26]

Regarding dual phase steels, hot rolled dual phase steels do not generally exhibit banding [27]**.** The presence of martensite banding in intercritically annealed dual phase steels is a direct result of inherited microstructure from the original ferrite/pearlite sheet. Although alloying element concentration gradients play a role, cooling rate, austenite grain size, and austenizing temperature also influence the severity of microstructural banding [26]. These parameters are controlled during the creation of the hot rolled ferrite/pearlite sheet, and thus cannot be altered during the intercritical annealing process. Permanent elimination of microstructural banding can only be achieved by high temperature homogenization treatments to remove the underlying compositional gradients. Such treatments are not practical on an intercritical annealing line, and therefore any elimination of banding in dual phase steels must come during the casting and hot rolling stages.

2.1.4 Structure-Property Relationships

The most important parameter dictating the mechanical properties of dual phase steels is martensite volume fraction [28]. Micrographs for three dual phase steels with varying martensite volume fractions can be seen in Figure 2.10. For a given martensite particle size, increasing the martensite volume fraction increases the tensile strength and work hardening rate, while decreasing the total elongation [9]. Yield strength is also affected by martensite

volume fraction; however, as the volume fraction is increased yield strength first decreases before starting to increase. This can be observed in Figure 2.11, and is thought to be associated with the gradual removal of yield point elongation at low martensite volume fractions [10].

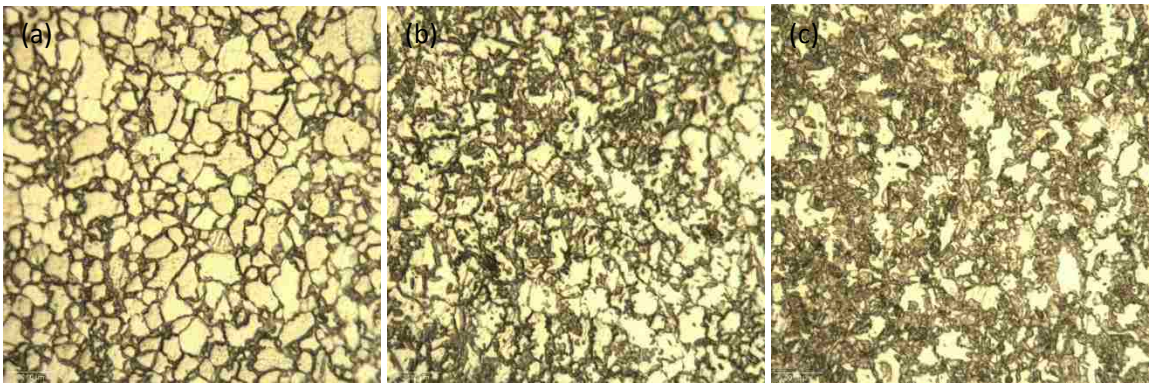

Figure 2.10: Steels with martensite volume fractions of (a) 14%, (b) 21%, and (c) 34%

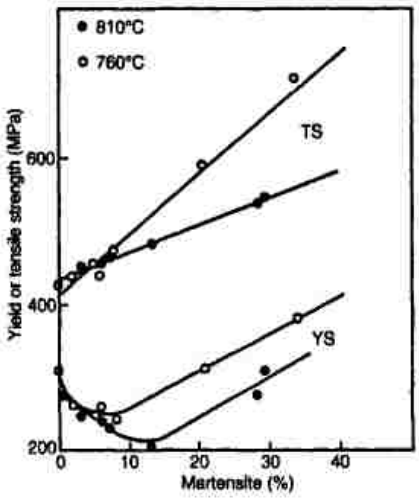

Figure 2.11: Strength vs. martensite volume fraction for two dual phase steels [28]

At a constant volume fraction of martensite, decreasing the mean particle size produces no effect on the tensile strength, but increases the work hardening rate and the maximum uniform elongation [29]. A reduction in ferrite grain size gives significant strengthening at small strains, but an increasing proportion of this strength arises from work hardening [9]. At low strains, the strain hardening rate increases with decreasing grain size, while at high strains the strain

hardening rate becomes nearly independent of grain size [30]. The optimum combination of strength and formability is obtained by a microstructure with a very fine distribution of martensite in a ferrite matrix with very small grain size [9].

The strengths of the individual phases within a dual phase steel play a role in the strength of the overall material. The strength of the ferrite phase is controlled mainly by steel chemistry and initial dislocation density upon cooling [31]. The addition of precipitate forming elements such as vanadium and titanium increase the strength of the ferrite [22]. The strength of martensite is determined by its structure (lath or plate) and by its carbon content [31]. The carbon content of martensite is determined by the intercritical annealing temperature. As the intercritical annealing temperature is decreased, the carbon content of the martensite increases [20]. Both the yield strength and tensile strength depend on martensite carbon content [32]. This can be seen in Figure 2.12. Increasing the martensite carbon content increases the yield and tensile strength of the steel [33]. A smaller volume of high carbon martensite produces the same strength steel as a larger volume of martensite of lower carbon content, however elongations may differ [22].

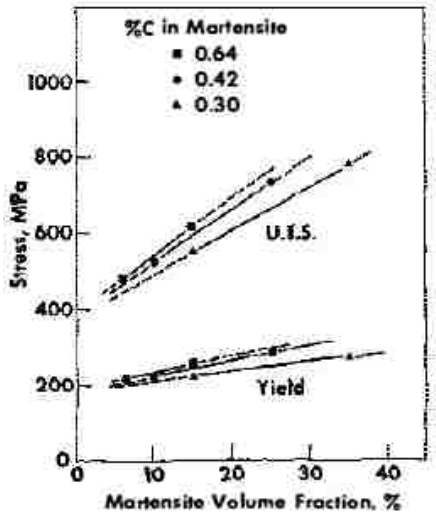

Figure 2.12: Comparison of strength for different martensite carbon contents [34]

2.1.5 Continuous Yielding Behaviour

The absence of yield point elongation in dual phase steel is attributable to the numerous free mobile dislocations, seen in Figure 2.13, introduced into the microstructure during the formation of martensite [5]. Upon quenching, there is a volume expansion of 2-3% which accompanies the martensitic transformation [35]. This introduces large numbers of dislocations in the vicinity of martensite particles. At low strains, these dislocations are able to move freely and yielding can start in several regions at the same time rather than in one localized region. This behaviour initiates a general yield process catastrophically. Additionally, localized regions are prevented from yielding due to the high back stresses the martensite islands exert on glide bands within the ferrite [9].

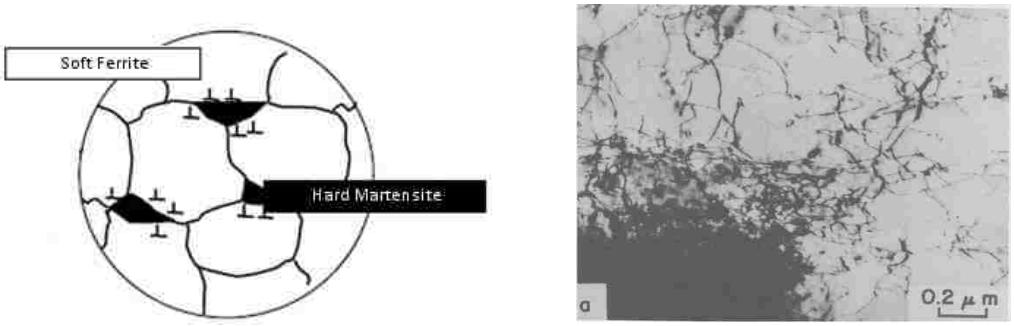

Figure 2.13: High dislocation density near martensite particles [35]

2.1.6 Work Hardening Behaviour

Unlike most conventional steels, the stress/strain behaviour of dual phase steel cannot be approximated by a simple parabolic function over the entire strain range [35]. In order to better understand the work hardening behaviour of the material, it is useful to perform a Jaoul-Crussard analysis [36]. This analysis consists of plotting the logarithm of the strain hardening rate as a function of the logarithm of true plastic strain. The resulting curve can then be analyzed for changes in slope to give indications of changes in work hardening behaviour. Jaoul-Crussard plots for several dual phase steels can be found in Figure 2.14. Based on this analysis, it is found that the work hardening of dual phase steels consists of three distinct phases [37,38]. Stage one results from the homogeneous deformation of the ferrite matrix produced by the

glide of mobile dislocations present near the martensite particles. Stage two, unique to dual phase steels, covers a period of diminished work hardening associated with constrained ferrite deformation in the presence of rigid martensite. In stage three, dislocation cell formation takes place after which further ferrite deformation takes place by cross slip and dynamic recovery processes. During this stage, it is also possible for the hard martensite phase to experience some degree of plasticity.

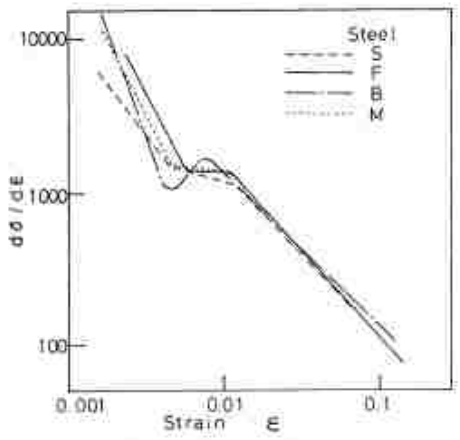

Figure 2.14: Jaoul-Crussard plot of several dual phase steels [14]

2.1.7 Deformation and Fracture

The composite deformation and fracture behaviour of dual phase steel can be ductile or brittle depending on the strength and level of damage development between the two phases [39]. At low martensite volume fractions, deformation and fracture is ductile and occurs by void nucleation, growth, and coalescence [40]. Void nucleation in dual phase steel has been associated primarily with martensite particles [40,41]. At low strains martensite particles begin to crack and separate, nucleating voids. This is followed by decohesion of ferrite/martensite interfaces as the strain is increased [40]. These mechanisms can be observed in Figure 2.15. The decohesion of the two phases is due to their widely different stress/strain characteristics, which results in their incompatibility [42]. The number of voids increases as the strain is increased and the size of these voids depends directly on the size of the martensite particles [43].

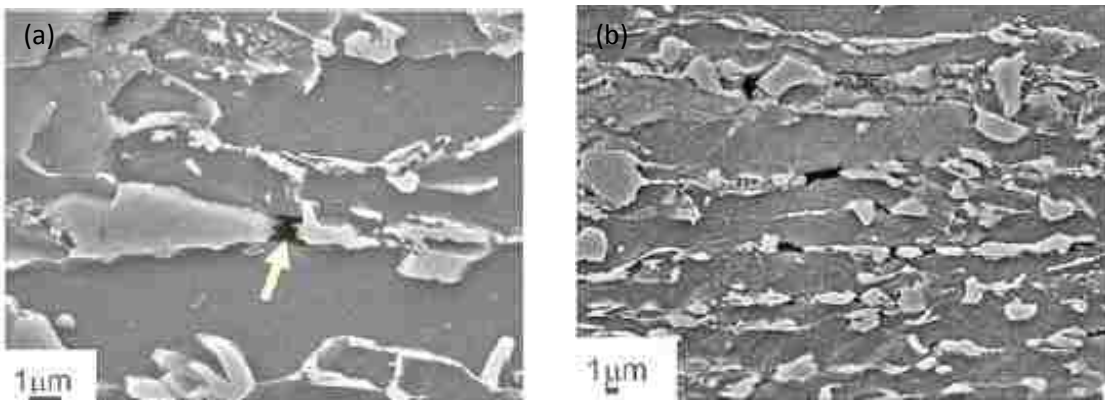

Figure 2.15: (a) Martensite separation and (b) ferrite/martensite decohesion [44]

When void growth is considered, the majority of voids formed at the ferrite/martensite interfaces grow along the ferrite boundaries parallel to the applied load. Voids formed under uniaxial stress tend to elongate in the tensile direction without coalescing, while voids formed under triaxial stress tend to grow in the transverse direction, eventually coalescing and causing failure [42].

At high martensite volume fractions, the fracture mode shifts toward brittle failure. The morphology of microvoids changes from decohesion at the ferrite/martensite interfaces to microcracks and fracture. Microcracks form at right angles to the tensile axis and experience minimal plastic deformation. There is no fixed martensite volume fraction at which brittle fracture occurs, and it is possible to see mixed mode fracture in steels with intermediate martensite volume fractions [45].

2.2 Manufacturing Processes

Thin-walled closed section tubular components are very desirable in automotive applications due to their strength and inherent stiffness [46]. In order to fabricate these components, it is common to start with tubes of a circular cross section. The following sections review the fundamentals of the manufacturing processes used to create dual phase steel tubes, and form them into finished components.

2.2.1 Roll Form Tube Making

To obtain a tubular structure, it is possible to subject flat steel sheet to a number of roll forming operations to form it into a round tube. In this continuous process, illustrated in Figure 2.16, the steel strip is guided through a series of roll forming stands, which deform the steel until it takes on the desired cross section. Once formed, the seam joining the two ends is welded either by high frequency resistance or laser welding techniques. The enclosed cross section then undergoes a sizing operation to obtain the required final dimensions, and is then cut into sections of a desired length.

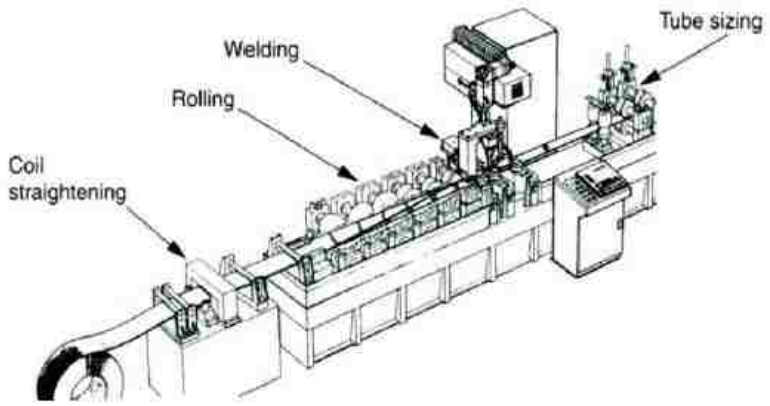

Figure 2.16: Layout of a tube rolling mill

The quality of incoming roll formed tubes is a major concern for bending and hydroforming operations [47,48]. Variations in tube material properties such as yield stress, flow stress, and hardness can lead to thinning or splitting during subsequent forming processes. It is known that the strain distribution around a roll formed tube is not uniform, and that for a given material and sheet thickness this non-uniformity is controlled by the roll forming sequence [49]. An illustration of this non-uniformity can be seen in Figure 2.17. This non-uniform strain causes non-uniform behaviours in strain hardening, flow stress, and elongation, which can significantly affect subsequent forming performance. It is of particular concern in dual phase steels where the high initial strain hardening rate exacerbates these non-uniformities [48]. Dual phase steel tubes produced for bending and hydroforming operations must be roll formed utilizing a sequence designed to minimize non-uniform strains around the tube circumference.

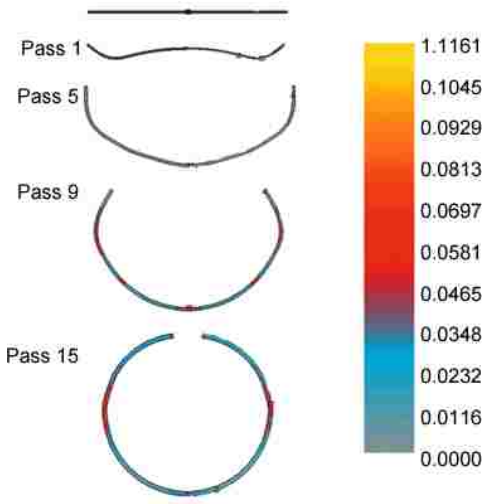

Figure 2.17: Effective strain of steel sheet after roll forming [49]

2.2.2 Rotary Draw Mandrel Tube Bending

The manufacture of complex tubular components produced using hydroforming often requires pre-forming operations before hydroforming can take place [50,51]. The most common of these pre-forming operations is tube bending, in which a straight length of tube is bent in one or more locations to get its rough shape close enough to the final shape so that it can be placed in the hydroforming die. Although several techniques can be used to bend tubing, the most popular and cost effective for bending thin walled tube is rotary draw mandrel bending. This process, seen in Figure 2.18, allows thin walled tube to be bent quickly and accurately without the undesirable side effects of tubing collapse or wrinkling [52].

Figure 2.18: Example of a steel tube which has undergone rotary draw mandrel bending

The rotary draw mandrel bending process utilizes a specialized bender which incorporates a series of dies and a mandrel [53]. A schematic of this equipment can be seen in Figure 2.19. A straight length of tube is placed over the mandrel and positioned against the clamp die. The clamp die is hydraulically forced against the tube to securely hold it in place. The bend die then begins to rotate, drawing the tube around it. While this is occurring, the pressure die opposes the outward force of the tube allowing it to be formed around the bend die. To prevent tubing collapse during forming, the mandrel remains inside the tube to give it support. As the tube is pulled around the bend die, it slides over the mandrel. This sliding motion can generate large frictional forces, and proper internal lubrication of the tube is required to avoid tube failure [54].

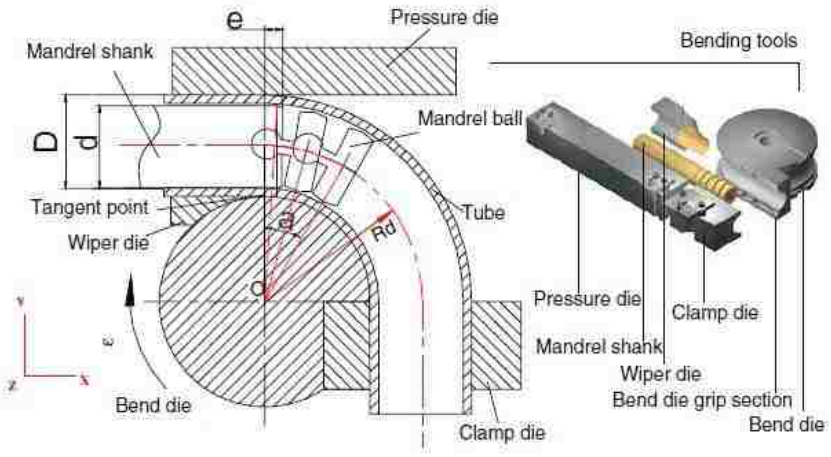

Figure 2.19: Schematic of a rotary draw mandrel bender [53]

In tube bending, the severity of the bend can be quantified using a number known as the bend ratio. The bend ratio, seen in Equation 2.1, is defined as the ratio between the centreline radius of the bend and the outside diameter of the tube being bent. It is considered the most important factor in determining the amount of deformation the tube will experience [55].

$$\text{Bend Ratio} = \frac{\text{Bend Centreline Radius}}{\text{Outside Tube Diameter}} \tag{2.1}$$

A decrease in bend ratio causes an increase in the tensile axial strain on the extrados of the bend and an increase in the compressive axial strain on the intrados of the bend [56]. As the bend ratio is decreased, the severity of the bend increases and the strains become greater. These strains result in a thinning of the tube on the extrados and a thickening of the tube on the intrados. If the thinning on the extrados becomes too great, the tube may fracture. To evaluate the strain in the tube extrados, a plane strain assumption may be used to give a rough approximation of the axial and thickness strains [52]. The axial strain can be calculated using Equation 2.2.

$$\varepsilon_{\text{axial}} = \ln\left(1 + \frac{\text{OD}}{2\text{R}_\text{o}}\right) \tag{2.2}$$

where OD is the outer tube diameter and R_o is the centreline radius of the bend. Once the axial strain is calculated, the thickness strain can be approximated by Equation 2.3.

$$\varepsilon_{\text{axial}} = -\varepsilon_{\text{thickness}} \tag{2.3}$$

Bending influences the properties of the tube and consequently its formability in subsequent hydroforming operations [51,57]. While strains experienced in hydroforming are mainly circumferential, tube bending strains are predominately axial. This sets up complex strain states within the tube, making predictions about the behaviour of the tube difficult [51]. Since plastic deformation in the cross section of the tube is not uniform after bending, the hydroformability is restricted by the thinned material around the extrados of the bend. This thinning can be

reduced by utilizing push assist during bending. If properly equipped, the bender can apply an axial force on the tube assisting its motion into the bend die. Tubes that are bent utilizing push assist will have more uniform wall thicknesses compared to tubes that are bent without it [57]. When utilizing materials such as high strength steels, which have limited formability, the use of push assist can be of great benefit to help reduce thickness variations in the final hydroformed part.

2.2.3 Pressure Sequence Hydroforming

Hydroforming is a specialized forming process in which a high pressure fluid is used to form material within a die at room temperature. Most commonly in the automotive industry, this process is used to form tubular components with complex cross sections [58,59]. An example of an upper fender rail produced for a sport utility vehicle can be seen in Figure 2.20. Traditionally, these components were fabricated using multi-piece stampings that were welded together to produce a closed section. The development of hydroforming allowed this welding step to be eliminated and provided the possibility of forming more complex shapes [59].

Figure 2.20: Example of an upper fender rail produced by hydroforming

In the conventional hydroforming process, seen in Figure 2.21, a high pressure fluid is pumped into a tube to raise its internal pressure. Once the hoop stress of the cross section exceeds the yield strength of the material, the forming begins and the tube expands to fill the surrounding

die [60]. Due to high internal pressures, when the tube begins to contact the walls of the die, significant frictional forces are generated. These forces oppose further sliding movement of the tube, and as a result, these areas stretch less while areas such as the corners which do not contact the die experience additional stretching [60]. It causes uneven wall thickness in the finished part and can lead to excessive material thinning in the corners, which may cause tube failure before the die is completely filled.

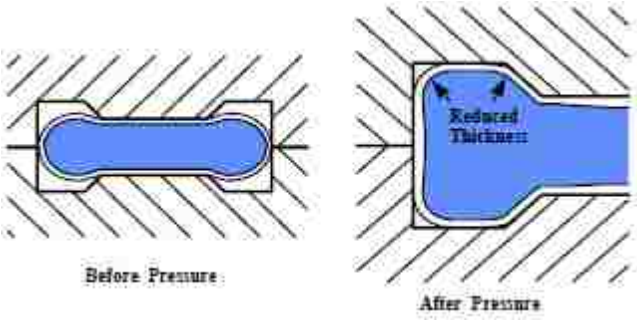

Figure 2.21: Illustration of the high pressure hydroforming process [61]

To avoid problems with excessive corner thinning, Vari-Form developed a patented hydroforming process referred to as pressure sequence hydroforming [62]. This process, seen in Figure 2.22, differs from traditional hydroforming in that it utilizes much lower fluid pressures. Instead of the tube expanding to fill a closed die, the die is initially open and is slowly closed around the tube with internal fluid pressures serving only to prevent collapse and pinching of the wall. Pressure sequence hydroforming forms the part by forcing the tube material to flow into the corners of the die without stretching or expansion [60,61]. The circumference of the initial tube is the same as the periphery of the die, meaning that the tube's cross section is only re-shaped, not expanded. The material's yield limit is exceeded in a bending mode to form the corner radii as opposed to a tensile mode in the conventional process. Additionally, since the tube forming is controlled by the closing die, the tendency for pinching at the die split line, common to high pressure hydroforming, is completely eliminated [61]. After completion of the die closing stage, internal pressures within the tube can be increased to flatten out the sides of the cross section and provide support for hole punching operations. Because the corners are formed by the closing of the press, the internal pressures required to completely form the cross

section are not governed by the pressures required to form the corners [60]. This allows complex cross sections to be formed with tight corner radii and without the risk of splitting the tube.

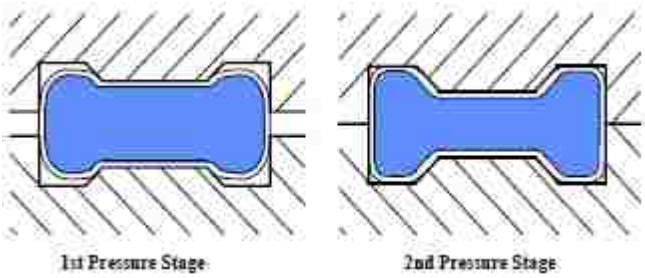

Figure 2.22: Illustration of the pressure sequence hydroforming process [61]

The pressure sequence hydroforming process is very useful in the forming of high strength materials such as dual phase steels, due mainly to the fact that average wall thickness after hydroforming is essentially equal to the wall thickness prior to hydroforming [61]. This can be observed in Figure 2.23, where the cross section of the pressure sequence hydroformed part exhibits significantly less thickness variation as compared to the cross section of the part formed by high pressure hydroforming. High strength steels, which posses lower elongations than conventional steels, can be successfully hydroformed without the concern of running out of elongation and failing in the corners of the die [61,63]. The limitations for the shapes of components able to be produced become contingent on material performance during pre-forming operations such as tube bending as opposed to hydroforming.

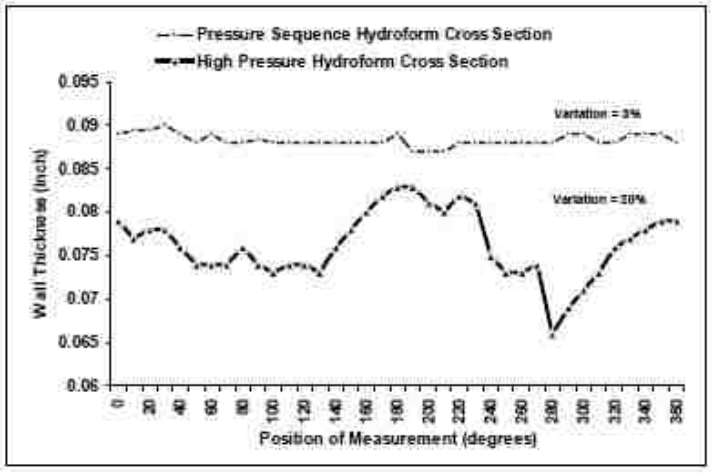

Figure 2.23: Comparison of tube wall thickness after hydroforming [60]

2.3 Nano Indentation Hardness Testing

The application of small scale indentation techniques to measure the hardness of materials is a long used and well established practice. In these techniques, a hard tipped indenter is forced, using a known load, into the surface of a sample material whose hardness is to be determined. Upon removal of the indenter, an impression is left behind. By measuring the dimensions of this residual indentation, the hardness of the material can be calculated according to Equation 2.4.

$$H = P_{max}/A_r \tag{2.4}$$

where P_{max} is the maximum indenter load and A_r is the surface area of the residual indentation. In order to measure the area of the indentation, these traditional techniques rely on the observation of the indentation dimensions using microscopy. This measurement presents a challenge as indentation size is reduced in order to probe smaller volumes. It becomes more difficult to adequately measure the dimensions on a small scale. The reduction of indentation size also presents a problem for the indenter tip. As indenting loads are reduced to limit the size of the indented area, indenters must be sufficiently sharp to leave an indentation which can be used to describe the hardness.

Nano indentation improves on these traditional methods by utilizing a nano scale indenter with a very precise tip shape. Due to the small indenter size, indentations in the sub-micron range are possible. The process by which nearly all nano indentation testing is done today was first described in 1992 by Oliver and Pharr [64]. The Oliver and Pharr method is carried out by utilizing indentation equipment, which can precisely measure both the load applied to the indenter, as well as the linear displacement of the indenter tip. It allows for the generation of a load-displacement plot, such as the one seen in Figure 2.24, from which values of several mechanical properties can be obtained.

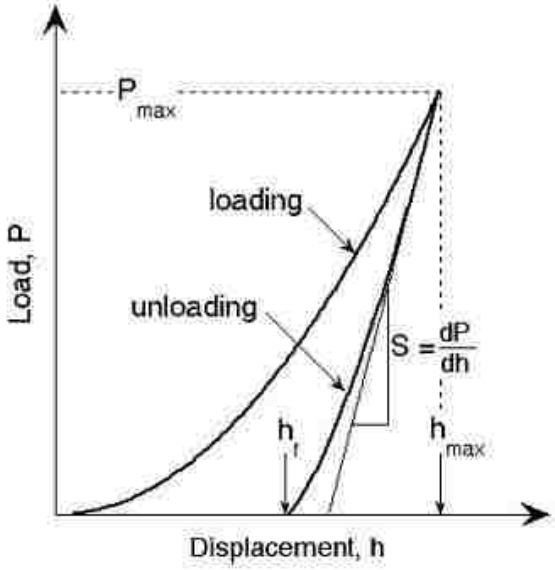

Figure 2.24: Example of a nano indentation load-displacement curve [65]

With one complete loading and unloading cycle performed, the hardness of the sample material can be calculated using Equation 2.5.

$$H = P_{max}/A(h_c) \tag{2.5}$$

where P_{max} is the maximum indenter load and $A(h_c)$ is the projected area of the indentation calculated as a function of the contact depth of the indenter. Given the inherent difficulty in measuring the dimensions of small indentations using microscopy, the Oliver and Pharr method

utilizes an area function which can be calculated in real-time based on the knowledge of the current indenter height. For the commonly used Berkovich indenter tip, seen in Figure 2.25, the area function can be described according to Equation 2.6.

$$A(h_c) = C_0 {h_c}^2 + C_1 h_c + C_2 {h_c}^{1/2} + C_3 {h_c}^{1/4} + C_4 {h_c}^{1/8} + C_5 {h_c}^{1/16} \quad (2.6)$$

where h_c is the indenter contact height, and C_0 through C_5 are calibration coefficients. For an ideal Berkovich indenter, C_0 will be equal 24.5 while the rest of the calibration coefficients will be equal to zero. To calibrate a real indenter, indentations are made on several materials with known elastic properties. An iterative procedure can then be used to identify and validate the correct tip shape function [64].

Figure 2.25: Ideal Berkovich indenter (a = 65.35°)

The slope of the load-displacement curve upon unloading is indicative of the stiffness of contact with the sample material. This stiffness can be related to the elastic modulus and the contact area using Equation 2.7.

$$S = \beta \frac{2}{\sqrt{\pi}} E_r \sqrt{A(h_c)} \quad (2.7)$$

where β is a constant related to the indenter shape, $A(h_c)$ is the indenter area function, and E_r is the reduced elastic modulus of the material being indented. The reduced elastic modulus

obtained from this relationship includes a stiffness contribution from both the sample material and the indenter. In order to separate the effect of each, Equation 2.8 can be used.

$$\frac{1}{E_r} = \frac{(1-\nu_i^2)}{E_i} + \frac{(1-\nu_s^2)}{E_s} \tag{2.8}$$

where ν_i and E_i are the Poisson ratio and elastic modulus of the indenter, and ν_s and E_s are the Poisson ratio and elastic modulus of the sample material.

2.3.1 Associated Challenges

Given the small scale of nano indentation testing, several issues arise that introduce errors and potentially provide invalid results. The most prominent source of error is the effect of surface roughness of the sample being tested. Due to the small size of the indenter tip, testing on a sample which is not sufficiently smooth can mean that the deformation induced by the indenter is not uniform. An example of this can be seen in Figure 2.26. On a high roughness surface, it is possible that the indenter will encounter peaks on the sample surface. This can cause the measured load to be unrepresentative of the true load required to force the indenter into the surface at the given depth.

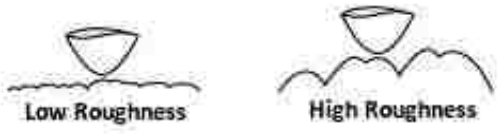

Figure 2.26: Effect of surface roughness on indenter tip

The indentation size effect must also be noted when performing nano indentation tests. It is often observed that the hardness of a material increases as the indentation size is decreased. This phenomenon must be taken into account when comparing indentation results obtained using different loads. For the best possible results, it is wise to only compare indentations that have been performed using similar loading levels.

When performing multiple indentations inside a defined area, it is possible for indenter drift to occur. This phenomenon involves the unintended and undesired movement of the indenter tip. Nano indentation equipment is very large in comparison with the size of the displacements it is designed to measure. It is possible for the thermal expansion of the equipment to have a significant influence on the position and stability of the indenter. Differences in rates of heat generation by the equipment can cause persistent deviations to the indenter position. This problem has been addressed on many new devices by the inclusion of automatic routines, which make corrective movements to the indenter tip to counter the undesired movements. Although this method provides a remedy to the problem, drift may still be encountered when large numbers of indentations are placed within a small area. While it is possible for the effects of the issues discussed above to be minimized, it is important for the operator of the nano indentation equipment to be aware of them, and to be able to properly interpret the results obtained from experiments.

Chapter 3:

Experimental Details

Commercial dual phase steels were obtained from three suppliers. Mechanical testing and metallography was performed on each steel to ascertain its mechanical and microstructural properties. The following chapter describes in detail, the steps performed to test and characterize each material.

3.1 Materials

Dual phase steels falling under three different strength grades were acquired from three separate suppliers. All steels were obtained in the form of cold rolled flat sheet. In order to assure both confidentiality and consistency throughout experimentation, identification numbers were assigned to each steel. These steels and corresponding identification numbers have been summarized in Table 3.1.

	DP600			DP780		DP980	
ID#	1	2	3	4	5	6	7
Supplier	A	B	C	A	B	A	B
Thickness (mm)	1.2	1.25	1.0	1.2	1.5	1.2	1.2

Table 3.1: Dual phase steel material summary

3.2 Tensile Testing

Tensile specimens were cut from as-rolled sheet using a wire EDM to minimize distortion. Dimensions were chosen according to the ASTM E8 standard sheet type specimen size. Thickness “T”, as seen in Figure 3.1, varied depending on the steel tested. For each material, specimens were obtained from longitudinal, transverse and 45° diagonal orientations.

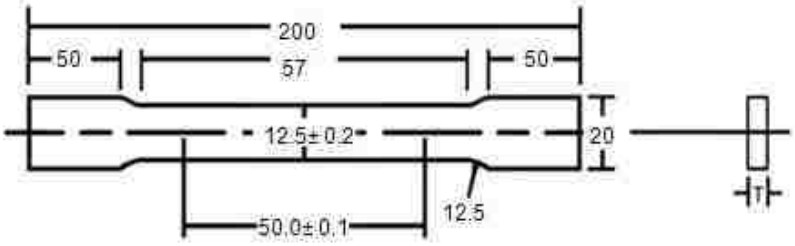

Figure 3.1: ASTM E8 standard sheet type specimen (dimensions in mm)

Testing was carried out using an ADMET 2613 universal testing machine, seen in Figure 3.2, equipped with a 50 kN load cell. Strain readings were taken using two Epsilon Technologies extensometers, measuring axial and width strains with a typical linearity of 0.2%. All samples were tested at room temperature utilizing a crosshead speed of 0.1 mm/sec. Data was collected and analyzed using ADMET's MTEST software.

Figure 3.2: Tensile testing setup

3.2.1 Strain Hardening Exponent

Calculation of the strain hardening exponent, or n-value, was performed as specified in ASTM E646. The engineering stress/strain values obtained from the tensile tests were converted to true stress/strain values according to Equations 3.1 and 3.2.

$$\sigma = S(1 + e) \tag{3.1}$$

$$\varepsilon = \ln(1 + e) \tag{3.2}$$

where σ and ε are the true stress and true strain values, and S and e are the engineering stress and engineering strain values. The n-value was determined for strains between 5 and 10 percent, or up to the uniform elongation when it was found to fall inside this range. By taking a line of best fit of N true stress/strain data pairs, the n-value was calculated according to Equation 3.3.

$$n = \frac{N\sum_{i=1}^{N}(\log\varepsilon_i \log\sigma_i) - (\sum_{i=1}^{N}\log\varepsilon_i \sum_{i=1}^{N}\log\sigma_i)}{N(\log\varepsilon_i)^2 - (\sum_{i=1}^{N}\log\varepsilon_i)^2} \tag{3.3}$$

3.2.2 Plastic Strain Ratio

The plastic strain ratio, or r-value, is a parameter that indicates the ability of a sheet metal to resist thinning or thickening under tensile and compressive forces in the plane of the sheet. It is defined for a uniaxial tension test in Equation 3.4.

$$r = {\varepsilon_w}/{\varepsilon_t} = \frac{\ln(w_f/w_o)}{\ln(t_f/t_o)} \tag{3.4}$$

where ε_w is the width strain, ε_t is the thickness strain, w_f is the final specimen width, w_o is the initial specimen width, t_f is the final specimen thickness and t_o is the initial specimen thickness.

Due to the difficulties in precisely measuring thickness strains during tensile testing, it is possible to replace ε_t according to Equation 3.5, using a constant volume assumption.

$$\varepsilon_t = \ln(l_o w_o / l_f w_f) \tag{3.5}$$

This equation allows the r-value to be easily calculated utilizing the length and width extensometer data based on Equation 3.6.

$$r = \frac{\ln (w_o/w_f)}{\ln (l_f w_f / l_o l w_o)} \tag{3.6}$$

where l_o is the initial specimen gauge length and l_f is the final length of the gauge. The average r-value for each test was determined between 5 and 10 percent strain. According to ASTM E517, a final mean r-value was calculated by averaging the r-values obtained for tensile specimens taken in the 0°, 45° and 90° orientations according to Equation 3.7.

$$r_m = (r_{0^\circ} + 2r_{45^\circ} + r_{90^\circ})/4 \tag{3.7}$$

3.3 Tube Bending and Hydroforming

Tube bending and hydroforming was performed on steels 1, 4, and 7. In order to create tubes from the dual phase steel, coils were sent to a tubing mill which roll formed and welded the material to create tubes with an outside diameter of 63.5 mm. The DP600 and DP780 tubes were welded using conventional high frequency electric resistance welding; however, the strength of the DP980 required the use of more precise laser welding.

3.3.1 Tube Preparation

Tubing received from the mill was cut to appropriate lengths and then etched using the electro-etching apparatus seen in Figure 3.3. Grids consisting of 2.54 mm circles were imprinted around the circumference of the sample tubes in several locations corresponding to the regions where subsequent bending was to take place.

Figure 3.3: Electro-etching apparatus

3.3.2 Tube Bending

Tube bending was carried out using an Eagle Precision Technologies electro-hydraulically driven rotary draw mandrel bender. The bender, seen in Figure 3.4, was fully CNC enabled allowing bending parameters to be easily adjusted. Standard production quality tooling was utilized, including bend, clamp, pressure, and wiper dies. To ensure tube integrity and to prevent tubing collapse, a flexible five-ball mandrel was used.

For each steel grade, bending was attempted using bend ratios of 3.1, 2.0, and 1.73 (see Equation 2.1). In order to achieve the desired bend, the bend angle was increased to account for material springback. Due to the high strength of the material, a boost pressure of 12.4 MPa was used while 9.0 MPa was applied to the pressure die.

Figure 3.4: Eagle Precision Technologies rotary draw mandrel bender

3.3.3 Hydroforming

Hydroforming was carried out on Vari-Form's manufacturing line utilizing tooling used to produce upper fender rails for a production vehicle. Their pressure sequence hydroforming process was used with low fluid pressures of 7 MPa and high fluid pressures of 55 MPa. Due to the constraints imposed by the production tooling, only tubes which had been bent with a bend ratio of 3.1 were able to be hydroformed.

3.3.4 Strain Measurements

After bending and hydroforming, strain measurements were obtained using the etched circle grids which had been deformed into ellipses. The bent sections of tube were cut into wedges, similar to that seen Figure 3.5, for observation.

Figure 3.5: Circle gridded section on a bent tube

Observation was carried out using a Leica MZ8 stereomicroscope, seen in Figure 3.6. The tube sections were placed on the microscope and dimensions were recorded for the deformed circles on the extrados of the tube bend and around the tube circumference at the midpoint of the bend. Thickness measurements were performed using both a ball end micrometer and a GE CL5 ultrasonic tester.

Figure 3.6: Circle grid strain measurement equipment

After measurement, true principal strains were calculated for each deformed circle according to Equations 3.8 through 3.10.

$$\varepsilon_1 = \ln\frac{l_1}{l_0} \tag{3.8}$$

$$\varepsilon_2 = \ln\frac{l_2}{l_0} \tag{3.9}$$

$$\varepsilon_3 = \ln\frac{t}{t_0} \tag{3.10}$$

where:

l_1 – ellipse major diameter;

l_2 – ellipse minor diameter;

l_0 – initial circle diameter;

t_0 – initial tube wall thickness;

t – final tube wall thickness.

3.4 Micro Hardness

Micro hardness measurements were performed in accordance with ASTM E384. Measurements were taken from the normal orientation on flat sheet samples. Testing was done using a Buehler Micromet II equipped with a Vickers indenter set at 300 g. Indentation dimensions were obtained using the machine's built in measuring system, and converted to Vickers hardness values according to Equation 3.11.

$$\mathrm{HV} = \frac{0.1891\mathrm{F}}{\mathrm{d_{avg}}^2} \tag{3.11}$$

where F is the indenter force in newtons and d_{avg} is the average of the two pyramidal lengths in millimetres.

3.5 Nano Hardness

Nano indentation testing was performed on steels 1, 4, and 6 in order to obtain hardness values for the ferrite and martensite phases within each material. Testing was carried out following the guidelines specified in ASTM E2546. Samples were prepared from flat sheet, and both etched and unetched samples were tested. Indentation was performed using a Hysitron TI 700 Ubi scanning nano indenter, seen in Figure 3.7, equipped with in-situ SPM capabilities. Indentation data was collected and processed using Hysitron's Triboscan software.

Figure 3.7: Hysitron TI 700 Ubi nano indenter

A Berkovich tip indenter was used to produce indentations in rectangular grid patterns of varying dimensions. A maximum load of 250 μN was applied using a trapezoidal loading function, illustrated in Figure 3.8, to reduce time dependent effects. Values for hardness and elastic modulus were determined using the methods of Oliver and Pharr as described in Section 2.3.

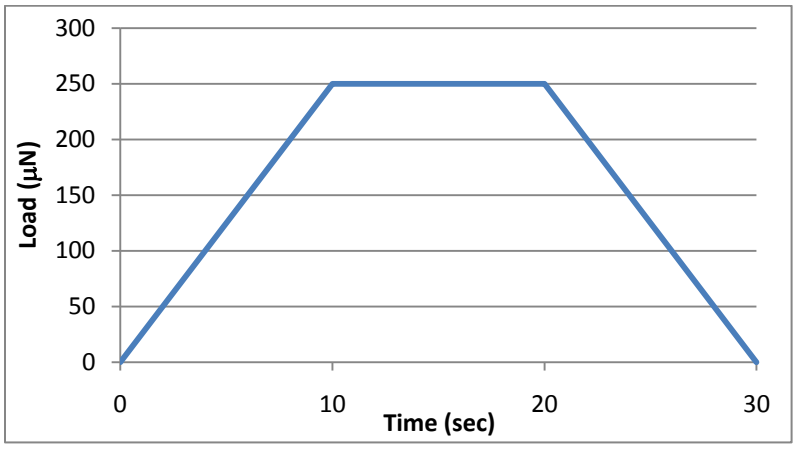

Figure 3.8: Trapezoidal loading function

3.6 Microstructural Analysis

Microstructural analysis was performed on as-received flat sheet, tensile samples, and bent tubing. Samples were prepared using polishing and etching, and then observed with optical and electron microscopes. Micrographs were taken, and used to determine a variety of microstructural properties.

3.6.1 Sample Preparation

Metallographic specimens from the as-rolled flat sheet were cut into samples approximately 1 cm^2 in size. These samples were mounted in 38.1 mm molds using diallyl phthalate thermosetting resin, which was cured at 150 °C and 3000 psi for 90 seconds. For each specimen, three samples were mounted, exposing the normal, rolling, and transverse planes. After mounting, samples were subjected to grinding and polishing according to the following sequence:

1. Four stage progressive manual grinding using SiC paper (240, 320, 400, 600 grit).
2. Intermediate polishing using 9 μm diamond paste on a nylon cloth wheel.
3. Two stage final polishing using alumina powder on micro cloth wheels (1 μm, 0.05 μm).

Upon completion of each polishing step, samples were cleaned with soap and water, and then rinsed with ethanol. To develop the ferrite grain boundaries and to reveal the ferrite/martensite interfaces, a 2% Nital etchant was prepared and placed in a shallow dish [66]. Samples were then immersed in the etchant for approximately 10-20 seconds to expose the microstructure.

Fracture surfaces were observed for both tensile and bent tube samples. For tensile samples, one side was collected from each specimen and carefully cut to remove the necked region and fracture surface. For bent tube samples, after failure during bending, a band saw was used to remove the section of interest. For both sample types, cleaning was carried out using an ultrasonic cleaner before observation.

For each tensile fracture surface that was observed, a corresponding sample was taken from the opposite side of the failed specimen in order to observe void sizes and distributions. Samples were cut according to Figure 3.9 using a wire EDM in order to preserve the void patterns. The wire EDM was offset from the centreline of the sample by half its kerf width, ensuring that the plane to be observed was in the exact middle of the tensile sample.

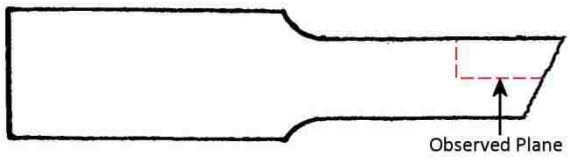

Figure 3.9: Fracture cross section

Preparation of the fracture cross section samples was carried out using the same three step grinding and polishing sequence performed on the flat sheet samples. After polishing, initial etching was carried out using 2% Nital to remove any flowed metal on the sample surface. A final re-polishing was completed using 0.05 μm alumina.

3.6.2 Microscopy

Optical microscopy was carried out using a Leitz Laborlux 12ME equipped with a Paxit PAXcam imaging system. Images were taken of all flat mounted samples.

A JEOL JSM-5800LV scanning electron microscope equipped with an EDAX energy dispersive spectrometer was used to image both flat mounted samples and fracture surfaces. Images were taken with an accelerating voltage of 15 kV using secondary electrons. Fracture surfaces and samples with large exposed surface areas were imaged without modification. Through-thickness samples were sputter-coated with gold in order to avoid problems with sample charging.

3.6.3 Grain Size

Ferrite grain size was determined according to the ASTM E112 grain counting method. A combination of optical and SEM micrographs were used in conjunction with Media Cybernetic's Image-Pro Plus analysis software to obtain a mean grain size for each material.

3.6.4 Martensite Volume Fraction

Martensite volume fraction was determined using Image-Pro Plus software according to ASTM E1245. Both optical and SEM micrographs were utilized for each material in order to obtain the best possible representative value. In order to confirm the results from the image analysis software, several micrographs from each material were treated to the traditional point counting method as described in ASTM E562.

3.6.5 Martensite Banding

To describe and characterize the extent of martensite banding in the sample steels, the ASTM E1268 linear intercept method was used. The anisotropy index was calculated for each sample material according to Equations 3.12 through 3.14.

$$AI = N_{L\perp}/N_{L\parallel} \quad (3.12)$$

$$N_{L\perp} = N_{\perp}/L_t \quad (3.13)$$

$$N_{L\parallel} = N_{\parallel}/L_t \quad (3.14)$$

where:

AI – anisotropy index (for a non-banded microstructure AI = 1);

$N_{\perp}$ – number of feature interceptions with test lines perpendicular to the rolling direction;

$N_{\parallel}$ – number of feature interceptions with test lines parallel to the rolling direction;

L_t – test line length (mm).

3.7 Chemical Composition

The chemical compositions of each sample material were determined using a Thermo Scientific ARL 3460 optical emission spectrometer according to ASTM E415. These results were found to match the heat chemistries supplied by the steel producers very closely.

Chapter 4:

Experimental Results

The following chapter presents a summary of the results obtained from tensile testing, tube forming, and microstructural analysis. Numerical data has been compiled into tables, while tensile curves, tube strains, micrographs, and nano indentation results have been shown using representations indicative of what was observed for each material.

4.1 Tensile Testing

Tensile testing was carried out on each steel using three samples from each orientation. Figure 4.1 shows representative engineering stress-strain curves for each steel taken from samples oriented parallel to the rolling direction.

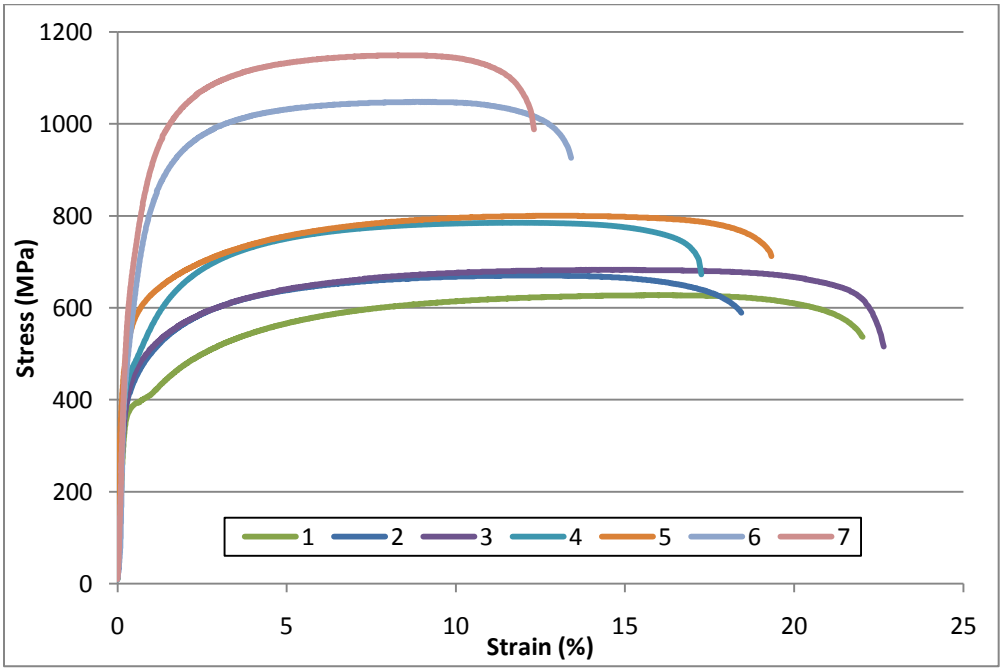

Figure 4.1: Representative tensile curves for tested steels

Table 4.1 summarizes the average values of the mechanical properties for each steel. Values obtained from replicate tests were found to vary by no more than five percent. Due to the continuous yielding behaviour of the steels, yield strength was determined by the 0.2 percent offset stress. The entry entitled yield discontinuity refers to the observation of discontinuous yielding seen in the DP600 and DP780 grades from supplier A. The values represent the range of strain over which discontinuous yielding was found to occur. Discontinuous yielding is not commonly seen in dual phase steels, as one of their key features is the lack of yield point elongation. Further discussion on this issue and an overview of some potential causes is found in Section 5.2.2.

	DP600			**DP780**		**DP980**	
ID#	1	2	3	4	5	6	7
Yield Strength (MPa)	383.6	434	424.4	474	552	621.7	748
Tensile Strength (MPa)	638.9	682	692.1	789	804	1085.7	1153
YS/TS	0.60	0.64	0.61	0.60	0.69	0.57	0.65
Yield Discontinuity (%)	0.5	0	0	0.25	0	0	0
Uniform Elongation (%)	16.2	13.8	13.4	11.5	14.4	9	9.1
Total Elongation (%)	21.4	18.7	22.8	17.2	19.7	13.4	12.4
n-value	0.16	0.13	0.2	0.13	0.15	0.1	0.08
r-value	1.11	0.96	0.91	0.93	0.87	0.78	0.73

Table 4.1: Summary of mechanical properties for tested steels

4.2 Tube Bending

Tube bending was carried out on steels 1, 4, and 7; representing one steel from each strength grade. As the bend ratio was decreased, material failures began to occur. These results have been summarized in Table 4.2. The DP980 steel was not tested using a bend ratio of 1.73 given its poor performance with a bend ratio of 2.0.

ID#	Steel Grade	Bend Ratio - 3.1		Bend Ratio - 2.0		Bend Ratio - 1.73	
		# of Tubes	Result	# of Tubes	Result	# of Tubes	Result
1	DP600	12	Success	8	Success	8	1 Failed
4	DP780	12	Success	8	5 Failed	6	5 Failed
7	DP980	8	Success	6	5 Failed	-	-

Table 4.2: Summary of tube bending results

4.2.1 Strain Distributions

Strains were obtained by measuring the dimensions of the deformed circles that were etched onto the surface of each tube. To ensure a proper comparison amongst all tubes, each measured circle was identified using a series of angles based on its location on the bent tube. The locations to which these angles correspond can be found in Figure 4.2. For strains measured around the tube circumference, 0° corresponds to the weld seam with angle increasing towards 90° at outside of the bend. For strains measured around the extrados of the bend, 0° corresponds to the location of the clamp die with angle increasing towards the mandrel side of the tube.

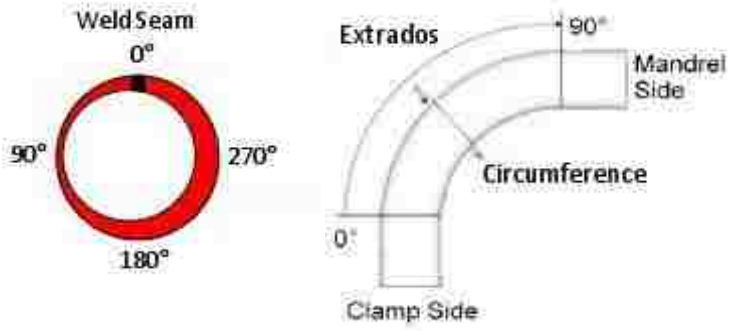

Figure 4.2: Orientations and angles used for strain measurements

Figures 4.3 through 4.8 summarize and compare the bending strains as follows: each steel grade for a given bend ratio; each bend ratio for a given steel grade; and bending versus hydroforming for a given steel grade. Hoop strains were found to be significantly less than axial and thickness strains, and therefore have been omitted from the graphs for the sake of clarity.

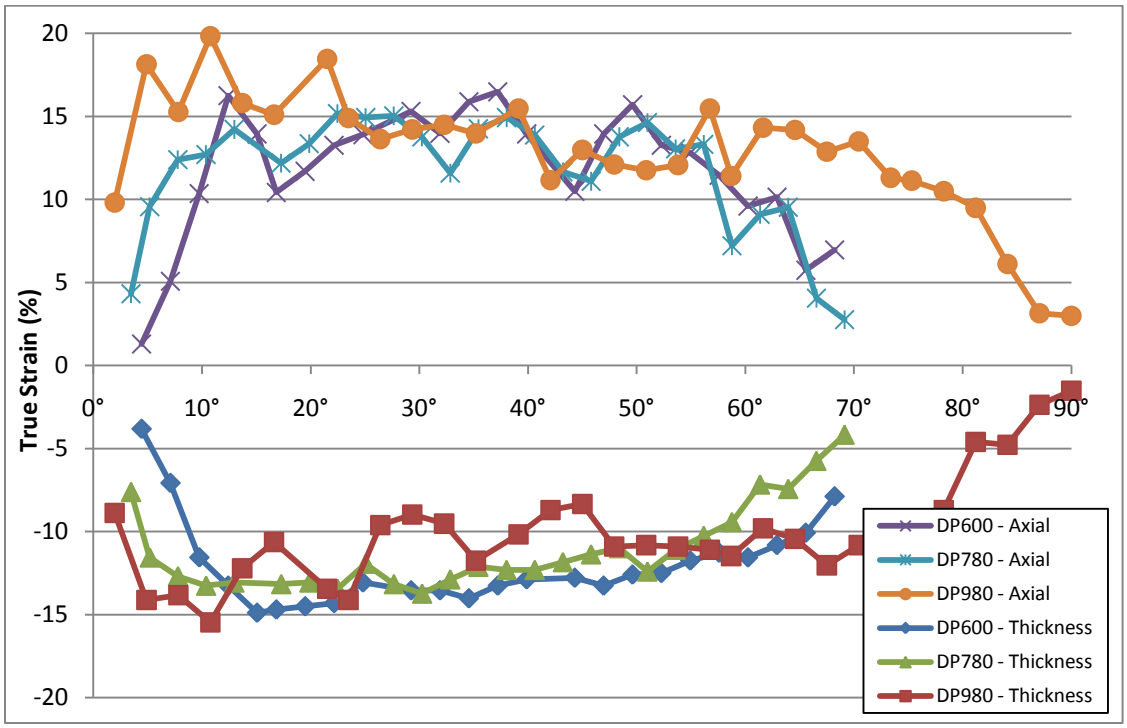

Figure 4.3: Tube extrados strains for each steel grade (bend ratio - 3.1)

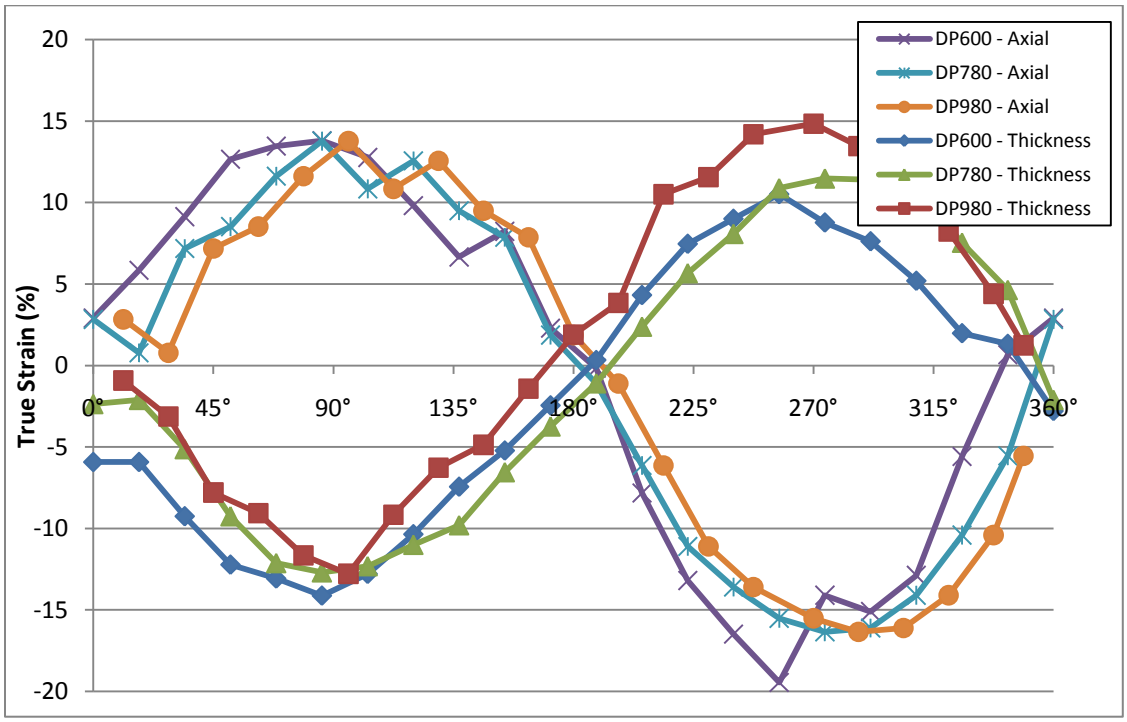

Figure 4.4: Tube circumference strains for each steel grade (bend ratio - 3.1)

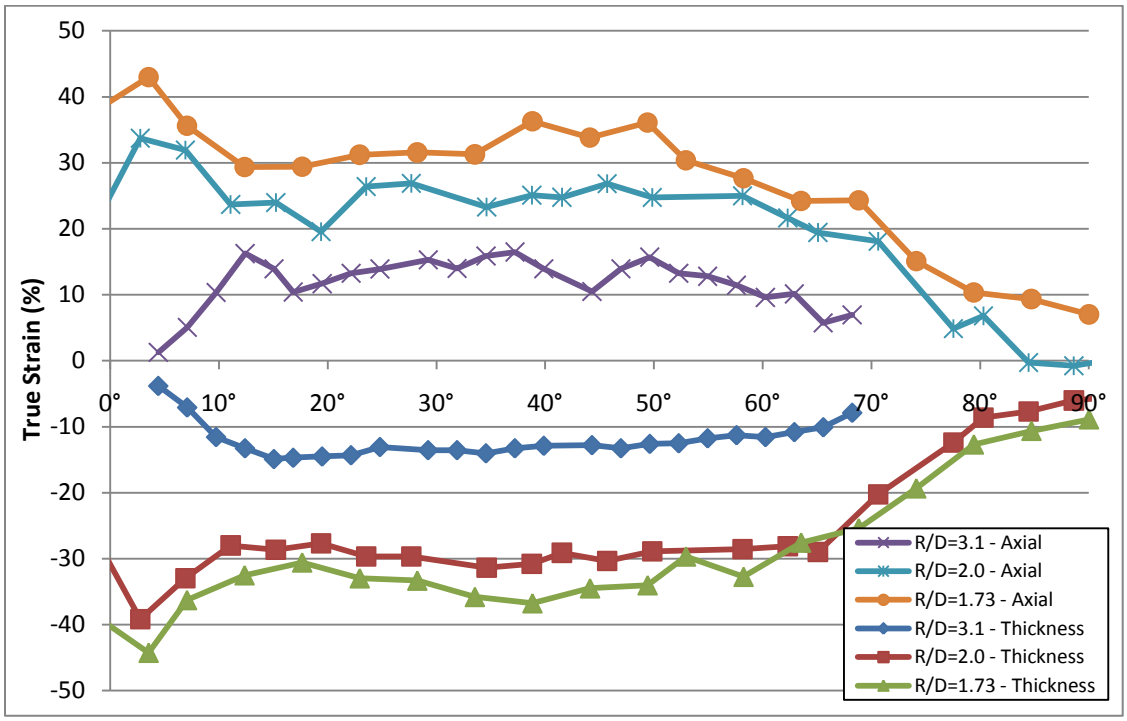

Figure 4.5: DP600 tube extrados strains for each bend ratio

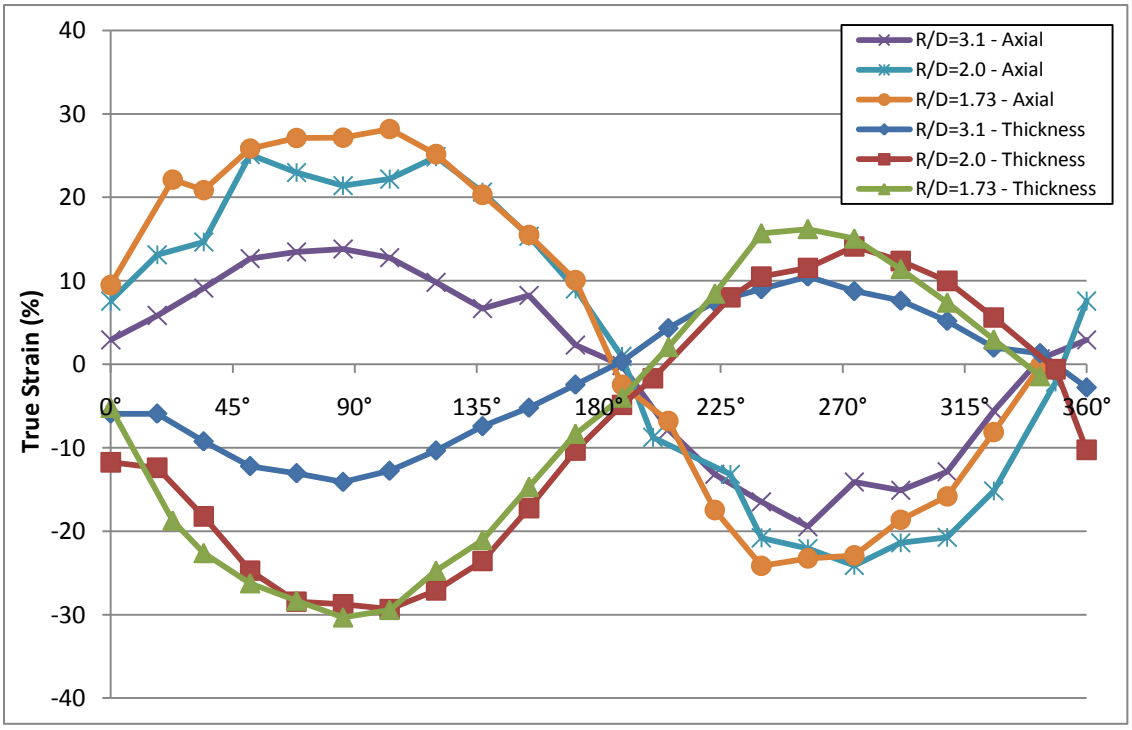

Figure 4.6: DP600 tube circumference strains for each bend ratio

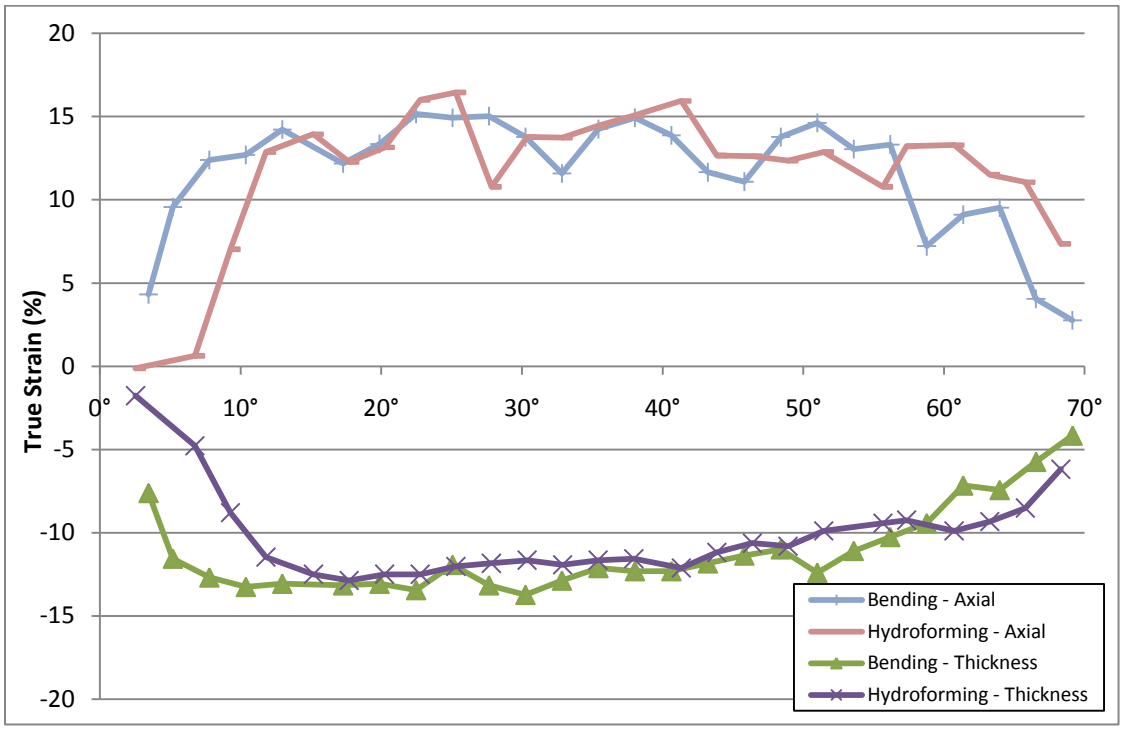

Figure 4.7: DP780 tube extrados strains for bending and hydroforming

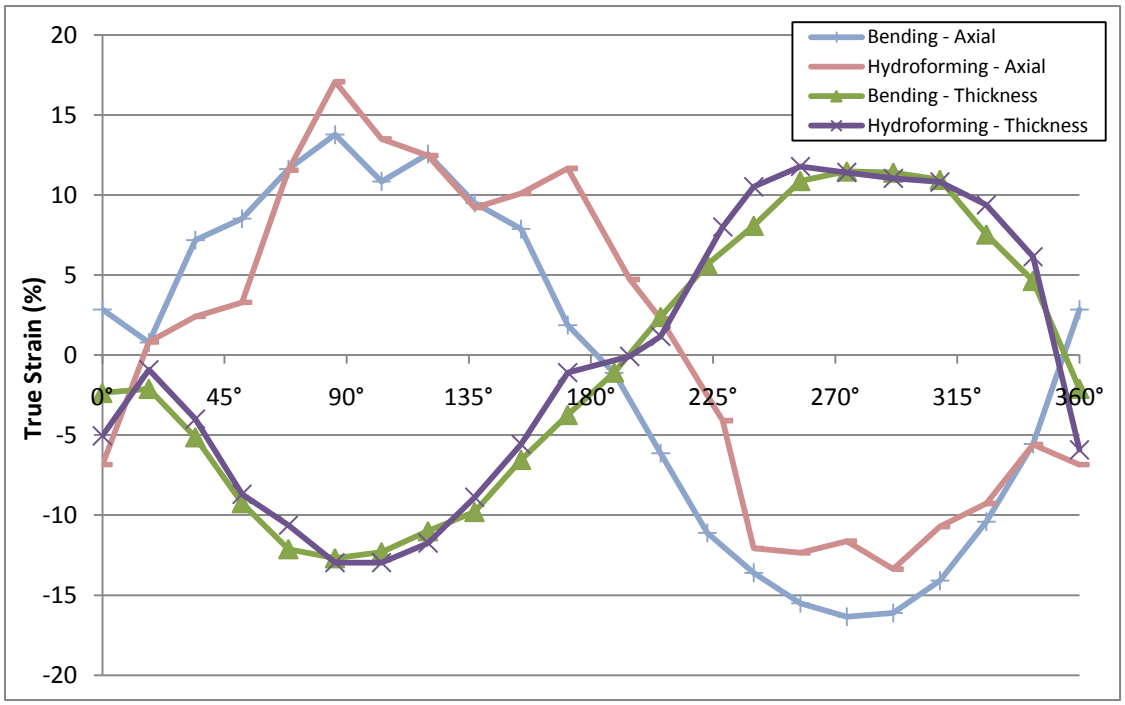

Figure 4.8: DP780 tube circumference strains for bending and hydroforming

4.3 Microstructure

The micrographs seen in Figures 4.9 through 4.15 represent the microstructures observed for each as-received material. The cubes consist of optical micrographs taken from the normal (ND), rolling (RD) and transverse (TD) directions of the steel sheet. They are intended to act only as a representation of the steel, and not a specific volume element within it. The scanning electron micrographs are taken from the normal direction of the sheet and provide enhanced detail of the grain structure and martensite morphology.

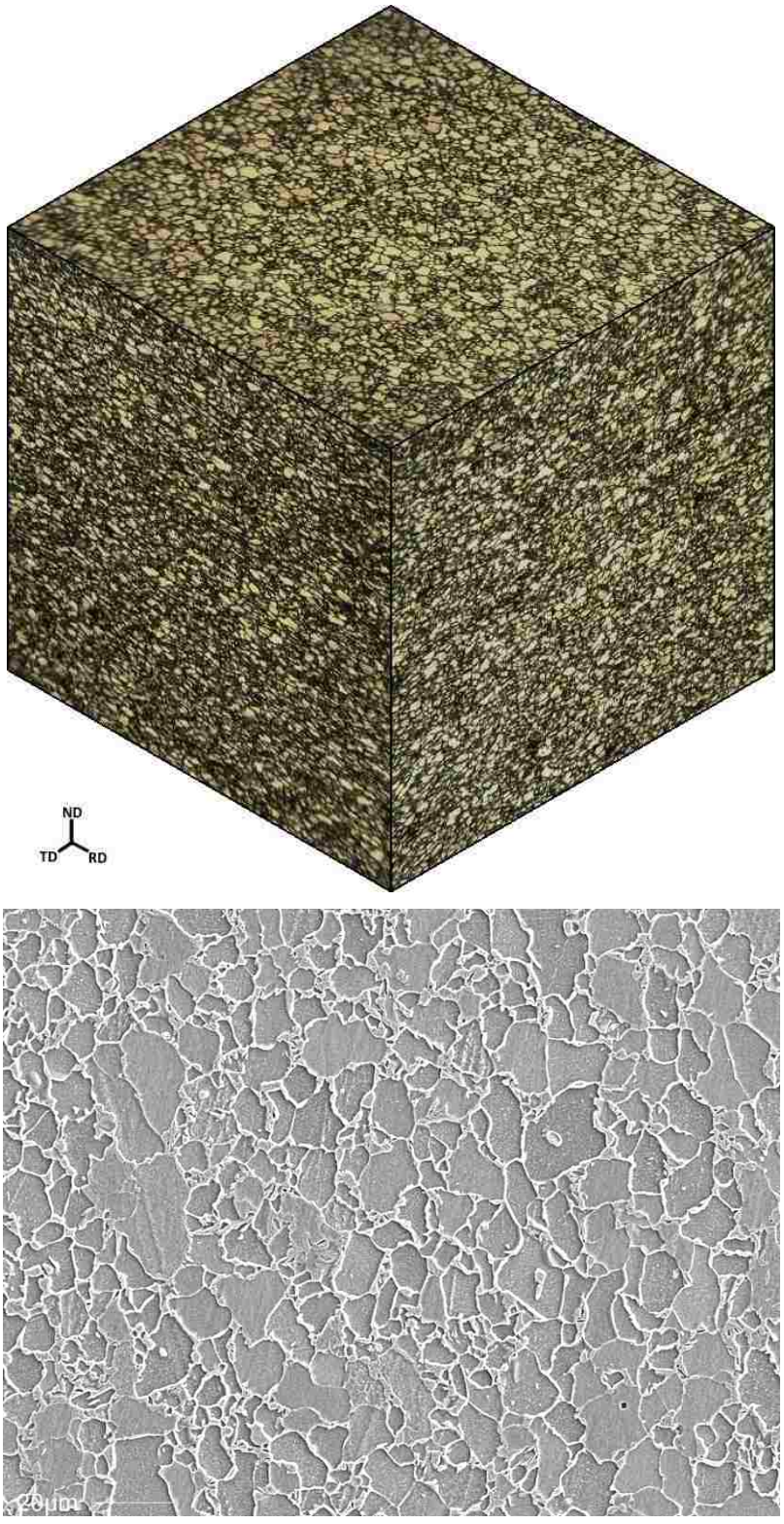

Figure 4.9: Steel 1 (Optical micrographs - 200x, SEM micrograph - 750x)

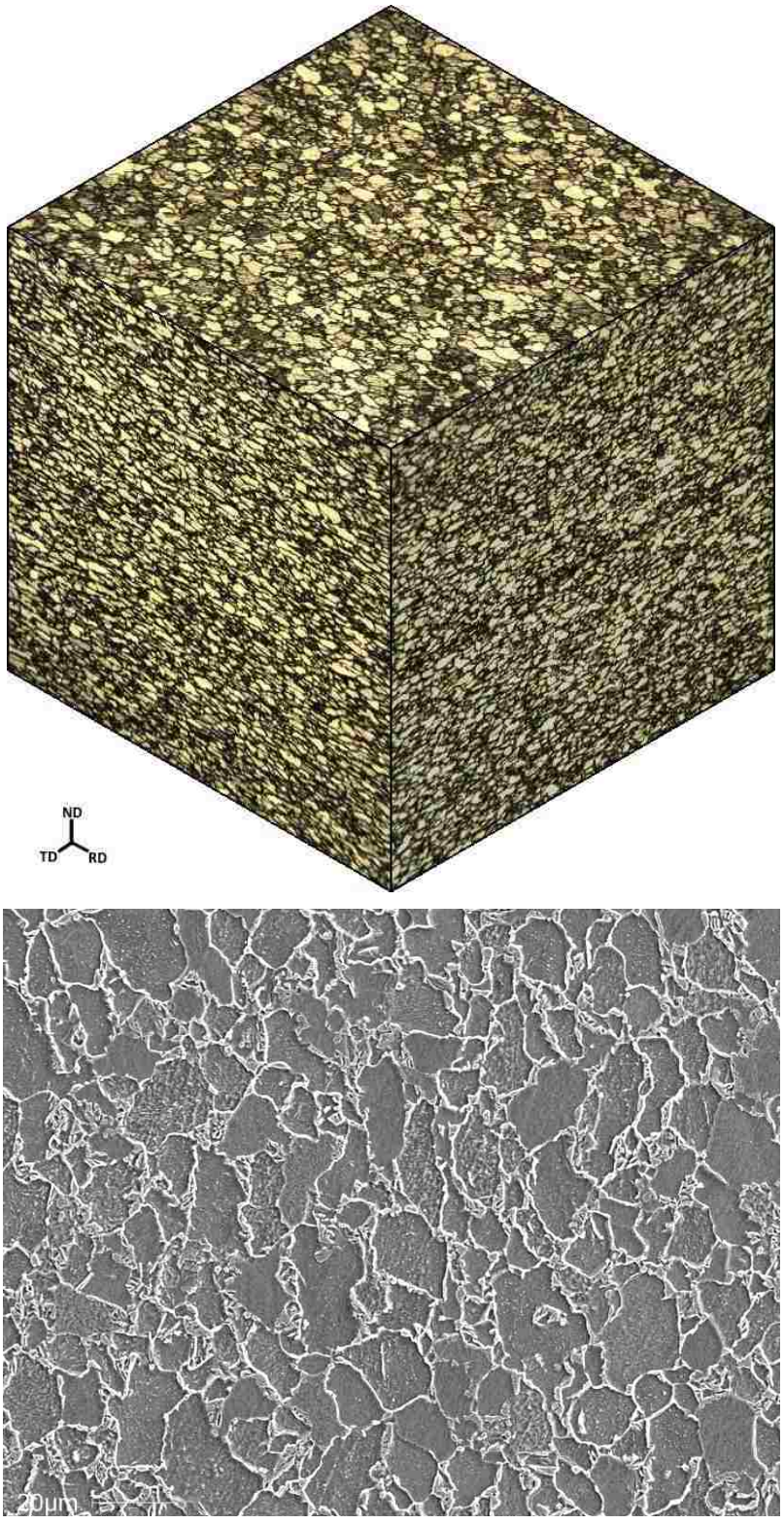

Figure 4.10: Steel 2 (Optical micrographs - 200x, SEM micrograph - 750x)

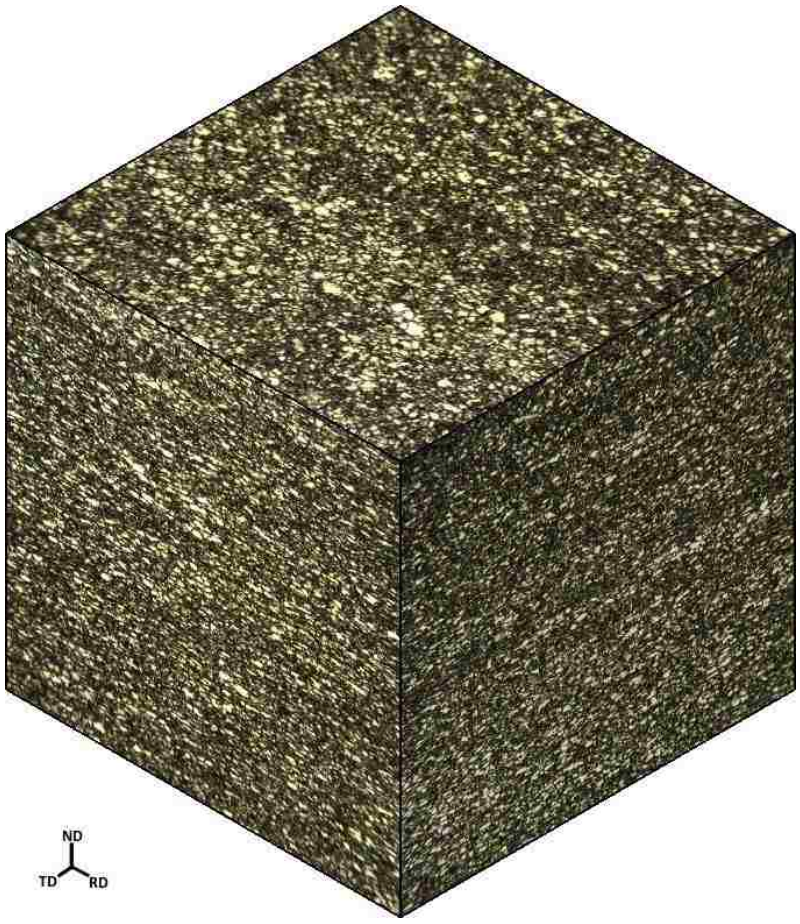

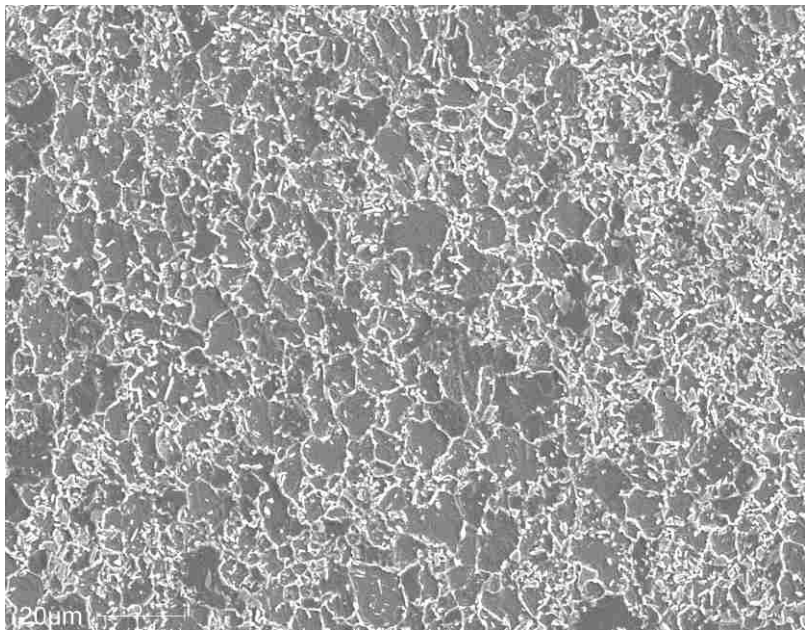

Figure 4.11: Steel 3 (Optical micrographs - 200x, SEM micrograph - 750x)

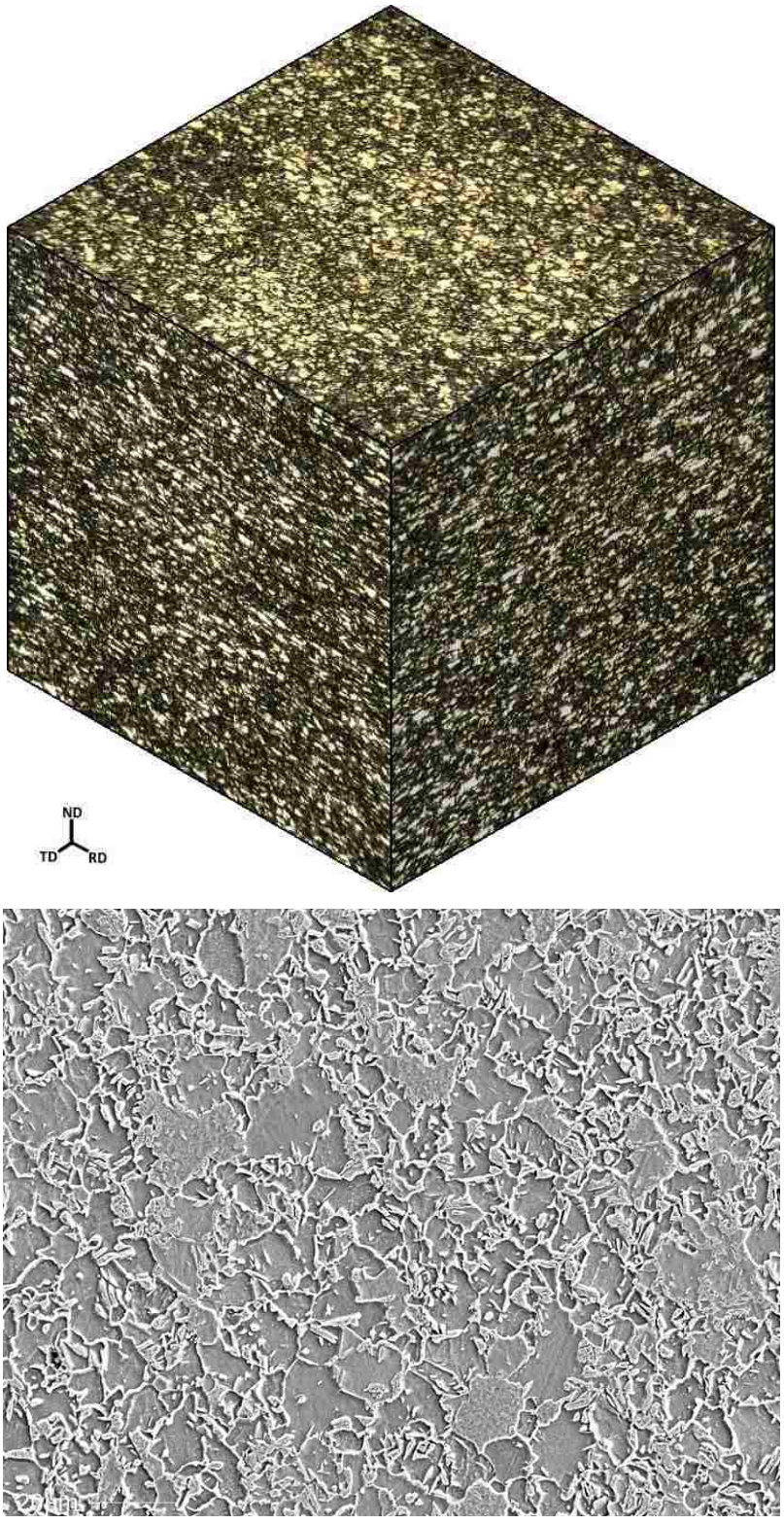

Figure 4.12: Steel 4 (Optical micrographs - 200x, SEM micrograph - 750x)

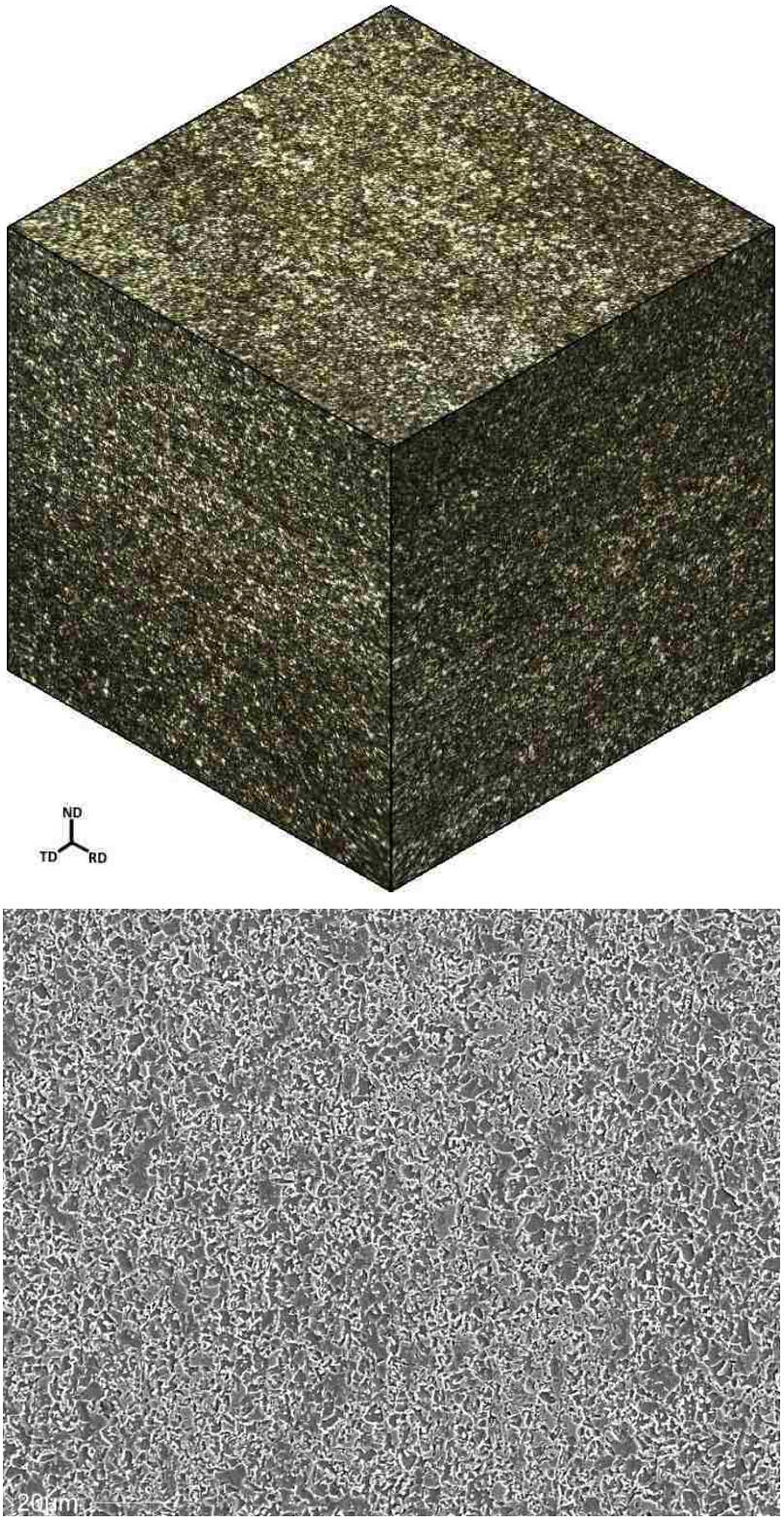

Figure 4.13: Steel 5 (Optical micrographs - 200x, SEM micrograph - 750x)

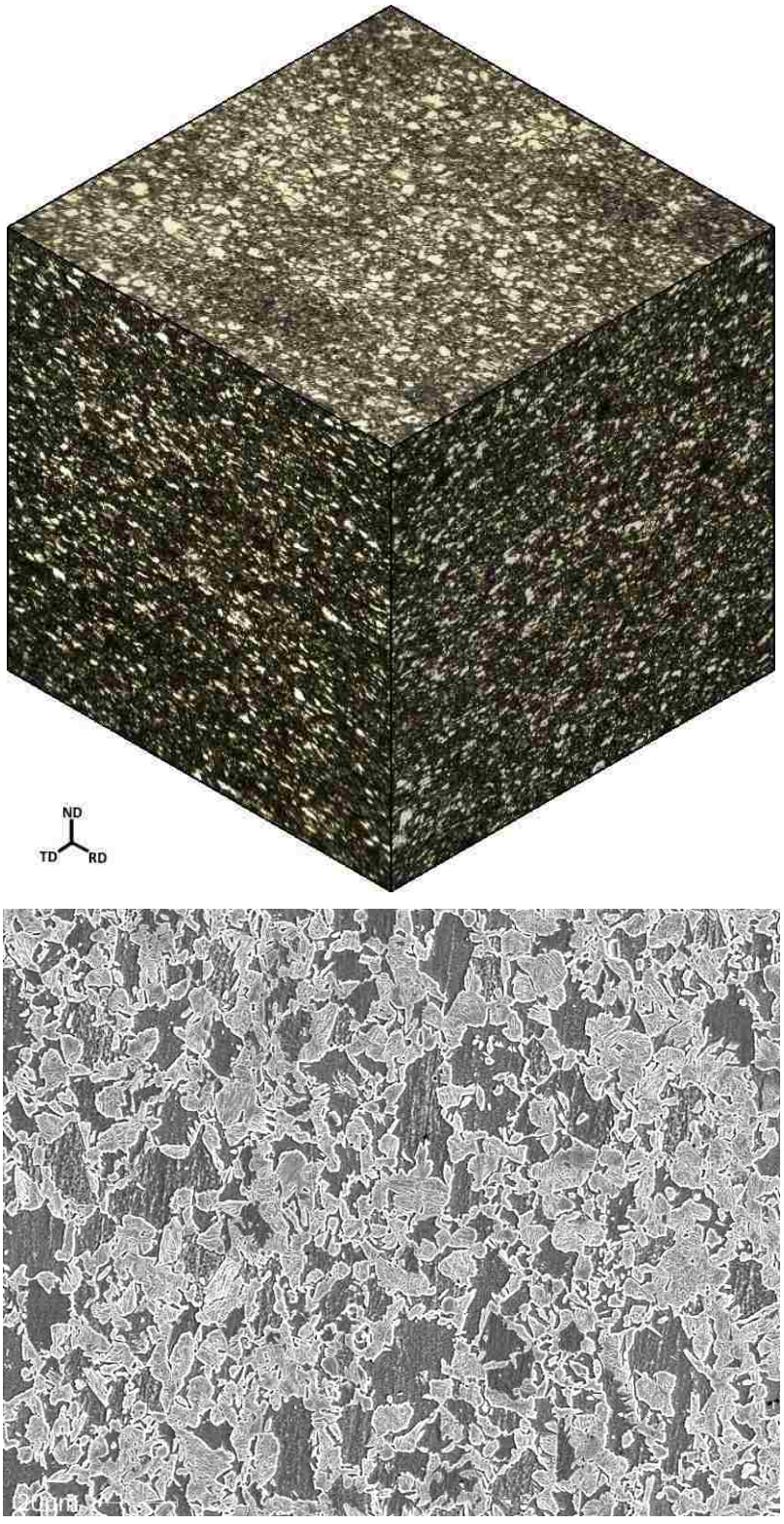

Figure 4.14: Steel 6 (Optical micrographs - 200x, SEM micrograph - 750x)

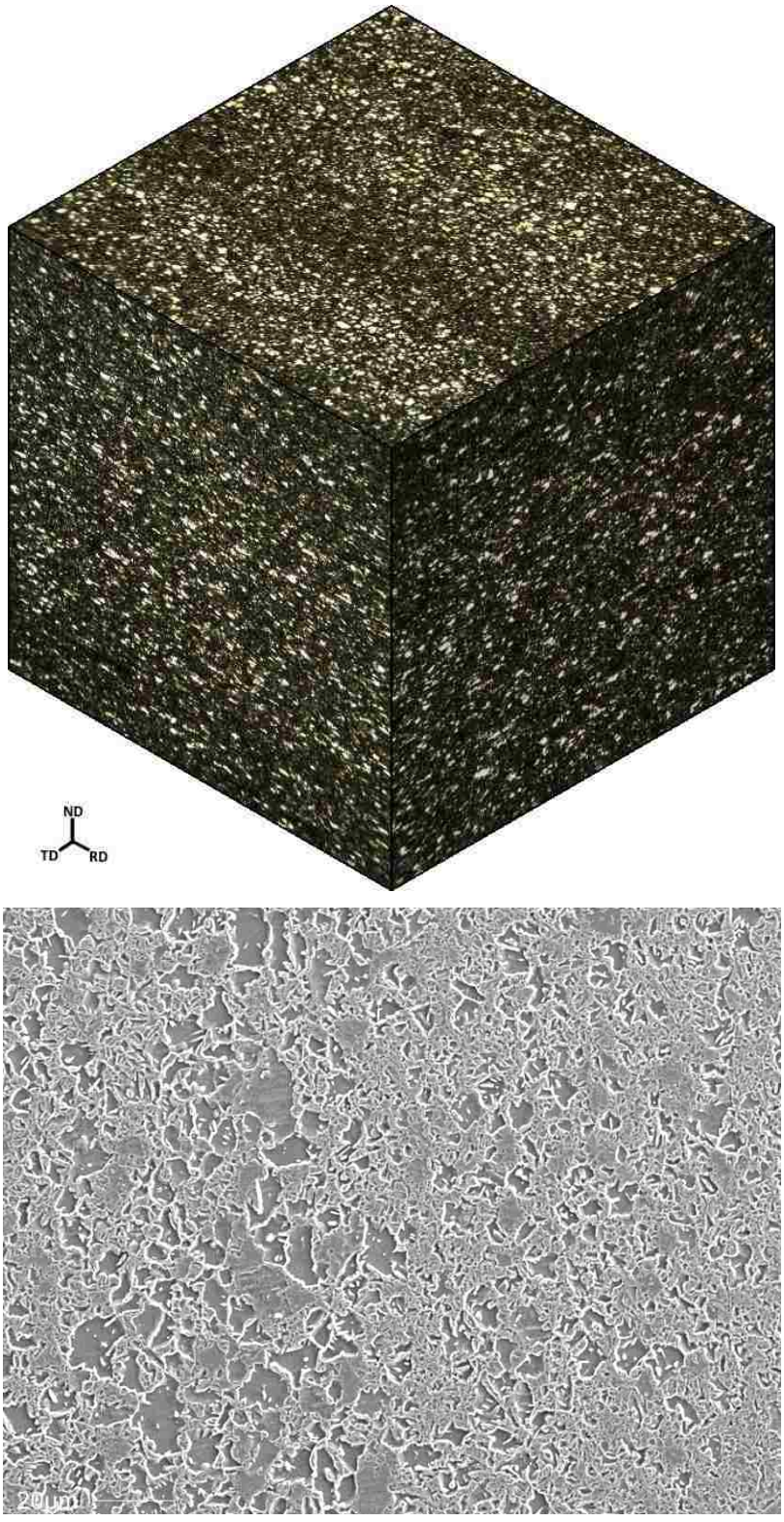

Figure 4.15: Steel 7 (Optical micrographs - 200x, SEM micrograph - 750x)

4.4 Martensite Volume Fraction and Ferrite Grain Size

The values obtained for martensite volume fraction and mean ferrite grain size can be found in Table 4.3. Due to the nature of the martensite morphology, it was not possible to obtain a single number which described the martensite particle size. In general, it can be said that the size of the martensite particles tends to increase as the martensite volume fraction increases and decrease as the ferrite grain size decreases. This can be observed in the micrographs shown in Section 4.3.

	DP600			DP780		DP980	
ID#	1	2	3	4	5	6	7
Martensite Volume Fraction (%)	14.1	16.2	18.5	21.2	26.2	34.6	38.1
Mean Ferrite Grain Size (μm)	8.86	9.36	7.40	8.44	4.89	8.28	6.68

Table 4.3: Martensite volume fraction and mean ferrite grain size of each steel

4.5 Martensite Banding

The anisotropy index values calculated for each steel are presented in Table 4.4. While these results indicate the overall severity of the banding within each material, they do not adequately capture steels with single large martensite bands at the centreline of the sheet. Further discussion on banding, and its impact on mechanical properties can be found in Section 5.2.4.

	DP600			DP780		DP980	
ID#	1	2	3	4	5	6	7
NL⊥ (#/mm)	162	143	181.2	174.6	167.1	176	150.3
NL∥ (#/mm)	141.1	120	124.4	125.4	122.4	144	117
AI (NL⊥/NL∥)	1.15	1.19	1.46	1.39	1.37	1.22	1.28

Table 4.4: ASTM anisotropy index values for martensite banding

4.6 Chemical Composition

The chemical compositions measured for each steel are listed in Table 4.5. The steels fall into two general categories: carbon-manganese, and carbon-manganese plus additional alloying elements. The differences between the two are discussed in Section 5.2.1.

	DP600			DP780		DP980	
ID#	1	2	3	4	5	6	7
C (%)	0.1	0.12	0.09	0.11	0.15	0.16	0.16
Si (%)	0.31	0.4	0.01	0.32	0.2	0.31	0.52
S (%)	0.005	0.004	0.003	0.004	0.004	0.007	0.003
P (%)	0.006	0.014	0.014	0.01	0.012	0.007	0.007
Mn (%)	0.99	0.93	1.81	1.77	1.68	1.42	1.49
Ni (%)	0.01	0.04	0.02	0.01	0.04	0.01	0.05
Cr (%)	0.02	0.04	0.2	0.02	0.42	0.02	0.03
Mo (%)	0	0	0.18	0	0	0	0.01

Table 4.5: Chemical compositions of tested steels

4.7 Micro Hardness

Micro hardness values for each steel can be seen in Table 4.6. As expected, these results correlate well with the macroscopic tensile strengths of the steels. Observation of the indentations under the microscope showed Vickers pyramidal lengths of approximately 38 to 48 μm, much larger than the mean ferrite grain and martensite island size. This indicates that the hardness values obtained are bulk material values and not phase specific.

	DP600			DP780		DP980	
ID#	1	2	3	4	5	6	7
Hardness (HV)	240	244	261	299	295	360	379

Table 4.6: Micro hardness values for each steel

4.8 Nano Hardness

Nano indentation testing was performed on steels 1, 4, and 6. For each steel tested, a series of 64 indentations were made in an eight by eight grid placed within a 30 μm by 30 μm square on the surface of the material. The results, shown in Figures 4.16 through 4.21, have been presented in two ways. First, histograms summarize the number of indentations measured for each range of reduced modulus and hardness values. Second, scanning probe micrographs and corresponding hardness contour maps show the specific locations from which each hardness value was obtained.

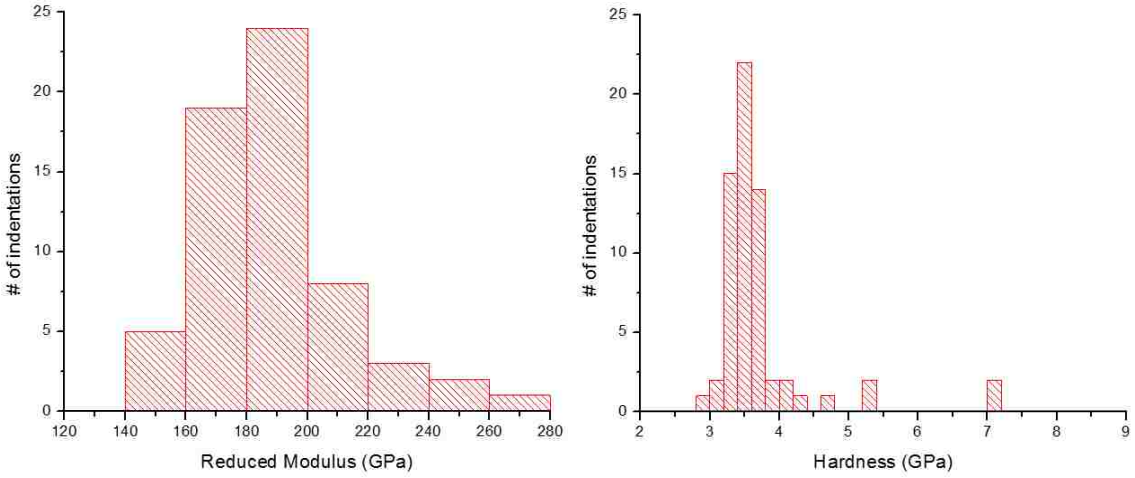

Figure 4.16: Modulus and hardness histograms for steel 1

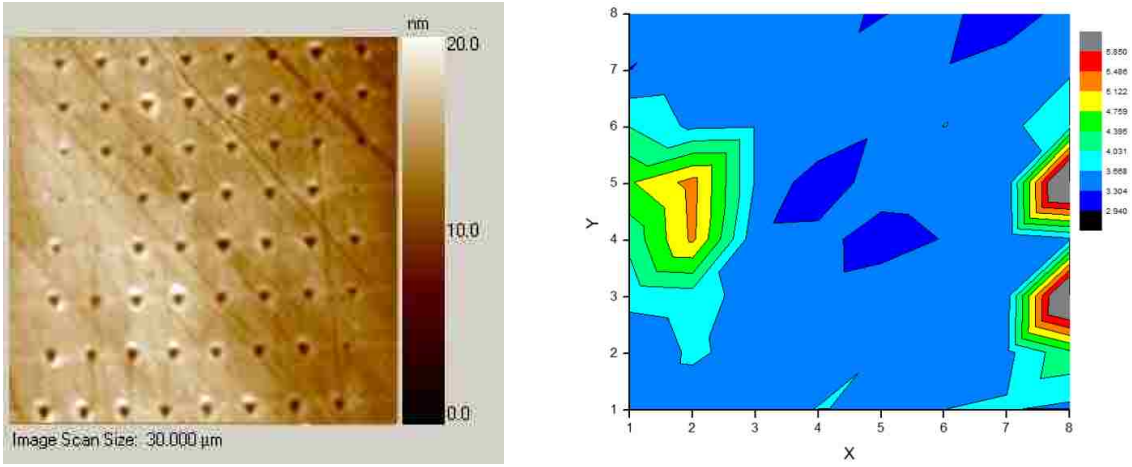

Figure 4.17: SPM image of grid pattern and corresponding hardness contour map for steel 1

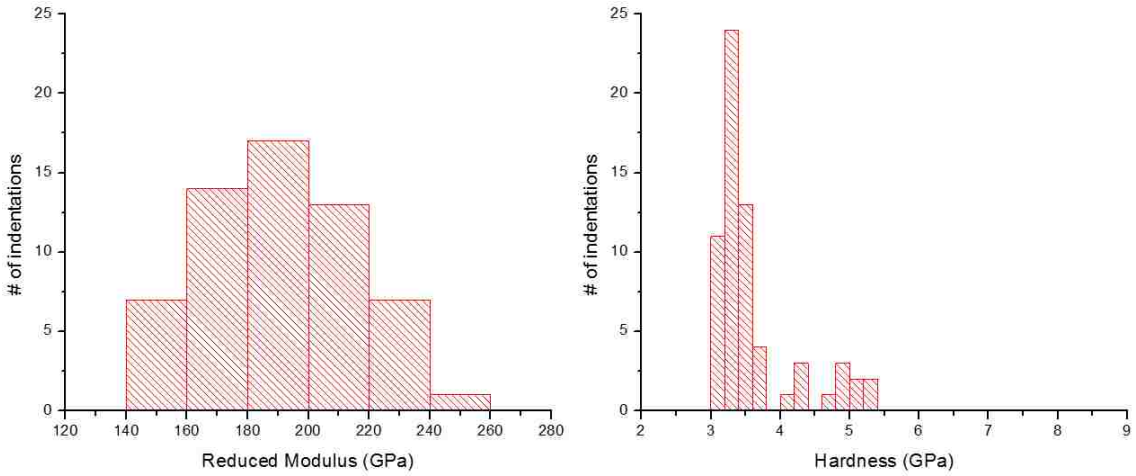

Figure 4.18: Modulus and hardness histograms for steel 4

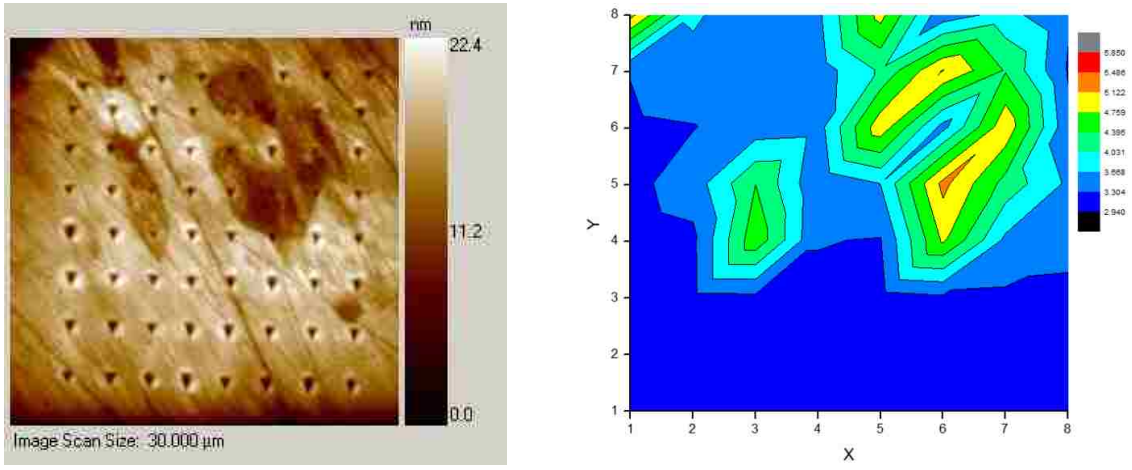

Figure 4.19: SPM image of grid pattern and corresponding hardness contour map for steel 4

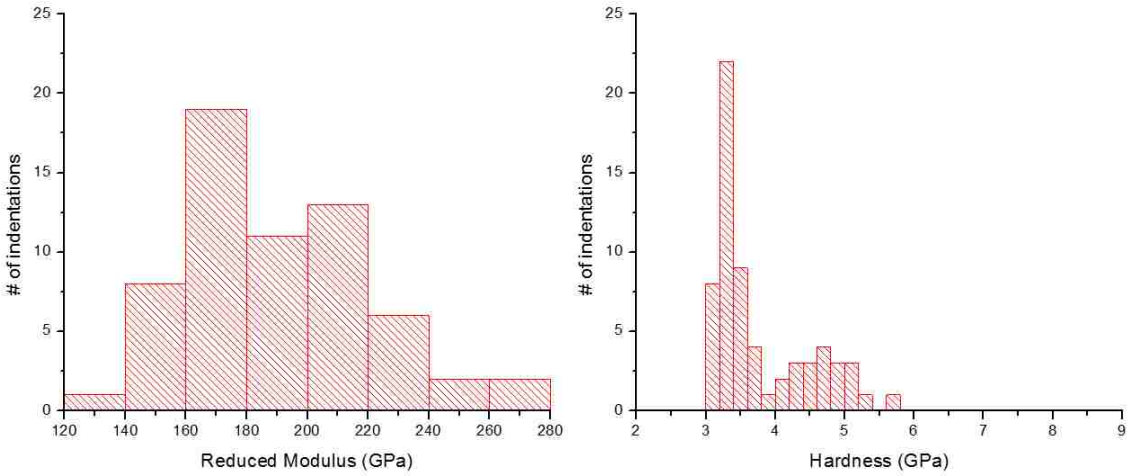

Figure 4.20: Modulus and hardness histograms for steel 6

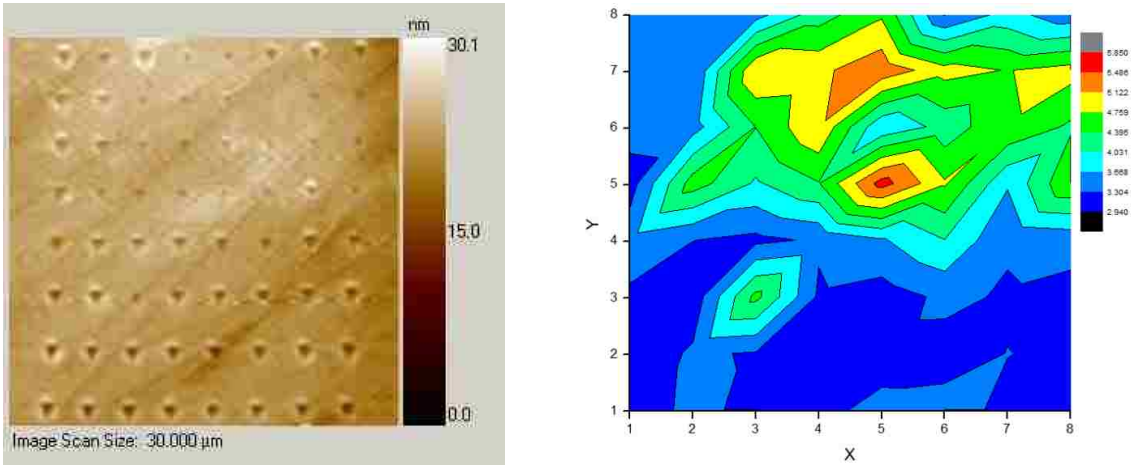

Figure 4.21: SPM image of grid pattern and corresponding hardness contour map for steel 6

Chapter 5:
Discussion of Results

This chapter contains a detailed discussion of the results presented in Chapter 4. It is broken down into the following sections: tube bending and hydroforming, comparison of commercial dual phase steels, and nano indentation testing. A common link is developed between each of these sections, and details of their interrelationships are discussed.

5.1 Tube Bending and Hydroforming

Inspection of Table 4.2 shows that the results of the tube bending process are stochastic in nature. For a given strength grade and bend ratio, there is no guarantee of the same result for multiple tubes. While one tube may be successfully bent, another may fail. For the dual phase steel tubes tested, there appears to be a minimum bend ratio to which the tubes can be reliably and consistently bent. For the DP600 tubes this was found to be 2.0, while the DP780 and DP980 tubes could only be reliably bent using a bend ratio of 3.1. As the bend ratio was decreased, the reliability of the bending process dropped, with a greater percentage of tubes failing.

Observation of the strains in Figure 5.1, taken around the extrados of the bent tube, reveals two distinct strain regions. First, at the clamp side there is a sudden spike in strain for approximately the first ten degrees of the bend. This is the location where the bending impulse is first applied to the tube, initiating the bending process. The severity of this spike was found to be influenced by parameters such mandrel lubrication, mandrel position and bending speed. Following the initial rise in strain, there is a drop off followed by a steady region in which the strains remain constant until they trail off at the end of the bend.

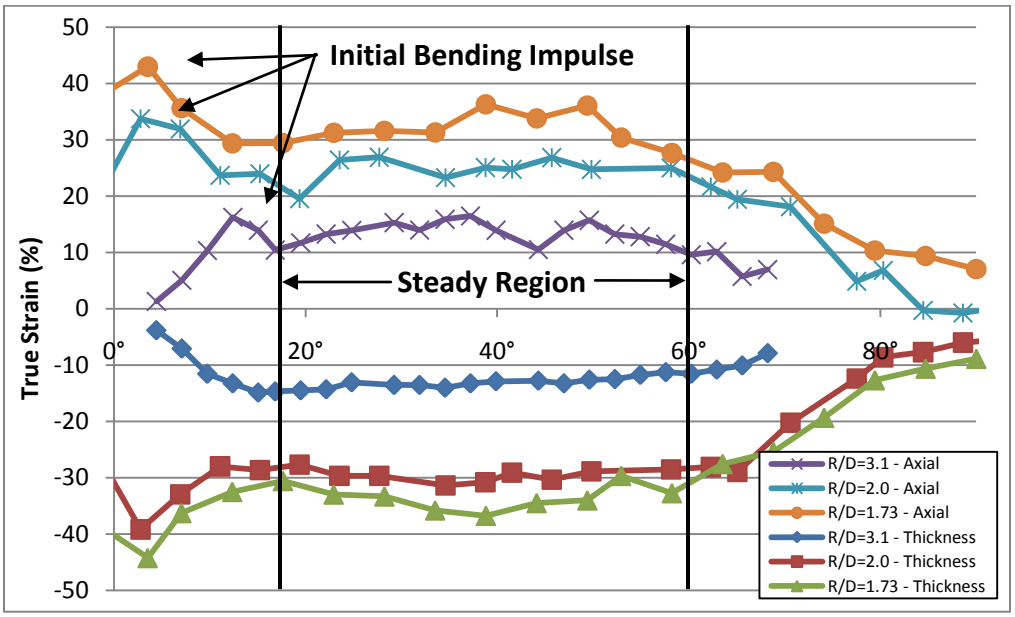

Figure 5.1: Regions of strain in bent tubes

Failures during bending were found to occur in both strain regions, however the majority occurred during steady strain. The angle of the bend at which failures occurred was seemingly random. Different tubes of the same grade bent with the same bend ratio would fail at different angles in the steady strain region. While it is possible that this occurred due to nuances in the bending process, it is more likely that the material itself was the cause.

The few failures that occurred during the initial bending impulse were much more violent in nature than those occurring during steady strain. These failures were often damaging to the bending equipment, such as the case of the DP980 tube seen in Figure 5.2. Given the high strength of the DP980, upon fracture the tube was able to destroy the mandrel before catastrophic failure of the material. Extreme care is required when bending the higher strength steel grades as the tube is not always the weakest link in the process.

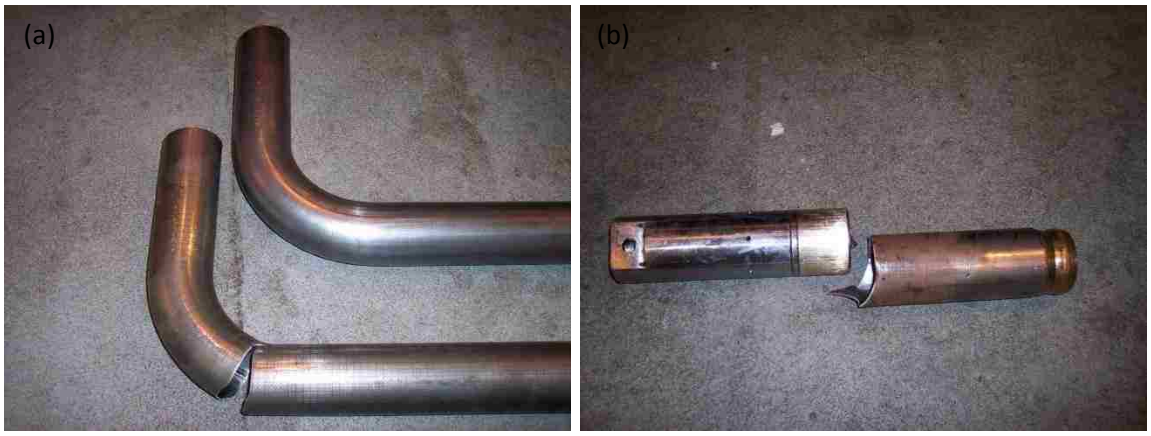

Figure 5.2: Tube failure during (a) steady strain and (b) initial bend impulse

5.1.1 Calculation of Effective Strains

It was observed that nearly all tube failures initiated at the extrados of the bend where the axial strains were positive. Summaries of the strains measured at this location for each steel grade and bend ratio are presented in Tables 5.1 through 5.3. The calculation of the effective strain has been performed using the von Mises yield criterion, according to Equation 5.1.

$$\bar{\varepsilon^{p}} = \sqrt{\frac{2}{3}\left[\left(\varepsilon_1^{p}\right)^2 + \left(\varepsilon_2^{p}\right)^2 + \left(\varepsilon_3^{p}\right)^2\right]} \tag{5.1}$$

where $\bar{\varepsilon^{p}}$ is the effective plastic strain, and ε_1^{p}, ε_2^{p}, and ε_3^{p} are the principal plastic strains [67]. The strain values used in these calculations are the average principal strains taken from the steady strain region of each tube. The approximated effective strains have been determined using the principal strains obtained from Equations 2.2 and 2.3 which assume a plane strain condition in the tube wall.

Bend Ratio - 3.1					
Steel Grade	**# of Tubes Measured**	**Maximum Axial Strain**	**Average Axial Strain**	**Average Effective Strain**	**Approximated Effective Strain**
DP600	6	17.1	12.6	16.0	17.3
DP780	6	18.7	14.3	16.1	17.3
DP980	2	22.2	13.3	13.4	17.3

Table 5.1: True strains measured for a bend ratio of 3.1

Bend Ratio - 2.0					
Steel Grade	**# of Tubes Measured**	**Maximum Axial Strain**	**Average Axial Strain**	**Average Effective Strain**	**Approximated Effective Strain**
DP600	4	40.2	25.1	30.5	25.8
DP780	3	29.6	26.8	28.8	25.8
DP980	-	-	-	-	-

Table 5.2: True strains measured for a bend ratio of 2.0

Bend Ratio - 1.73					
Steel Grade	**# of Tubes Measured**	**Maximum Axial Strain**	**Average Axial Strain**	**Average Effective Strain**	**Approximated Effective Strain**
DP600	3	52.1	29.7	35.6	29.3
DP780	1	33.4	31.4	36.8	29.3
DP980	-	-	-	-	-

Table 5.3: True strains measured for a bend ratio of 1.73

5.1.2 Comparison of Steel Grades

Figures 4.3 and 4.4 show comparisons of the strains measured for each steel grade undergoing bending with the same bend ratio. It is evident that the level of strain experienced by each steel grade is very similar. This is confirmed by comparison of the average effective strains in Section 5.1.1. The strains experienced by dual phase steel tubes undergoing rotary draw bending do not appear to be dependent on the steel grade. This observation confirms what has been described by Khodayari [55], that principal bending strains are a function of bend ratio only and therefore material neutral.

5.1.3 Effect of the Weld Zone

For all bending experiments, the weld zone of the tube was oriented so that it was as close as possible to the neutral axis during bending. Based on tensile testing done on samples cut from tubular material and on the work done by Pavalina et al. [48], it is known that the fusion and heat affected zones generated by the tube welding process have substantially higher strength and lower elongation than the rest of the tube material. Figure 4.6 shows that as you move away from the neutral axis of the bend, the axial strain greatly increases. The lack of elongation at the weld zone causes tube failure if it is exposed to even moderate levels of strain. It is therefore important that the weld be placed as close as possible to the neutral axis. This placement was found to be particularly important for the DP600 and DP780 tubes joined using high frequency electric resistance welding. The heat affected zones on these tubes were nearly double the size of the laser welded DP980 tubes and were more likely to cause tube failures when positioned away from the neutral axis.

5.1.4 Comparison of Strains Before and After Hydroforming

As discussed in Section 2.2.3, the pressure sequence hydroforming process used by Vari-Form does not subject the tube to significant hoop and thickness strains like traditional high pressure hydroforming. The majority of the strain imparted on the tube comes during the pre-bending operation. Strain measurements were taken from tubes after bending and then again after hydroforming. A comparison of these strains for a DP780 tube can be seen in Figure 5.3. It is clear that the strains are very similar and match quite closely when overlaid. The thickness strains measured for the hydroformed tube show no sign of additional thinning as would be expected with a traditional high pressure process. These results confirm that the pressure sequence hydroforming process is well suited to forming high strength steels and that concerns regarding their formability should be focused on the pre-bending operations.

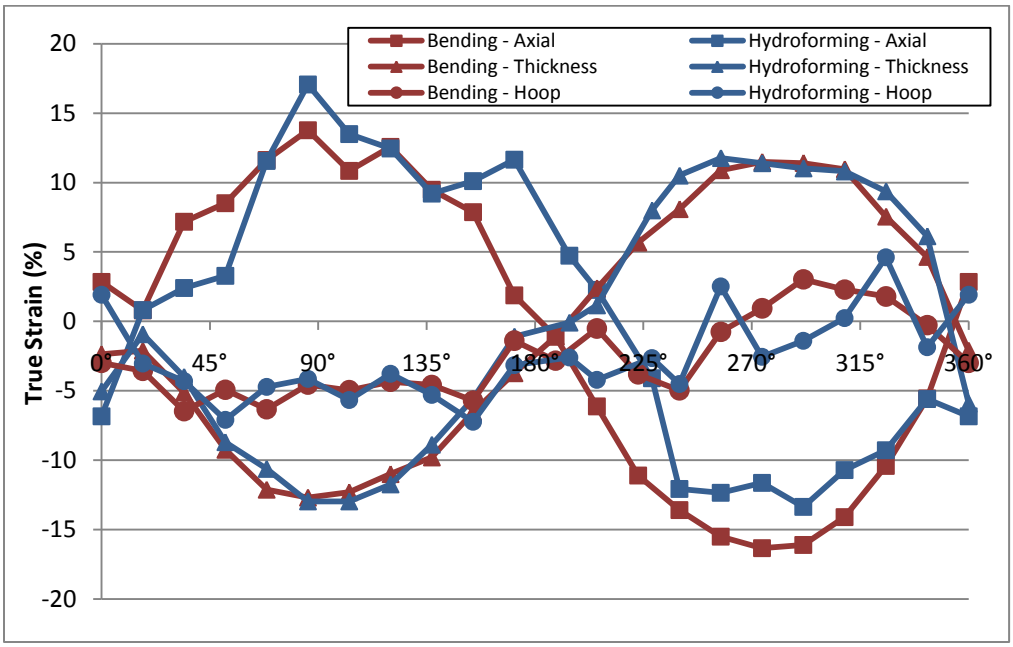

Figure 5.3: Comparison of strains before and after hydroforming for DP780 tube

5.1.5 Microstructural Observation of Bent Tubes

Observation of the microstructure of both failed and successfully bent tubes was carried out in order to identify deformation and fracture mechanisms operating during the tube bending process. As discussed in Section 2.1.7, the deformation behaviour of dual phase steels can vary from ductile to brittle depending on the martensite volume fraction of the material. The DP600 and DP780 tubes, with martensite volume fractions of 14.1% and 21.2% respectively, exhibited exclusively ductile behaviour while the DP980 tubes with 38.1% martensite volume fraction displayed mixed mode behaviour. Figure 5.4 shows a micrograph of the fracture surface of a failed DP980 tube. The presence of quasi-cleavage facets indicate that a brittle mode of fracture is occurring due to the large percentage of martensite contained within the microstructure.

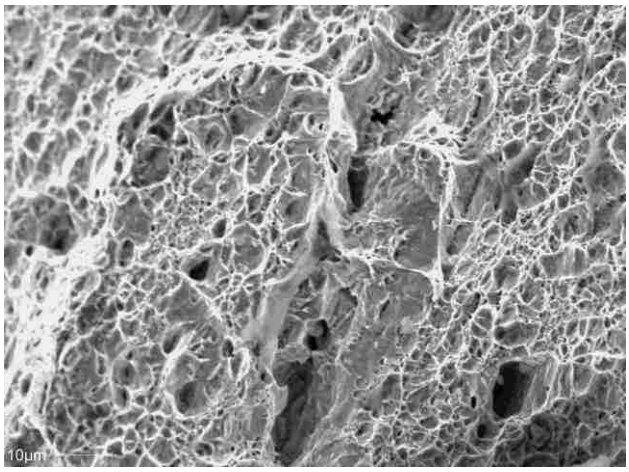

Figure 5.4: DP980 tube fracture surface showing mixed mode behaviour

Ductile deformation and fracture in dual phase steels has been shown to be associated with nucleation, growth and coalescence of micro voids. The mechanisms by which these voids nucleate and grow in samples undergoing uniaxial tension were shown in Section 2.1.7 to be by the fracture and separation of martensite particles at low strains, followed by the decohesion of the ferrite/martensite interfaces at higher strains. Metallographic samples taken from the extrados of the bent tubes show these void nucleation and growth mechanisms to also be functioning in the dual phase steel during tube bending. Figure 5.5 shows examples of these mechanisms occurring. When the micrographs in Figure 5.5 are compared to micrographs taken for uniaxial tensile samples, as seen in Section 2.1.7, it can be concluded that the same void nucleation and growth mechanisms operating in the uniaxial tensile strain state are also functioning in the more complex strain state encountered during tube bending.

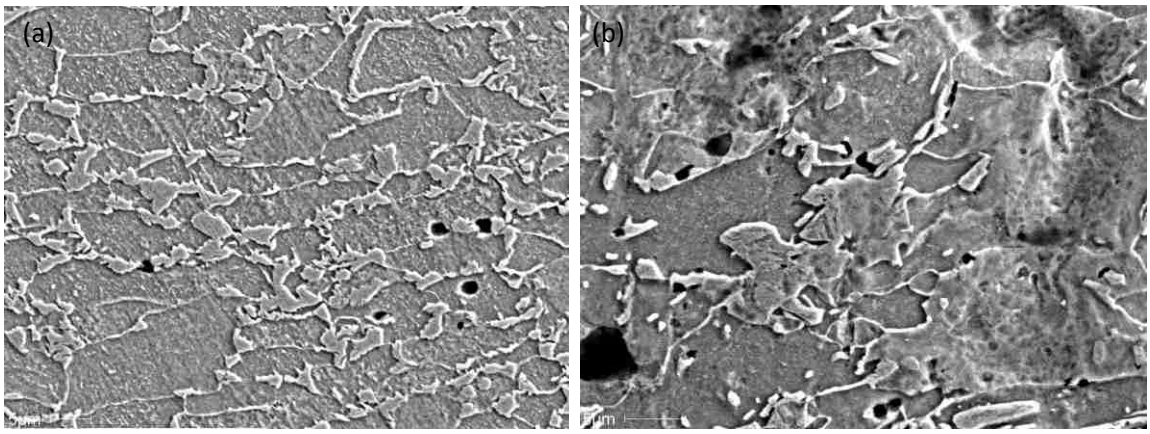

Figure 5.5: Void nucleation by (a) fracture of martensite and (b) separation of interfaces

As illustrated above, the DP980 tubes showed indications of brittle behaviour on their fracture surfaces. This was also observed in metallographic samples taken from the extrados of the DP980 tubes. Figure 5.6 shows both the formation of a large crack opened up on the fracture surface and the cross section of this crack and its path through the microstructure. The crack can be seen taking an intergranular path through the martensite network until it is eventually blunted by converging regions of martensite. This mechanism was not observed in any of the micrographs taken of the DP980 material undergoing uniaxial tensile testing. The crack morphology seen in Figure 5.6 is likely a consequence of the steel's high volume fraction of martensite being exposed to the tube bending strain state.

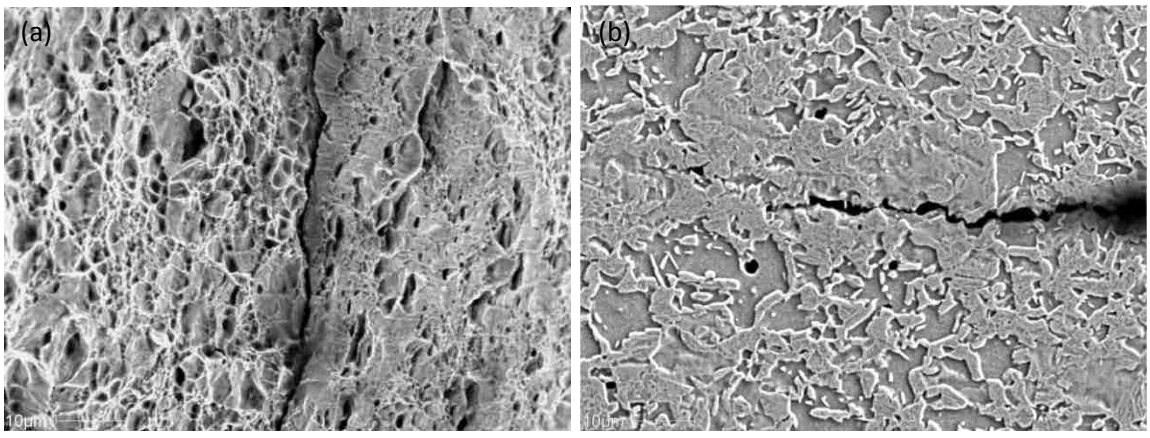

Figure 5.6: DP980 tube (a) fracture surface crack and (b) cross sectional view of crack path

Several researchers have observed the effects of both inclusions and martensite banding on the tensile behaviour of dual phase steels. Park et al. [27] stated that there is a clear indication that martensite bands and inclusions significantly influence the formability of dual phase steels. Broek [68] found that voids attributed to large inclusions gave rise to increased stresses within the material and often determined the location and moment of ductile fracture. The effects of both banding and inclusions within the material were found to manifest themselves on the fracture surface of the failed material. Avramovic-Cingara et al. [42] found that the pattern and size of dimples on the tensile fracture surface reflected the distribution of the martensite within the material. A uniform dimple pattern was observable for interfacial decohesion nucleation sites, while parallel striations reflected void nucleation along martensite bands. Large voids present on the fracture surface indicated void nucleation and growth on inclusion particles. Observation of the fracture surfaces obtained from tubes which failed during bending indicate that the same microstructural issues which influence dual phase steels undergoing uniaxial tension, namely martensite banding and inclusions, also affect dual phase steels undergoing tube bending. Figure 5.7 shows the fracture surfaces of failed DP600 and DP780 tubes. In both micrographs there is clear evidence of large voids nucleated at inclusions, consistent with what has been observed by others in uniaxial tensile samples. Inspection of the DP780 fracture surface shows the tell-tale signs of martensite banding, with long parallel striations through the thickness of the steel. Voids that have preferentially nucleated on the bands are visible on the fracture surface. The DP600 tube does not exhibit these characteristic striations. These findings are explained when the degree of banding, given by the anisotropy index, is considered for both tube materials. As seen in Table 4.4, the anisotropy index for the DP600 is 1.15 and for the DP780 is 1.39. It indicates that the DP780 is in fact much more heavily banded. The effects of this are readily apparent at the fracture surface of the tube.

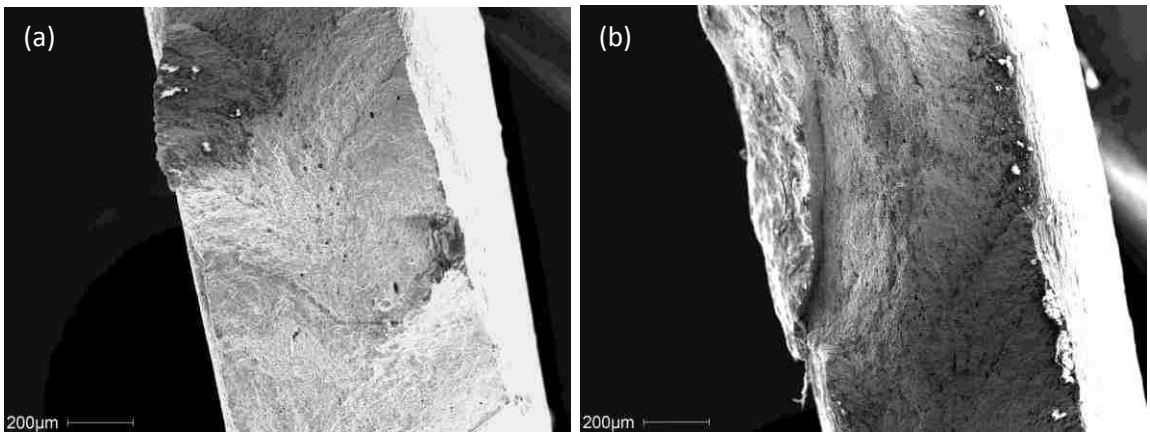

Figure 5.7: (a) DP600 and (b) DP780 tube fracture surfaces

Observation and comparison of the tube fracture surfaces indicates that although the state of strain is different in tube bending as compared to uniaxial tensile testing, the same microstructural features affecting deformation and fracture still apply. For a dual phase steel to perform to its full potential in the tube bending process, it is important that both inclusions and martensite banding be minimized.

5.1.6 Identification of Inclusions in Tube Material

Non-metallic inclusions trapped within steel are typically a consequence of the steelmaking process. They generally arise from the entrapment of slag and deoxidation products used to treat impurities in the steel. Inclusions in the steels used for tube bending were found to be of two types; oxides and sulphides. Figures 5.8 and 5.9 show micrographs of each type of inclusion, along with EDS profiles indicating their chemical composition.

The most common inclusions were found to be sulphides. During the steelmaking process sulphur is present in the form of iron sulphide. Iron sulphide is able to form a eutectic with the surrounding iron which causes it to become segregated at the grain boundaries during cooling. It can weaken the bonding of the grains and contribute to increased brittleness of the steel. In order to avoid this problem steelmakers typically utilize manganese additions to preferentially combine with the sulphur and form manganese sulphide, reducing the detrimental effects of

sulphur. These manganese sulphide inclusions remain in the steel and tend to elongate as the steel undergoes hot rolling. During subsequent plastic deformation, the compatibility between these elongated inclusions and the surrounding steel causes them to act as void nucleation sites. In Figure 5.8, the areas associated with manganese sulphide show clear indications of nucleated voids. These are likely the predominant nucleation sources for the large voids seen on the fracture surfaces of the tubes.

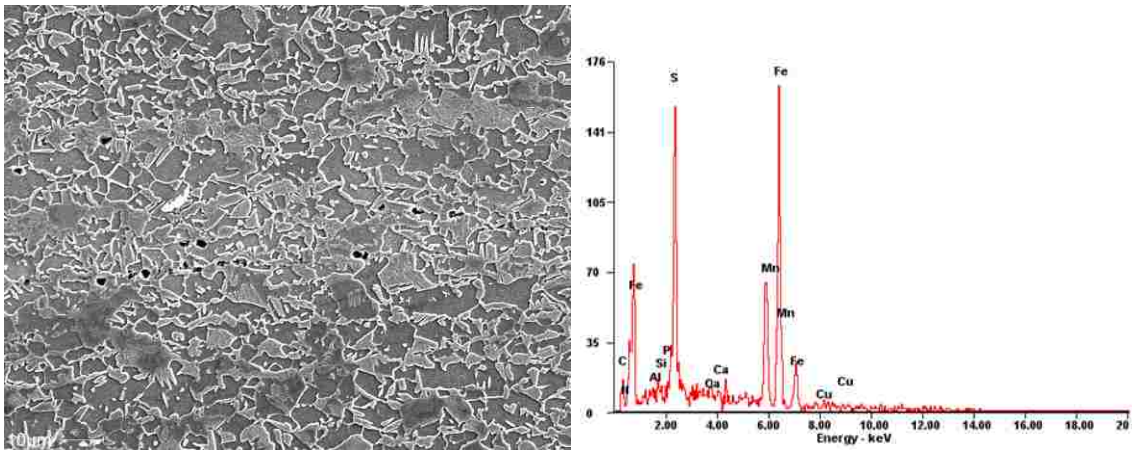

Figure 5.8: Voids nucleated along rolling direction at sulphide inclusions

Less common, but much larger in size, were oxide inclusions. These oxides were found to include aluminum and calcium. Dual phase steels are generally aluminum killed, meaning that aluminum is added to the molten steel prior to solidification to deoxidize the material and form slag. Small particles of slag trapped within the steel upon solidification become excellent sites for the nucleation of voids. Oxide inclusions are much harder than the steel and are only weakly bonded to the surrounding material. Upon application of strain, voids can easily nucleate at their interfaces.

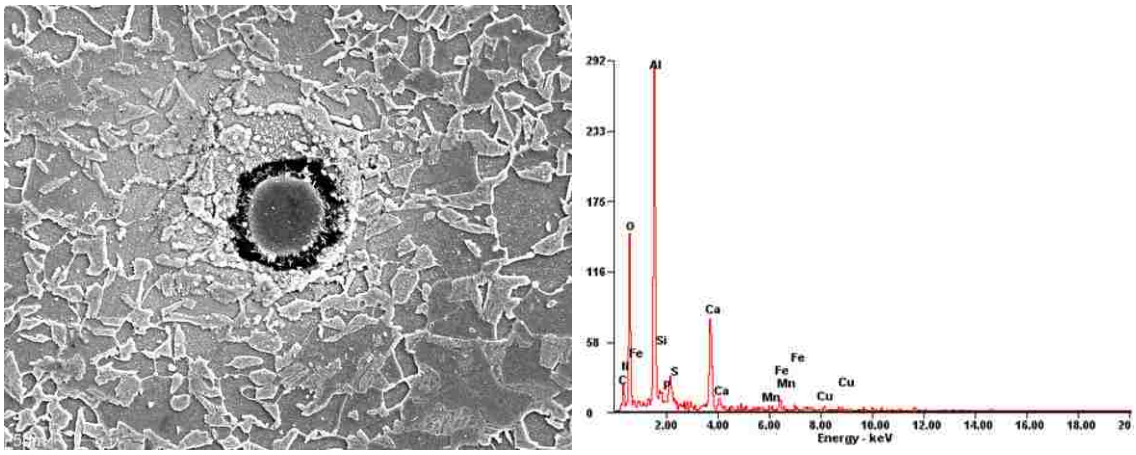

Figure 5.9: Large oxide inclusion

Given the limited number of oxide inclusions which were found within the dual phase steels, it is much more likely that the sulphide inclusions were the primary cause of reduced mechanical behaviour. The effects of sulphide inclusions on dual phase steels have been commented on by other researchers. Avramovic-Cingara et al. [42], Chawla et al. [69] and Szewczyk et al. [70] all found that sulphide inclusions played a role in the fracture of dual phase steels. This was observed first hand in the case the DP600 tube seen in Figure 5.10. This tube did not fracture catastrophically, but instead formed a small neck on its surface. Upon removing the necked area from the tube and observing it utilizing EDS analysis, it was found that the area contained high levels of calcium and sulphur. This is likely a consequence of the desulphurizing process used during steelmaking. Calcium oxide is often added to remove sulphur from the steel and form a calcium sulphide slag. It is possible that some of this slag became trapped and was still present in the steel after solidification. The presence of these calcium sulphide inclusions inside the microstructure was likely the reason for the localized failure seen on the tube.

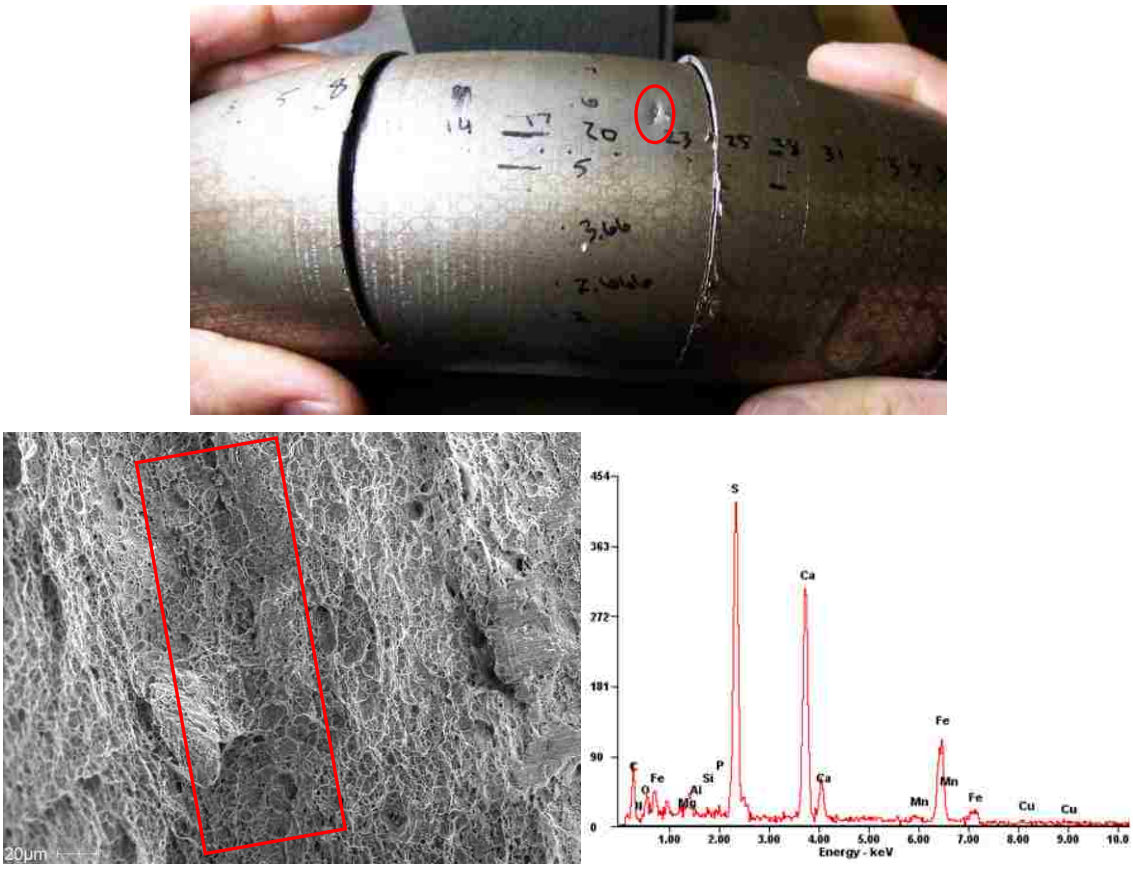

Figure 5.10: Localized tube failure with fracture surface micrograph and EDS profile

5.2 Comparison of Commercial Dual Phase Steels

Although the materials used in this work fall under only three different strength grades, it is apparent from Figure 4.1 that the actual strengths and elongations of the steels are underestimated to varying degrees by each steel producer. This underestimation is important, as it directly impacts the forming process. Steels exhibiting higher strengths than indicated by the supplier will require the application of greater forces and pressures during the tube bending and hydroforming processes. Additionally, if the tubes posses greater elongation than that indicated by the supplier, their reliability during forming may be increased.

5.2.1 Chemical Compositions

Table 4.5 shows that the commercial steels tested fall into two categories, carbon-manganese and carbon-manganese plus additional alloying elements. These additional alloying elements consist primarily of chromium and molybdenum, indicating that they were added for heat treatment purposes as opposed to strengthening via precipitation hardening. Although Lis et al. [12] commented that alloying elements such as molybdenum are rarely added to commercial dual phase steels due to cost, it was found to be present in steel 3. The presence of molybdenum, along with the relatively high manganese content indicates that the producer of steel 3 likely utilized a continuous annealing line which did not allow for the necessary fast cooling rates required to form the dual phase microstructure using the low alloy steel compositions used by the other suppliers.

Commercial continuous annealing lines generally contain cooling systems which utilize either hydrogen gas jet cooling or water quenching. Water quenching can achieve substantially faster cooling rates and therefore produce martensite in dual phase steels containing much lower concentrations of alloying elements. The primary benefit of using low alloy dual phase steels is cost; however, a reduced alloy content can also give the steel better weldability and galvanizing behaviour [71].

Although specific heat treatment parameters are proprietary information and therefore not available from the steel producers, it is still possible to obtain estimates of these values based on the public work of other researchers. Tobiyama et al. [72] have shown that the empirical formulas developed by Andrews [73] can be used to approximate the A_{c1}, A_{c3}, and martensite start temperatures for low carbon dual phase steels. These formulas are presented in Equations 5.2 through 5.4.

$$A_{c3}(°C) = 910 - 203[C]^{1/2} - 15.2[Ni] + 44.7[Si] + 104[V] + 31.5[Mo] + 13.1[W] \quad (5.2)$$

$$A_{c1}(°C) = 723 - 10.7[Mn] - 13.9[Ni] + 29[Si] + 16.9[Cr] + 290[As] + 6.38[W] \quad (5.3)$$

$$M_s(°C) = 539 - 423[C] - 30.4[Mn] - 17.7[Ni] - 12.1[Cr] - 7.5[Mo] \quad (5.4)$$

These equations were used to calculate the A_{c1}, A_{c3}, and martensite start temperatures for each commercial steel. Calculated temperature values are presented in Table 5.4. Based on these values, it appears that the intercritical temperature range for all of the steels is fairly similar. The greatest differences seem to be present in the martensite start temperatures.

	DP600			DP780		DP980	
ID#	1	2	3	4	5	6	7
A_{c3} (°C)	859.5	857.0	854.9	856.8	839.7	842.5	851.6
A_{c1} (°C)	721.6	724.8	707.0	713.5	717.4	717.0	721.9
M_s (°C)	466.2	458.8	441.8	438.2	418.7	427.7	424.7

Table 5.4: Calculated values for A_{c1}, A_{c3}, and M_s

Cooling rates are much more difficult to estimate, and therefore only general comparisons between similar steels are possible. An equation has been developed by Irie et al. [74] to describe the manganese equivalent of low carbon steel containing additional alloying elements critical to heat treatment. Equation 5.5 illustrates that both chromium and molybdenum are more effective in reducing the critical cooling rate as compared to manganese.

$$[\mathrm{Mn}]_{\mathrm{eq}} = [\mathrm{Mn}] + 1.3[\mathrm{Cr}] + 2.67[\mathrm{Mo}] \tag{5.5}$$

The manganese equivalent for each of the commercial steels has been calculated in Table 5.5. These values, combined with the knowledge of the carbon content of each steel indicate that the critical cooling rates of steels 3 and steel 5 are likely lower than the other steels. Beyond this simple inference, it is not possible without more detailed thermo-mechanical experimentation to obtain quantitative knowledge of the cooling rates used by the steel producers.

	DP600			DP780		DP980	
ID#	1	2	3	4	5	6	7
Manganese (%)	1.0	0.9	1.8	1.8	1.7	1.4	1.5
Manganese Equivalent (%)	1.0	1.0	2.6	1.8	2.2	1.4	1.6

Table 5.5: Calculated values for Mn_{eq}

5.2.2 Discontinuous Yielding

One of the key features of dual phase steels is their continuous yielding behaviour. By eliminating yield point elongation normally found in mild and high strength low alloy steels, finished parts are able to be produced with more uniform strain distributions [20]. As described in Section 2.1.5, the absence of yield point elongation in dual phase steels is due to the large number of free mobile dislocations created within the microstructure upon heat treatment. From the tensile curves seen in Figure 4.1, it is apparent that both the DP600 and DP780 steels from supplier A demonstrate signs of discontinuous yielding. It indicates that the heat treatment used by this supplier included a tempering step following quenching.

Specimens which have been tempered show discontinuous yielding behaviour due to the diffusion of interstitial solute atoms to the free dislocations generated during intercritical annealing. Gunduz [75] showed that for tempering temperatures between 100 °C and 600 °C, that discontinuous yielding began to reappear somewhere between 200 °C and 300 °C. Comparison of the tensile curves obtained from supplier A's steels to those generated by Gunduz, seen in Figure 5.11, gives some indication of the degree to which supplier A tempered their steels. The DP600 from supplier A appears to have received a greater level of tempering than the DP780.

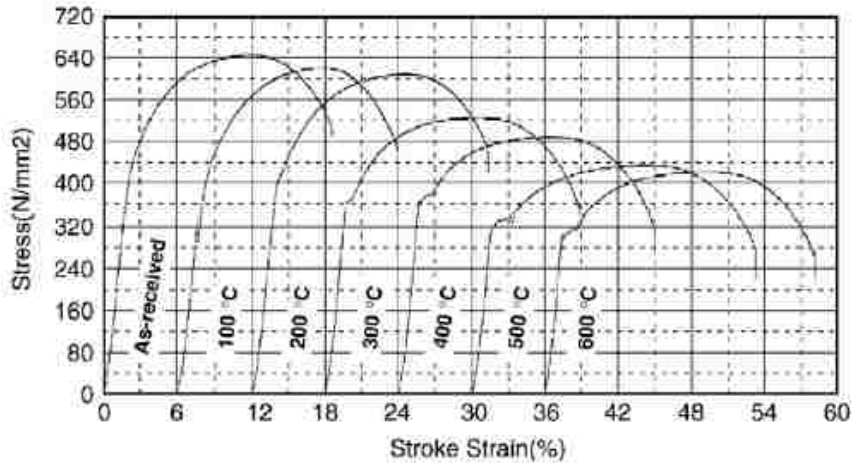

Figure 5.11: Effect of tempering temperature on tensile behaviour [75]

Tempering of dual phase steel sheet can often occur during the galvannealing process, in which the steel is heated to promote interdiffusion between the base material and the zinc coating. The steel sheet used in this work was not zinc coated and therefore the reason for this tempering is likely a function of the intercritical annealing process of supplier A. Fang et al. [76] showed that the tensile strength of a dual phase steel decreases with increasing tempering temperature, while both the uniform and total elongations increase. It is possible that in order to achieve finished steel with both the desired strength and elongation, that producer A subjected their steel to a tempering treatment after intercritical annealing. The chemical composition results discussed in Section 5.2.1 also seem to support this fact. Rashid [22] commented that the extent of autotempering is lower in water quenched dual phase steels and that ductility is usually improved in these steels at the expense of strength by a short tempering treatment below 500 °C. The lack of alloying elements in the DP600 and DP780 of producer A indicates that they were probably subjected to water quenching. It therefore seems likely that they were made to undergo tempering after quenching in order to obtain the required strengths and elongations.

5.2.3 Correlation of Mechanical and Microstructural Properties

In order to characterize the effects of microstructural differences on the mechanical properties of the commercial dual phase steels, plots were generated to determine levels of correlation. From the review presented in Section 2.1.4, it is known that martensite volume fraction is generally considered to be the most important parameter influencing the mechanical properties of dual phase steels. For the steels examined in this work, Figures 5.12 and 5.13 plot strength and elongation against martensite volume fraction.

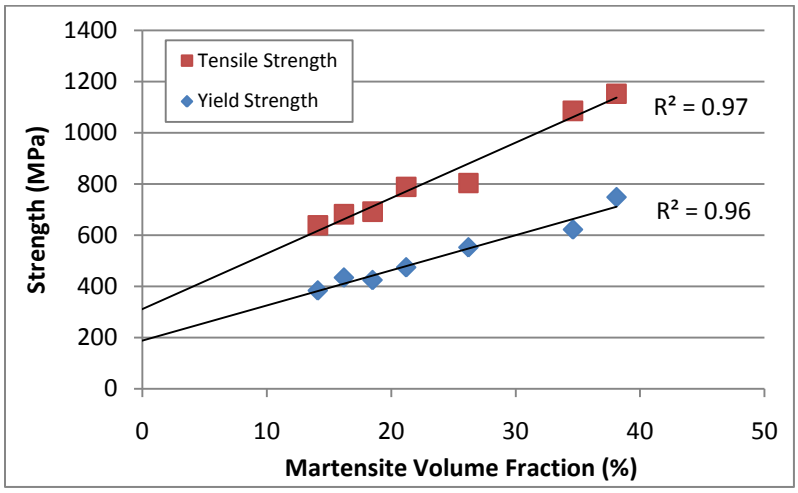

Figure 5.12: Comparison of yield/tensile strength vs. martensite volume fraction

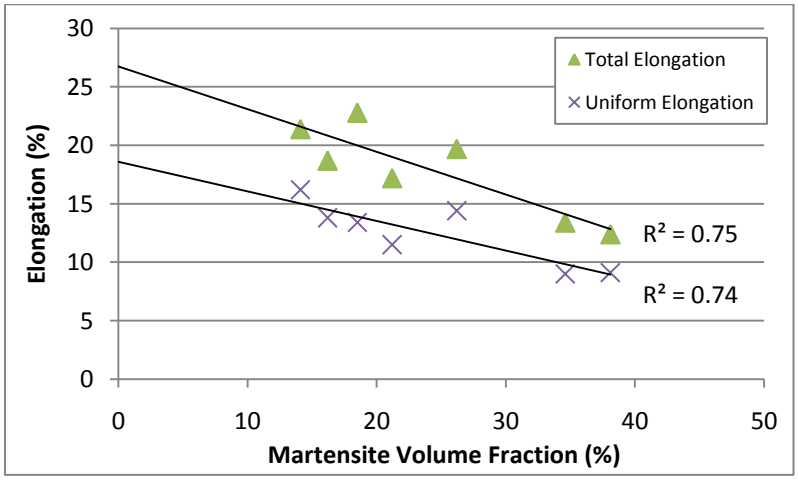

Figure 5.13: Comparison of uniform/total elongation vs. martensite volume fraction

As expected, the general trend shows that as the martensite volume fraction is increased both yield and tensile strength increase, while uniform and total elongation decrease. When a linear regression is performed on each data set, it becomes apparent that the correlation between strength and martensite volume fraction is quite good, while the correlation between elongation and martensite volume fraction is not. It seems to match the findings of both Mazinani et al. [31] and Korzekwa et al. [35] who showed that strength was a linear function of martensite volume fraction while elongation was not. Mazinani et al. commented that the strength of a dual phase steel was only affected by the volume of martensite in the

microstructure and fairly insensitive to changes in the morphology of that martensite. Elongation on the other hand was directly affected by both the shape and distribution of the martensite, with banded microstructures being the most detrimental to performance. As such, it is apparent that the commercial steels tested in this work exhibit differences that are related to their microstructure. By observation of the microstructure, it should be possible to determine why the differences in elongation values arise.

5.2.4 Martensite Banding

As discussed in Section 2.1.3, the presence of banding in intercritically annealed dual phase steels is a result of the hot band microstructure used in its creation. This banding is due to the segregation of alloying elements during the production of the hot band sheet. It has been established that manganese is the most important element in determining the level of banding in steel, and has been confirmed based on the observations of the current commercial steels. Figure 5.14 plots the level of martensite banding, given by the anisotropy index calculated in Section 4.5, against the manganese content for each steel.

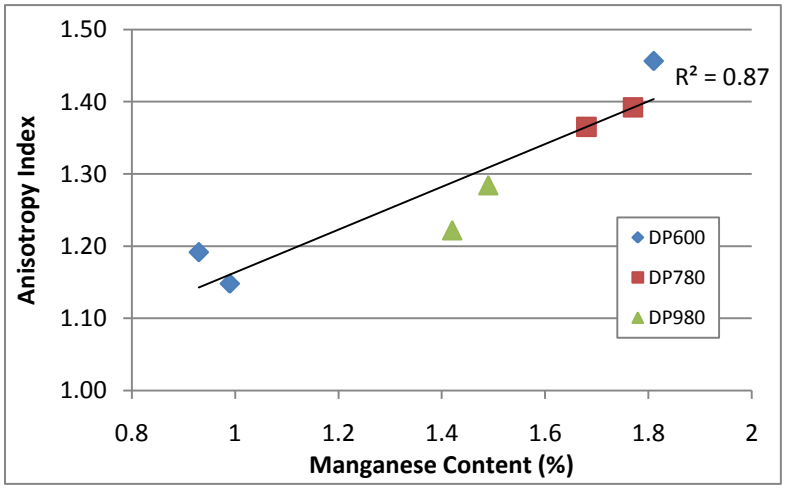

Figure 5.14: Anisotropy index vs. manganese content

The linear correlation confirms that level of banding in dual phase steels is influenced by manganese content. Inspection of the graph also reveals some interesting findings about the

level of banding in each steel grade. The amount of banding in the DP780 steels is actually greater than that observed in the DP980 steels. While the DP980 steels contain greater amounts of martensite, this martensite is less banded and more evenly distributed throughout the microstructure. The reason for this distribution can likely be explained by the amounts of manganese producers must add to assist in the heat treatment of the steels. Because the DP980 steels contain additional carbon compared to the DP780 steels, they do not require as much manganese to sufficiently lower the critical cooling rate of the steel. The DP600 outlier on the chart corresponds to steel 3 which has been discussed in detail in Section 5.2.1. As a consequence of the additional manganese and alloying elements required for heat treatment, the final dual phase steel displays significant banding.

The effect of martensite banding on the deformation and fracture behaviour of dual phase steels has been investigated by several researchers. The presence of martensite banding has been shown to influence the locations at which the nucleation of voids occurs. Melander [77] has shown that the fracture strain of a material is influenced by the randomness of the distribution of voids in ductile fracture. Instead of being random and uniform, Szewczyk et al. [70] demonstrated that voids become concentrated along the martensite bands causing failure to occur sooner than if the martensite particles were more uniformly distributed.

The level of banding in each of the commercial DP600 steels was more closely investigated in order to determine its effect. The fracture surface micrographs obtained from tensile tests can be seen in Figure 5.15. It is evident that both the level and type of martensite banding can be observed at the fracture surface. As expected, steel 3, which has the highest anisotropy index value, clearly shows the most severe impact of banding. The fracture surface contains many parallel striations characteristic of void nucleation. In addition, there are several areas where it appears void coalescence and growth has occurred along a martensite band. As a consequence, steel 3 displayed the worst uniform elongation of the DP600 steels tested. The level of banding in steel 2 does not appear to be adequately described by the anisotropy index. While the quantitative value for banding is low, observation of the actual band morphology, seen in Figure 5.16, illustrates that the banding consists of just one single large martensite band through the

centre of the microstructure. This large band is very apparent on the fracture surface in Figure 5.15. It is likely that the majority of voids nucleated and grew at this location, resulting in the large depression seen on the fracture surface.

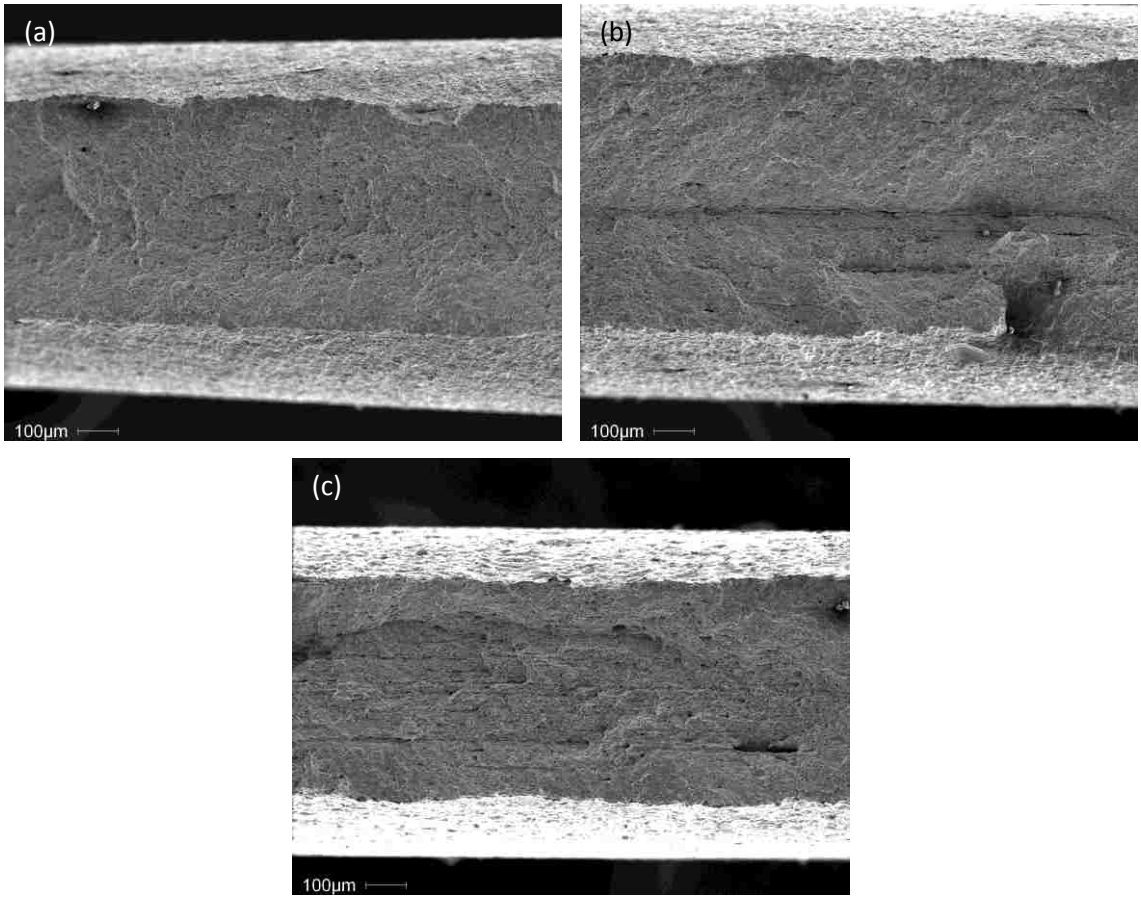

Figure 5.15: Tensile test fracture surfaces of (a) steel 1, (b) steel 2, and (c) steel 3

Figure 5.16: Optical micrograph of transverse plane in steel 2

Figure 5.17 shows a comparison of the cross sections of the tensile fractures for steel 1 and steel 3. It can be seen that the number and distribution of voids is different for each steel. The voids in steel 1, which is a very lightly banded material, are very random in nature. Close to the fracture surface there is no apparent favourable orientation as they are quite uniformly distributed. The void pattern in steel 3 on the other hand is clearly indicative of the effects of martensite banding. The voids in the vicinity of the fracture surface show a distinct linear orientation following the martensite bands along the rolling direction.

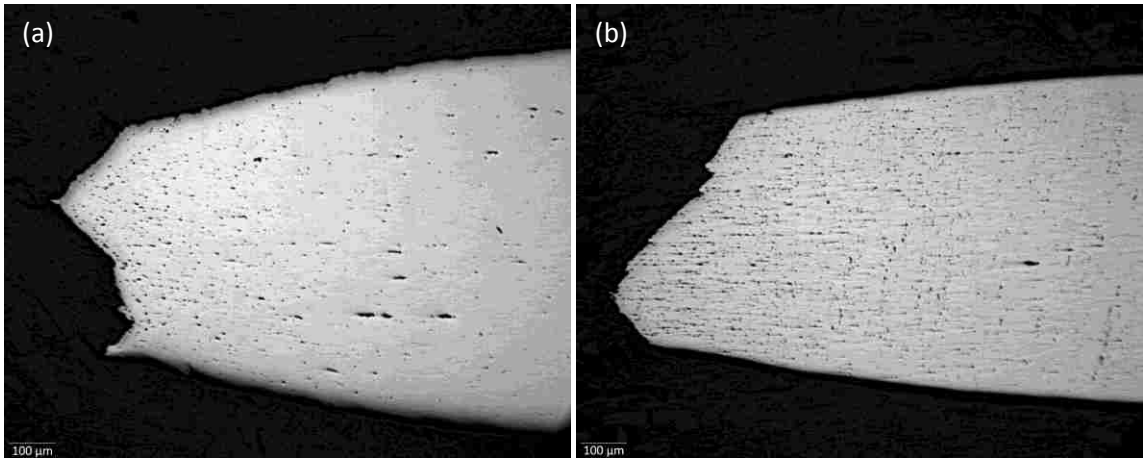

Figure 5.17: Fracture cross sections of (a) steel 1 and (b) steel 3

When the values of uniform elongation for the three DP600 steels are compared, it is apparent that the level of banding in the steel has a definite and sizeable impact on the mechanical

properties. Steel 1, which showed very little sign of martensite banding, had a uniform elongation of 16.2% while the banded steels 2 and 3 had uniform elongations of 13.8% and 13.4%, respectively. It is likely that, if steel 2 and steel 3 were formed into tubes and made to undergo bending, their performance would be worse than the results obtained for the tubes made from steel 1. Martensite banding was observed to influence the formability in tube bending; therefore it is expected that by using more severely banded steel tubes, tube bending performance will be less consistent and reliable.

5.2.5 Martensite Carbon Content

As discussed in Section 2.1.4, the strengths of the individual phases within a dual phase steel directly influence the behaviour of the composite material. In order to evaluate the strength of the martensite phase within dual phase steel, it is important to determine its carbon content. Martensite carbon content can be calculated utilizing the methodology of Speich and Miller [32]. Taking a mass balance for a dual phase steel yields Equation 5.6.

$$|\%C|_a \rho_a = |\%C|_m v_m \rho_m + |\%C|_f (1 - v_m) \rho_f \quad (5.6)$$

By utilizing the assumptions that the density of each phase is the same and that the carbon content in ferrite is negligible, this equation can be reduced to Equation 5.7.

$$|\%C|_m = |\%C|_a / v_m \quad (5.7)$$

where $|\%C|_m$ is the carbon content of the martensite, $|\%C|_a$ is the carbon content of the alloy, and v_m is the martensite volume fraction.

The validity of these assumptions has been tested by El-Sesy et al. [20]. Their results, shown in Figure 5.18, show that carbon content values calculated using Equation 5.7 match closely the actual carbon content measured using electron probe microanalysis.

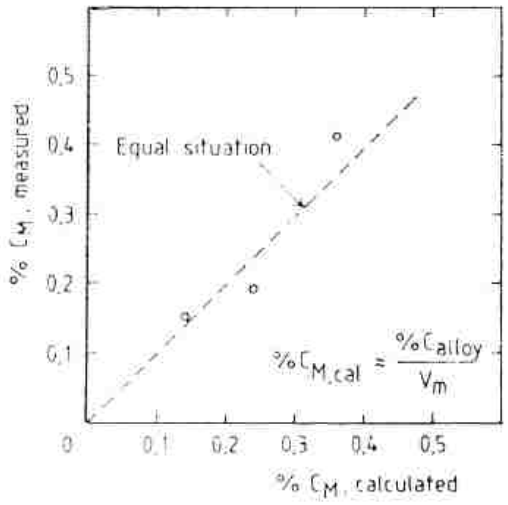

Figure 5.18: Martensite carbon content as measured by El-Sesy et al. [20]

Following this methodology, martensite carbon content values for each commercial steel have been calculated in Table 5.6. Upon inspection, it is observed that, with the exception of steel 3, the carbon content of the martensite decreases as the strength grade increases. This observation implies that although the higher strength grades of dual phase steels have higher overall strengths, the martensite phase in these steels is actually weaker.

	DP600			DP780		DP980	
ID#	1	2	3	4	5	6	7
MVF (%)	14.1	16.2	18.5	21.2	26.2	34.6	38.1
C (%)	0.1	0.12	0.09	0.11	0.15	0.16	0.16
Martensite C (%)	0.71	0.74	0.49	0.52	0.57	0.46	0.42

Table 5.6: Martensite carbon content calculated for each steel

The effects of a lower carbon content martensite have been examined by several researchers. Avramovic-Cingara et al. [44] commented that a lower carbon martensite is likely to deform more compatibly with the ferrite matrix, while a higher carbon martensite can lead to decohesion at the phase interfaces. High carbon martensite, according to Mairea et al. [41], reduces the overall ductility of the steel. Chawla et al. [69] found that a softer martensite phase allows larger post necking strains after uniform elongation. It is a likely explanation for the large

post uniform strains exhibited by steel 3. The substantially lower carbon content of the martensite in this steel increases its capacity to deal with imposed deformation, allowing for less void nucleation and growth by the separation of the ferrite/martensite interfaces.

5.3 Measurement of Individual Phase Hardness

Although researchers have investigated the effects of martensite strength on the deformation behaviour of dual phase steels, their knowledge of the true strength of the martensite phase has been limited. The primary method for determining martensite strength has been through the use of bulk martensitic steel samples which contain the same carbon content as that calculated for the martensite phase within the dual phase steel. While this may provide an acceptable approximation, a more desirable method would be to directly measure the strength of the individual phases within dual phase steel, foregoing the use of analogue samples.

5.3.1 Micro Indentation

In an initial attempt to measure the hardness of both the ferrite and martensite phases within dual phase steel, micro hardness testing was performed. Using both Vickers and Knoop indenters with loads of 10 grams, indentations were made on several of the commercial dual phase steels. A micrograph illustrating a series of Vickers indentations performed on steel 1 can be seen in Figure 5.19. It is apparent based on this micrograph that the indentations are too large to adequately describe the hardness of the ferrite and martensite separately. The indentations shown in Figure 5.19 are over 10 μm in size; they are larger than the mean ferrite grain size and consequently also much larger than the martensite particles. They are also not well defined, making the calculation of meaningful hardness values impossible. Similar results were also obtained for the Knoop indentations. The narrow indentations did not provide sufficient detail at low loads to obtain valid hardness results.

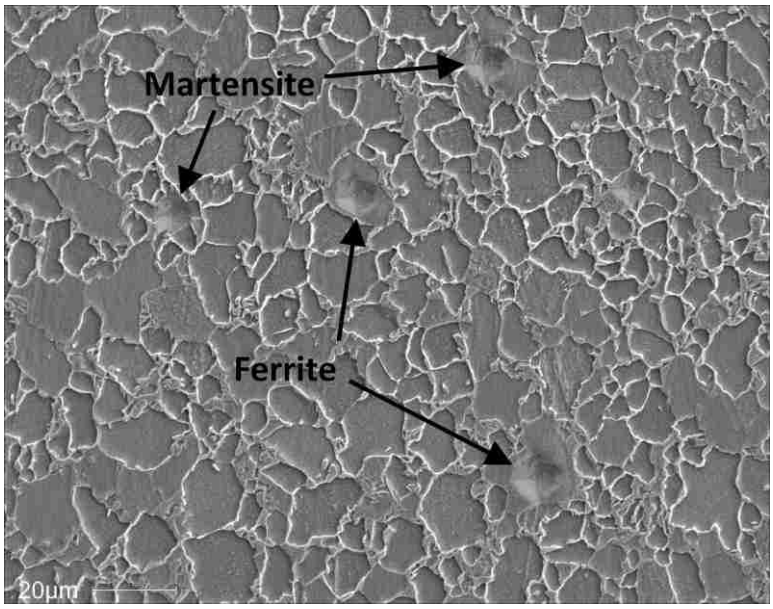

Figure 5.19: Vickers micro indentations attempted on individual phases

It has been claimed by El-Sesy et al. [20] that they were able to obtain individual phase hardness measurements using micro indentation equipment. Based on the present work on commercial steels, this claim seems doubtful. Although they did not present micrographs of their steels, it is unlikely that the size of their martensite particles was large enough to be adequately described by the Vickers micro indenter. The experience in the present work matches much more closely the work of Szewczyk et al. [70], who found that micro indentations were too large to characterize martensite particles, and that the hardness values obtained for ferrite grains reflected their constrained hardness with influences from the grain boundaries. The current work supports the conclusion that micro hardness techniques are not on a scale small enough to adequately characterize individual phases, and therefore smaller scale techniques such as nano indentation are required.

5.3.2 Nano Indentation

Traditionally, the use of nano indentation has been primarily focussed on thin films and hard surface coatings. Nano indentation on multiphase steels has not been widespread, and therefore the techniques by which to carry it out have not been well described in literature. As

such, procedures both to prepare the samples, as well as operate the nano indentation equipment had to be developed for the current work using a trial and error process.

In order to identify the specific phases in which each indentation was being placed, initial samples were etched with 2% Nital to reveal their microstructure. The intent was to indent the etched sample in several locations, and then observe those indentations using a scanning electron microscope. This technique was attempted on one sample from each strength grade, and in all cases turned out to yield very poor results. Hardness values obtained from the indentations showed very little distinction between the ferrite and martensite phases. Additionally, the reduced modulus values were found to range from 50 GPa to over 400 GPa, indicating that the results were clearly flawed. Problems also arose with indentations being absent from locations in which they were thought to be indented. Figure 5.20 shows a micrograph of a six by six grid of nano indentations placed on the etched surface of the DP980. While several indentations are clearly visible, many more are absent. Although data was obtained for the loading and unloading of the indenter, the lack of visible indentations on the surface of the material further confirms the invalidity of this technique.

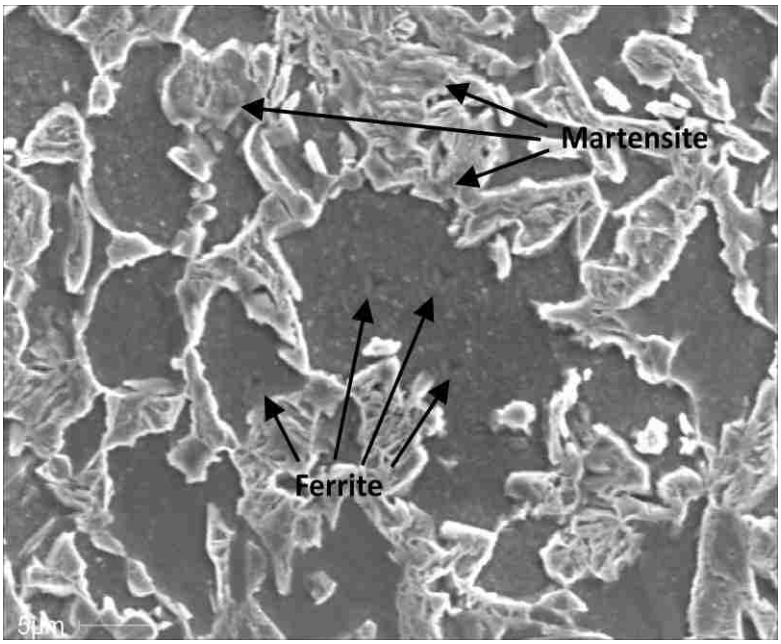

Figure 5.20: Nano indentations on DP980

As mentioned in Section 2.3.1, the small size of the nano indenter tip makes it very sensitive to the surface roughness of the sample being indented. As the indenter is lowered towards the sample surface, any contact with a raised peak can generate invalid results. This may explain why the results on the etched samples were poor. The etching process preferentially removes material from the sample surface in order to differentiate the phases. It is possible that the effects of the etching produced a surface that was incompatible with the nano indenter and thus generated bad results. Given that data was collected for the missing indentations in Figure 5.20, it is likely that the indenter made contact with the material surface; however, this contact was not sufficient to generate a good indentation.

In order to test this hypothesis, samples from each steel grade were treated by polishing only, with no subsequent etching. These unetched samples were then indented with the same series of indentations that had been placed on the etched samples. The results obtained from the unetched samples were considerably different than those on the etched samples, and pointed to the possibility of identifying the phase in which the indentation was placed strictly by interpreting the hardness value. An example of two load-displacement curves for indentations obtained from the unetched DP600 can be seen in Figure 5.21. The values calculated for both the hardness and reduced modulus can be found in this figure. While the elastic modulus values are nearly equal, the hardness values are distinctly different. Elastic modulus is a function of the atomic bonds within a material, and therefore fairly independent of crystallography. Although considerably harder, martensite has the same elastic modulus as ferrite [10]. It therefore stands to reason that the indentations made in Figure 5.21 are in fact good indentations which have managed to make contact with separate phases within the dual phase microstructure. By strictly observing the hardness values, while making sure that the elastic modulus values are consistent, it appears to be possible to characterize the individual phases within a dual phase steel without requiring microscopic observation of the indentations.

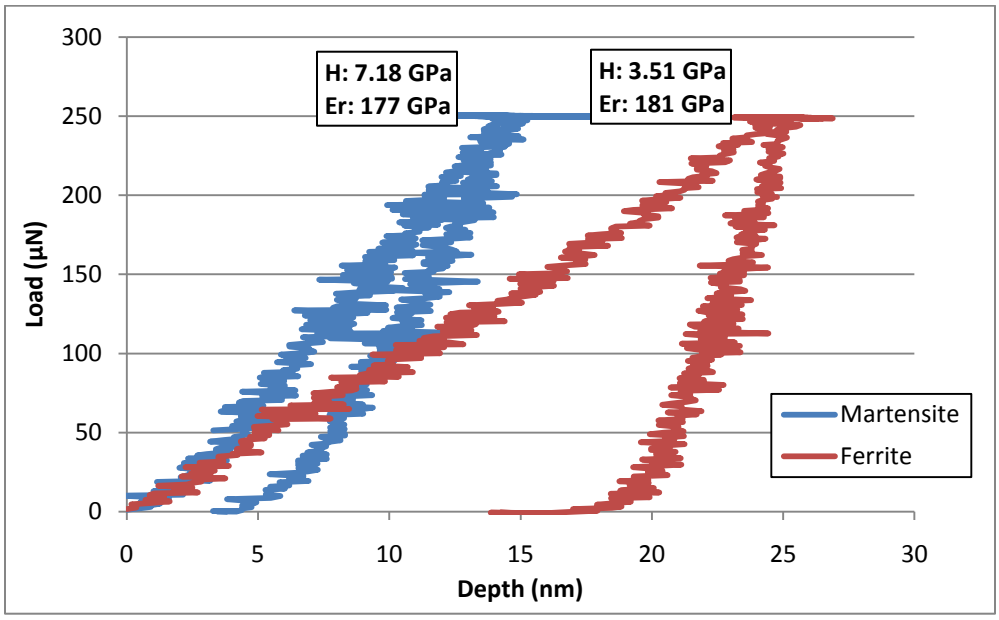

Figure 5.21: Load vs. depth curves for DP600

5.3.3 Comparison of Hardness Values

Given the data presented for martensite carbon content in Table 5.6 in Section 5.2.5, it was implied that for the commercial dual phase steels tested that the strength of the martensite phase decreased as the strength grade of the steel increased. In order to experimentally confirm this, and to further enhance the understanding of the nano indentation technique on dual phase steels, indentations were performed on each steel grade offered by supplier A. These indentations were placed in eight by eight grid patterns located within 30 µm by 30 µm squares. Results from these indentations can be found in Figure 4.16, Figure 4.18, and Figure 4.20. Observation of the histograms displaying the measured reduced modulus values illustrate that for all three steels, the modulus values were normally distributed around a peak of 180 GPa. Using the relationship shown in Equation 2.8, it can be shown to correspond quite closely with the accepted elastic modulus value for steel of 200 GPa. Observation of the histograms displaying the measured hardness values reveals several unique features. For the sake of clarity, these histograms have been formatted and combined in Figure 5.22.

Inspection of Figure 5.22 reveals several interesting and important features. First, each curve possesses one major peak located at 3.5 GPa followed by one or more peaks at higher hardness values. The major peak represents indentations within the ferrite phase of the steel, while the subsequent peaks represent indentations within the martensite phase. Given that all three steels are produced by the same supplier, and are from the same carbon-manganese family, it is not surprising that the ferrite phase in each steel possesses the same hardness. It is expected that the dislocation densities within the ferrite phase of each steel are similar. Additionally, none of the three steels contain precipitate forming elements which would presumably cause the ferrite peak to shift to higher hardness values.

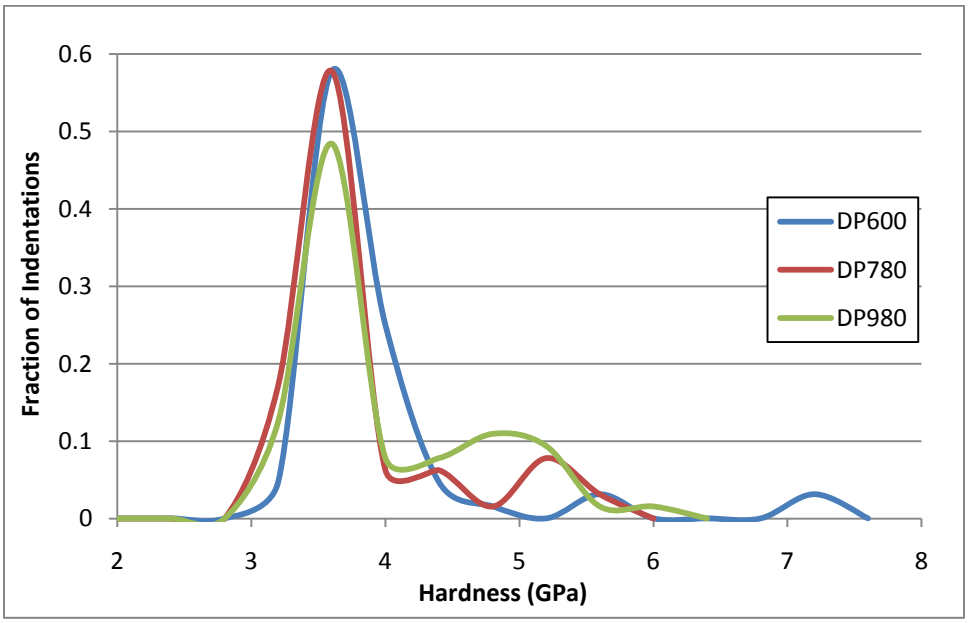

Figure 5.22: Comparison of nano hardness distributions for different steel grades

The relative heights of the ferrite and martensite peaks are indicative of the volume fractions of the two phases within the microstructure. As the strength grade of the steel is increased, martensite volume fraction is increased. As a result, the height of the martensite peak increases, indicating more indentations are landing in the martensite phase, while the height of the ferrite peak decreases by a corresponding amount.

The prediction regarding the strength of the martensite phase in each steel grade can be confirmed from the curves in Figure 5.22. It was shown that for the steels from producer A, the carbon content of the martensite for the DP600, DP780, and DP980 was 0.71%, 0.52%, and 0.46%, respectively. When looking at the location of the martensite peaks in Figure 5.22, it can be seen that as the strength grade of the steel is increased, the martensite peak is shifted towards lower hardness values. This observation confirms the predicted trend towards softer martensite as the strength grade of the steel is increased. Taking an average of the hardness values over the range of martensite indentations yields average martensite hardness values of 6.2 GPa for DP600, 5.0 GPa for DP780 and 4.7 GPa for DP980.

As previously mentioned, there is a paucity of research presently available describing the nano indentation process on dual phase steels. As such, there is little data for comparison with the present values for ferrite and martensite hardness. Hernandez et al. [78] used nano indentation to measure the hardness of spot welded DP980 steel. They found ferrite hardness to be in the 3 GPa range, while their martensite ranged from 6 to 8 GPa. Chen et al. [79] indented 780 MPa TRIP steel and found ferrite hardness ranging from 2.6 to 3.1 GPa while martensite hardness was 5.5 GPa. Fernemont et al. [80] indented TRIP steels with varying silicon contents and found ferrite hardness to be 4.8 GPa while their martensite hardness was extremely high at 16.7 GPa.

A direct comparison of nano hardness values for each phase between the different groups of researchers is not particularly useful. The first problem arises from the fact that the indenter loadings used by each researcher are not constant. As described in Section 2.3.1, the indentation size effect can come into play at small loads; it is therefore only truly valid to directly compare testing done with the same loads. Additional problems also arise due to the unique chemistries and thermal histories of each material, both of which can directly impact the hardness of each phase. The comparison of hardness values between different types of multiphase steels means that variations in these parameters will likely be large.

From the values presented above, it is interesting to note that the ferrite hardness values are much more similar between the steels presented from literature and those tested in the present

work. Ferrite is less sensitive to changes in alloy carbon content and thermal treatment; therefore it is no surprise that the values across all of the different works are similar. The hardness of martensite on the other hand is quite sensitive to both alloy chemistry and thermal treatments. For example, it is known that during even short tempering treatments, carbon within the martensite is able to segregate to dislocations or twin boundaries, lowering its hardness [23]. As described in Section 5.2.2, indications of tempering were observed in both DP600 and DP780 from producer A. It is unknown to what degree the hardness of the martensite within these steels was affected; however, it is a clear illustration of the challenges associated with comparing hardness values across different steels.

Chapter 6:

Conclusions, Recommendations, and Contributions to the Field

The following chapter summarizes the conclusions made from the current work, and proposes several ideas for future research directions. Finally, a brief synopsis is given describing the unique contributions this research has provided to the overall body of knowledge on dual phase steels.

6.1 Conclusions

Based on the experiments performed and the observations carried out during this work, the following conclusions can be made:

1. The rotary draw mandrel bending results for dual phase steel tubes show that bending success is stochastic in nature. For a given steel strength grade and bend ratio, the tube may be successfully bent some of the time, and fail others. There appears to be a minimum bend ratio to which each steel grade can reliably be bent. These were found to be 2.0 for DP600 and 3.1 for DP780 and DP980. As the bend ratio was decreased, the reliability of the bending process also decreased.

2. Bending success appears to be affected by the same microstructural factors that affect samples in uniaxial tension: primarily inclusions and martensite banding in the extrados of the bent tube. Large numbers of inclusions and the presence of martensite banding are detrimental to tube bending performance.

3. Differences exist in both the mechanical properties and the microstructures of dual phase steels from different suppliers falling under the same strength grade. The microstructural differences appear to affect elongation more than strength. Strength is primarily dictated by martensite volume fraction, while elongation is reduced given the presence of martensite

banding. Suggestions regarding steels from specific steel producers have been provided to Vari-Form.

4. It is possible to investigate and characterize the individual phases within commercial dual phase steels using nano indentation. Elastic modulus measured via nano indentation is similar across both ferrite and martensite phases, while hardness is distinctly different.

5. For all three steel strength grades, average ferrite hardness was found to be 3.5 GPa. Average martensite hardness was found to be 6.2 GPa for DP600, 5.0 GPa for DP780 and 4.7 GPa for DP980. These values confirmed the trend predicted based on the values calculated for martensite carbon content.

6.2 Recommendations for Future Work

The following recommendations are made for future work which can build on and enhance the work performed in this study:

1. Use measured tube bending strains to validate FEA model of dual phase steels undergoing rotary draw mandrel bending.

2. Extend comparison of commercial materials to include additional testing methods such as hole expansion, dome stretching and stretch bending. These methods will provide a more complete picture of the ability of each steel to undergo commonly encountered industrial forming processes.

3. Acquire dual phase steels of each strength grade from additional producers. It will allow further development of a comparative database of commercial steels.

3. Perform nano indentation testing on more dual phase steels and compare the hardness values of ferrite and martensite for each of them.

4. Attempt to utilize multiple nano indentations within single ferrite grains and martensite particles to develop an understanding of their localized heterogeneities.

6.3 Unique Contributions to the Field

Although dual phase steels have been well researched over the past five decades, the current work contributes to advances in understanding of these steels in two fashions. First, knowledge of microstructural behaviour of dual phase steels undergoing tube bending and hydroforming has been obtained. Many of the same factors that affect material performance in uniaxial tension were found to affect performance in tube bending. As such, past and future research of dual phase steels utilizing tensile testing can be applied to provide enhancements to tube bending and hydroforming performance. Secondly, with the use of commercially available nano indentation equipment, it was shown that the ferrite and martensite phases in dual phase steels of different strength grades were not identical. The hardness of the martensite phase widely varied based on the carbon content and martensite volume fraction of the steel. The development of techniques to characterize dual phase steels on a sub-micron scale allows for further advances in the understanding of their micromechanical behaviour in the future.

Bibliography

[1] Williams, E. W., and L. K. Davies, "Recent Developments in Annealing", ISI Special Report 79, 1963

[2] Lutsey, N.,"Review of Technical Literature and Trends Related to Automobile Mass-Reduction Technology", Institute of Transportation Studies, University of California-Davis, 2010

[3] World Auto Steel, “Advanced High Strength Steel (AHSS) Applications Guidelines”, 2009

[4] Davies, R. G., and C. L. Magee, "Physical Metallurgy of Automotive High Strength Steels", In Structure and Properties of Dual-Phase Steels, by R.A. Kot and J.W. Morris, pp. 1-19, TMS-AIME, 1979

[5] Rigsbee, J. M., J. K. Abraham, A. T. Davenport, J. E. Franklin, and J. W. Pickens, "Structure-Processing and Structure-Property Relationships in Commercially Produced Dual-Phase Steels", In Structure and Properties of Dual-Phase Steels, by R. A. Kot and J. W. Morris, pp. 304-329, 1979

[6] Hansen, S. S., and R. R. Pradhan, "Structure/Property Relationships and Continuous Yielding Behaviour in Dual-Phase Steels", In Fundamentals of Dual-Phase Steels, by R. A. Kot and B. L. Bramfitt, pp. 113-143, TMS-AIME, 1981

[7] Hovath, C. D., and J. R. Fekete, "International Opportunities and Challenges for Increased Usage of Advanced High Strength Steels in Automotive Applications", International Conference on Advanced High Strength Sheet Steels for Automotive Applications Proceedings, Association for Iron & Steel Technology, pp. 3-10, 2004

[8] SSAB Swedish Steel, "Docol DP/DL Cold Reduced Dual Phase Steels", Material Specification Data, 2010

[9] Smallman, R. E., and R. J. Bishop, Modern Physical Metallurgy and Materials Engineering, 6th Edition, Butterworth Heinemann, 1999

[10] Llewellyn, D. T., and R. C. Hudd, Steels: Metallurgy and Applications, 3rd Edition, Butterworth Heinemann, 1998

[11] Park, K. S., K. T. Park, D. L. Lee, and C. S. Lee, "Effect of Heat Treatment Path on the Cold Formability of Drawn Dual-Phase Steels", Materials Science and Engineering A 449-451, pp. 1135-1138, 2007

[12] Lis, J., A. K. Lis, and C. Kolan, "Processing and Properties of C–Mn Steel with Dual-Phase Microstructure", Journal of Materials Processing Technology 162-163, pp. 350-354, 2005

[13] Krauss, G., and A. R. Marder, "The Morphology of Martensite in Iron Alloys", Metallurgical and Materials Transactions, pp. 2343-2349, 1971

[14] Shirasawa, H., and J. G. Thomson, "Effect of Hot Band Microstructure on Strength and Ductility of Cold Rolled Dual Phase Steel", Transactions of the Iron and Steel Institute of Japan 27, no. 5, pp. 360-365, 1987

[15] Kuang, S., Y. L. Kang, H. Yu, and R. D. Liu, "Simulation of Intercritical Austenization of a C-Mn Cold Rolled Dual Phase Steel", Materials Science Forum 575-578, pp. 1062-1069, 2008

[16] Sun, S., and M. Pugh, "Manganese Partitioning in Dual-Phase Steel During Annealing", Materials Science and Engineering A 276, no. 1-2, pp. 167-174, 2000

[17] Erdogan, M., "Effect of Austenite Dispersion on Phase Transformation in Dual Phase Steel", Scripta Materialia 48, no. 5, pp. 501-506, 2003

[18] Zeytin, H. K., C. Kubilay, and H. Aydin, "Investigation of Dual Phase Transformation of Commercial Low Alloy Steels", Materials Letters 62, no. 17-18, pp. 2651-2653, 2008

[19] Ajmal, M., M. A. Tindyala, and R. Priestner, "Effect of Controlled Rolling on the Martensitic Hardenability of Dual Phase Steel", International Journal of Minerals, Metallurgy, and Materials 16, no. 2, pp. 165-169, 2009

[20] El-Sesy, I. A., and Z. M. El-Baradie, "Influence of Carbon on the Structure and Properties of Dual-Phase Steels", Materials Letters 57, pp. 580-585, 2002

[21] Li, L., H. Ding, L. Du, J. Wen, H. Song, and P. Zhang, "Influence of Mn Content and Hot Deformation on Transformation Behavior of C-Mn Steels", Journal of Iron and Steel Research 15, no. 2, pp. 51-55, 2008

[22] Rashid, M. S., "Dual Phase Steels", Annual Review of Materials Science 11, pp. 245-266, 1981

[23] Smith, W. F., Structure and Properties of Engineering Alloys, 2nd Edition, McGraw-Hill, 1993

[24] Doherty, R. D., and D. A. Melford, Journal of the Iron and Steel Institute 204, pp. 1131-1143, 1966

[25] Leslie, W. C., The Physical Metallurgy of Steels, McGraw-Hill, 1981

[26] Majka, T. F., D. K. Matlock, and G. Krauss, "Development of Microstructural Banding in Low-Alloy Steel with Simulated Mn Segregation", Metallurgical and Materials Transactions A 33, no. 6, pp. 1627-1637, 2002

[27] Park, Y. J., A. P. Coldren, and J. W. Morrow, "Effect of Martensite Bands and Elongated Manganese Sulfide Inclusions on the Formability of Dual-Phase Steels", In Fundamentals of Dual-Phase Steels, by R. A. Kot and B. L. Bramfitt, pp. 485-497, TMS-AIME, 1981

[28] Lawson, P. D., D. K. Matlock, and G. Krauss, "The Effect of Microstructure on the Deformation and Mechanical Behaviour of a Dual-Phase Steel", In Fundamentals of Dual-Phase Steels, by R. A. Kot and B. L. Bramfitt, pp. 347-381, TMS-AIME, 1981

[29] Gladman, T., In Advances in the Physical Metallurgy and Applications of Steel, by B.L. Eyre, p. 55, The Metals Society, 1981

[30] Jiang, Z., Z. Guan, and J. Lian, "Effects of Microstructural Variables on the Deformation Behaviour of Dual-Phase Steel", Materials Science and Engineering A 190, no. 1-2, pp. 55-64, 1995

[31] Mazinani, M., and W. J. Poole, "Effect of Martensite Plasticity on the Deformation Behavior of a Low-Carbon Dual-Phase Steel", Metallurgical and Materials Transactions A 38, no. 2, pp. 328-339, 2007

[32] Speich, G. R., and R. L. Miller, "Mechanical Properties of Ferrite-Martensite Steels", In Structure and Properties of Dual-Phase Steels, by R. A. Kot and J. W. Morris, pp. 145-182, TMS-AIME, 1979

[33] Chen, H. C., and G. H. Cheng, "Effect of Martensite Strength on the Tensile Strength of Dual Phase Steels", Journal of Materials Science 24, pp. 1991-1994, 1989

[34] Ramos, L. F., D. K. Matlock, and G. Krauss, Metallurgical and Materials Transactions A 10, pp. 259-261, 1979

[35] Korzekwa, D. A., D. K. Matlock, and G. Krauss, "Dislocation Substructure as a Function of Strain in a Dual-Phase Steel", Metallurgical and Materials Transactions A 15, no. 6, pp. 1221-1228, 1984

[36] Jaoul, B., “Etude de la Forme des Courbes de la Deformation Plastique”, Journal of the Mechanics and Physics of Solids 5, pp. 95-114, 1957

[37] Matlock, D. K., G. Krauss, L. F. Famos, and G. S. Huppi, "A Correlation of Processing Variables with Deformation Behavior of Dual-Phase Steels", In Structure and Properties of Dual-Phase Steels, by R. A. Kot and J. W. Morris, pp. 62-90, TMS-AIME, 1979

[38] Cribb, W. R., and J. M. Rigsbee, "Work Hardening Behaviour and its Relationship to the Microstructure and Mechanical Properties of Dual-Phase Steels", In Structure and Properties of Dual-Phase Steels, by R. A. Kot and J. W. Morris, pp. 91-117, TMS-AIME, 1979

[39] Sun, X., K. S. Choi, A. Soulami, W. N. Liu, and M. A. Khaleel, "On Key Factors Influencing Ductile Fractures of Dual Phase Steels", Materials Science and Engineering A 526, no. 1-2, pp. 140-149, 2009

[40] Steinbrunner, D. L., D. K. Matlock, and G. Krauss, "Void Formation During Tensile Testing of Dual Phase Steels", Metallurgical and Materials Transactions A 19, no. 3, pp. 579-589, 1988

[41] Mairea, E., O. Bouazizb, M. Di Michielc, and C. Verdua, "Initiation and Growth of Damage in a Dual-Phase Steel Observed by X-ray Microtomography", Acta Materialia 56, no. 18, pp. 4954-4964, 2008

[42] Avramovic-Cingara, G., A. R. Saleh, M. K. Jain, and D. S. Wilkinson, "Void Nucleation and Growth in Dual-Phase Steel 600 during Uniaxial Tensile Testing", Metallurgical and Materials Transactions A 40, no. 13, pp. 3117-3127, 2009

[43] He, X. J., N. Terao, and A. Berghezan, "Influence of Martensite Morphology and its Dispersion on Mechanical Properties and Fracture Mechanisms of Fe-Mn-C Dual Phase Steels", Metal Science 18, no. 7, pp. 367-373, 1984

[44] Avramovic-Cingara, G., Y. Ososkov, M. K. Jain, and D. S. Wilkinson, "Effect of Martensite Distribution on Damage Behaviour in DP600 Dual Phase Steels", Materials Science and Engineering A 516, no. 1-2, pp. 7-16, 2009

[45] Ahmad, E., T. Manzoor, K. L. Ali, and J. I. Akhter, "Effect of Microvoid Formation on the Tensile Properties of Dual-Phase Steel", Journal of Materials Engineering and Performance 9, no. 3, pp. 306-310, 2009

[46] Toyoda, S., K. Suzuki, and A. Sato, “High Strength Steel Tubes for Automotive Suspension Parts”, JFE Steel, 2004

[47] Carleer, B. D., "FE Process Simulation for Tube Hydroforming Starting With the Tube Forming Process", International Conference on Hydroforming, Stuttgart, Germany, 2001

[48] Pavlina, E. J., C. J. Van Tyne, and K. Hertel, "Hydraulic Bulge Testing of Dual Phase Steel Tubes Produced Using a Novel Processing Route", Journal of Materials Processing Technology 201, no. 1-3, pp. 242-246, 2008

[49] Shah, K., Y. Aue-u-lan, and T. Altan, "Getting it Right - Using Finite Element Analysis to Roll Form Tubes", The Tube & Pipe Journal, September, 2003

[50] Khodayari, G.,"Hydroforming of Pre-Bent Aluminum Tubes", International Conference on Accuracy in Forming Technology, Chemnitz, Germany, 2003

[51] Gholipour, J., M. J. Worswick, D. A. Oliveira, and G. Khodayari, "Severity of the Bend and Its Effects on the Subsequent Hydroforming Process for Aluminum Tube", Materials Processing and Design: Modeling, Simulation and Applications - NUMIFORM 2004, pp. 1089-1094, 2004

[52] Strano, M., "Automatic Tooling Design for Rotary Draw Bending of Tubes", International Journal of Advanced Manufacturing Technology 26, pp. 733-740, 2005

[53] Li, H., H. Yang, and M. Zhan, "A Study on Plastic Wrinkling in Thin-Walled Tube Bending via an Energy-Based Wrinkling Prediction Model", Modelling and Simulation in Materials Science and Engineering 17, pp. 1-33, 2009

[54] Oliveira, D. A., M. J. Worswick, and R. Grantab, "Effect of Lubricant in Mandrel-Rotary Draw Tube Bending of Steel and Aluminum", Canadian Metallurgical Quarterly 44, no. 1, pp. 71-78, 2005

[55] Khodayari, G., "Bending Limit Curve for Rotary Draw Bending of Tubular Components in Automotive Hydroforming Applications", SAE International Journal of Materials and Manufacturing 1, no. 1, pp. 841-848, 2009

[56] Inoue, K., and P. B. Mellor, "Radial-Draw Bending of Stainless Steel Tube", Journal of Metal Working Technology 3, no. 2, pp. 151-166, 1979

[57] Khodayari, G., and M. Worswick, "Examining the Effects of Push Assist on the Formability of Aluminum Tubes", The Tube & Pipe Journal, July, 2003

[58] Lang, L. H., et al., "Hydroforming Highlights: Sheet Hydroforming and Tube Hydroforming", Journal of Materials Processing Technology 151, no. 1-3, pp. 165-177, 2004

[59] Ahmetoglu, M., and T. Altan, "Tube Hydroforming: State-of-the-Art and Future Trends", Journal of Materials Processing Technology 98, no. 1, p. 15, 2000

[60] Vari-Form, "The Hydroform Advantage", Strathroy, Ontario, 2004

[61] Morphy, G., “Hydroforming High Strength Steel Tube for Automotive Structural Applications Using Expansion”, SAE Technical Paper Series, 970373, pp. 107-114, 1997

[62] Cudini, Ivano G., Method of Forming Box-like Frame Members, United States of America Patent 4,744,237, 1988

[63] Morphy, G., "Tube Hydroforming: Efficiency and Effectiveness of Pressure Sequence Hydroforming", International Body Engineering Conference, Detroit, Michigan, 1998

[64] Oliver, W. C., and G. M. Pharr, "An Improved Technique for Determining Hardness and Elastic Modulus Using Load and Displacement Sensing Indentation Experiments", Journal of Materials Research 7, no. 6, pp. 1564-1583, 1992

[65] Oliver, W. C., and G. M. Pharr, "Measurement of Hardness and Elastic Modulus by Instrumented Indentation: Advances in Understanding and Refinements to Methodology", Journal of Materials Research 19, no. 3, pp. 3-20, 2004

[66] Viella, J. R., Metallographic Technique for Steels, American Society for Metals, 1938

[67] Dowling, N. E., Mechanical Behavior of Materials: Engineering Methods for Deformation, Fracture and Fatigue, 3rd Edition, Pearson Prentice Hall, 2007

[68] Broek, D., "Some Contributions of Electron Fractography to the Theory of Fracture", International Metals Reviews 9, pp. 135-181, 1974

[69] Chawla, K. K., P. R. Rios, and J. R.C. Guimaraes, "Fractography of a Dual Phase Steel", Journal of Materials Science Letters 2, no. 3, pp. 94-98, 1983

[70] Szewczyk, A. F., and J. Gurland, "A Study of the Deformation and Fracture of a Dual-Phase Steel", Metallurgical and Materials Transactions A 13, no. 10, pp. 1821-1826, 1982

[71] Meng, Q., J. Li, J. Wang, Z. Zhang, and L. Zhang, "Effect of Water Quenching Process on Microstructure and Tensile Properties of Low Alloy Cold Rolled Dual-Phase Steel", Materials and Design 30, no. 7, pp. 2379-2385, 2009

[72] Tobiyama, Y., K. Osawa, and M. Hirata, "Development of 590MPa Grade Galvannealed Sheet Steels with Dual Phase Structure", Kawasaki Steel Giho 31, no. 3, pp. 181-184, 1999

[73] Andrews, K.W., "Empirical Formulas for the Calculation of Some Transformation Temperatures", Journal of the Iron and Steel Institute 203, pp. 721-727, 1965

[74] Irie, T., S. Satoh, K. Hashiguchi, I. Takahashi, and O. Hashimoto, "Metallurgical Factors Affecting the Formability of Cold-rolled High Strength Steel Sheets", Transactions of the Iron and Steel Institute of Japan 21, p. 793, 1981

[75] Gunduz, S., "Effect of Chemical Composition, Martensite Volume Fraction and Tempering on Tensile Behavior of Dual Phase Steels", Materials Letters 63, no. 27, pp. 2381-2383, 2009

[76] Fang, X., Z. Fan, B. Ralph, P. Evans, and R. Underhill, "Effects of Tempering Temperature on Tensile and Hole Expansion Properties of a C-Mn Steel", Journal of Materials Processing Technology 132, no. 1-3, pp. 215-218, 2003

[77] Melander, A., "Computer Simulation of Ductile Fracture in a Random Distribution of Voids", Materials Science and Engineering 39, no. 1, pp. 57-63, 1979

[78] Baltazar Hernandez, V. H., S. K. Panda, M. L. Kuntz, and Y. Zhou, "Nanoindentation and Microstructure Analysis of Resistance Spot Welded Dual Phase Steel", Materials Letters 64, no. 2, pp. 207-210, 2010

[79] Chen, J., et al., "Transmission Electron Microscopy and Nanoindentation Study of the Weld Zone Microstructure of Diode-Laser-Joined Automotive Transformation Induced Plasticity Steel", Metallurgical and Materials Transactions A 39, pp. 593-603, 2008

[80] Furnemont, Q., M. Kempf, P. J. Jacques, M. Goken, and F. Delannay, "One the Measurement of the Nanohardness of the Constitutive Phases of TRIP-assisted Multiphase Steels", Materials Science and Engineering A 328, no. 1-2, pp. 26-32, 2002

Vita Auctoris

NAME: Chad Oliver

PLACE OF BIRTH: Windsor, Ontario

YEAR OF BIRTH: 1985

EDUCATION: Bachelor of Applied Science
Mechanical Engineering – Materials Option – Co-operative Education
University of Windsor
Windsor, Ontario
2008

Master of Applied Science
Engineering Materials
University of Windsor
Windsor, Ontario
2010